School of Physics and Astronomy
Condensed Matter Department
Femto-Nano Group

Dissertation submitted to the Tel-Aviv University Senate for the degree Doctor of Philosophy

Multifrequency Near Field Optics and Composite Pulses for Quantum Coherent Control

by Hadar Greener

This work has been carried out under the supervision of

Prof. Haim Suchowski

March 2021

by Hadar Greener

Multifrequency Near Field Optics and Composite Pulses for Quantum Coherent Control

Dissertation submitted to the Tel-Aviv University Senate for the degree Doctor of Philosophy,
March 2021

Supervisor: Prof. Haim Suchowski

Tel Aviv University

Femto-Nano Group

Condensed Matter Department

School of Physics and Astronomy

Abstract

With the advent of novel techniques, which push the limits of nano-scaled fabrication of materials, the characterization and understanding of their fundamental physical properties is of paramount importance. Specifically, the ability to control how these materials are manipulated and interact with light is key, as they may be the next generation detectors and modulators for electronic and optical information. In this research, I explored light-matter interactions on two fronts, the first being through near-field scanning optical microscopy and the second through developing a new scheme of composite pulses for quantum coherent control.

Scanning near-field optical microscopy (SNOM) has revolutionized the study of fundamental physics, as it is one of the very few optical non-invasive imaging techniques with subwavelength resolution. This has been particularly valuable to gain an intimate understanding of the processes in platforms, such as 2D materials, plasmonics and waveguide systems, that allow to tailor light-matter interactions at the nanoscale. The spatial resolution of SNOM, based on the atomic force microscope (AFM), is limited mainly by the apex of the probing tip (˜15nm), and by the poor discrimination of near-field optical signals from a much stronger far-field background. Thus, the achievement of high sensitivity in such measurements remains a daunting task. In this work, I theoretically derived and experimentally applied a feasible multifrequency SNOM method that results in enhanced sensitivity for the detection of weak near-field signals of dielectric contrast. I achieved two-fold enhanced sensitivity in the measurement of near field signals as a function of tip-sample distance, gaining higher sensitivity to such optical measurements.

The second front of my research focused on advancing methods of quantum coherent control schemes for quantum information processing (QIP). In particular, my aim was to design high-fidelity and robust control protocols for quantum integrated photonics platforms. I studied the dynamics of quantum systems interacting with an external electric field and derived techniques for accurate state transfer within the threshold for QIP. I generalized popular composite pulses schemes (CPs) to N-level systems with SU(2) symmetry, and developed a novel family of CPs, harnessing for the first time the detuning as a control parameter. Detuning-modulated CPs (DMCPs) allow for remarkable tolerance against pulse area errors, reaching high fidelities of under 10^{-4}, within the lifetime of the system. They are perfectly suited for implementation in integrated photonic circuits to overcome inaccuracies in fabrication and provide a path for true high-fidelity QIP schemes. Moreover, DMCPs provide a foundation for short error-correction techniques suitable to control other qubit architectures.

Acknowledgements

> *Science is a collaborative effort. The combined results of several people working together is often much more effective than could be that of an individual scientist working alone.*
>
> **— John Bardeen**
> (Nobel Prize Physicist)

I would like to take the opportunity to thank the dear people without whom I would never have graduated. First, to Prof. Haim Suchowski for taking me in as a hardcore condensed matter MSc and guiding my way into optics and quantum coherent control. Thank you for teaching me important lessons, from innovative thinking and formulation of research questions through showstopping presentation of results. Your time has been a great gift to me and the team you built of excellent scientists in the Femto-Nano group, for whom I am also thankful.

I am grateful for the opportunities I had to learn from fruitful collaborations with Dr. Elica Kyoseva, Dr. Michael Mrejen, Dr. Lena Yadgarov, Tom Coen and Dr. Asaf Levanon. Thanks to the members of the third floor of Shenkar and the Kaplun basement for your friendship and coffee breaks, from which many ideas emerged. Specifically, I would like to thank Erga Lifshitz and Gal Tuvia for their immediate onboarding and experimental expertise for my scientific endeavours, which originated from one such conversation with Dr. Eran Maniv and Dr. Alon Ron. I am grateful for the school of Physics which has been my second home for the past decade. A big thanks to Prof. Roy Beck Barkai, Adir Vigder, Alon Rabinowicz, Matan Friedmann, Yakira Navaty, Gila Smaransky, Galia Netzer-Erlichmen, Ronit Yona, Prof. Yoram Dagan, Prof. Ady Arie, Prof. Alexander Palevski and Prof. Moshe Goldstein, who have helped and taught me more than they are probably aware. I am grateful to have been part of an institution that enabled me to establish *ShePhysics*, TAU's Women in Physics Society, and to meet and connect between strong female role models such as Dr. Michal Shaviv, Dr. Sivan Trajtenberg Mills and Roni Majlin Skiff.

I am forever indebted to my wonderful family - my parents Malka and Tsvika, and my sister Ziv, for always believing in me and helping me become who I am. Thanks dad, for telling me bedtime stories about paradoxes and planets, and thanks mom for practically forcing me to sign up for a bachelor's in Physics. Finally, I thank my husband Idan for his endless encouragement, support and love. Together, we can do anything. You and our son Alon are my guiding stars.

Funding

I would like to express my gratitude toward the Israeli Council for Higher Education Planning and Budgeting Committee for granting me a full three-year scholarship as an excellent PhD candidate in a High-Tech Field of Study. I am also thankful for the Marian Gertner Institute and the Tel Aviv University Center for Nanoscience and Nanotechnology for their financial support.

Contents

1 List of Publications, Oral Presentations and Awards

1.1 Peer-Reviewed Publications

1. H. Greener, M. Mrejen, U. Arieli, and H. Suchowski, "Multifrequency excitation and detection scheme in apertureless scattering near-field scanning optical microscopy," Opt. Lett. 42, 3157-3160 (2017)

2. H. Greener, H. Suchowski, “Composite Pulses in N-level Systems with SU(2) Symmetry and their Geometrical Representation on the Majorana Sphere,” J. of Chem. Phys. 148, 074101 (2018) (Featured on cover)

3. H. Greener, A. Vigder, S. Beck, R. Beck-Barkai, “Experiences in improving introductory physics labs,” Physics Today 71, 7, 12 (2018)

4. E. Kyoseva*, H. Greener*, H. Suchowski, “Detuning-modulated composite pulses for high-fidelity robust quantum control,” (*equal contribution) Physical Review A 100 (3), 032333 (2019)

5. T. Coen, H. Greener, M. Mrejen, L. Wolf, H. Suchowski, “Deep Learning based Reconstruction of Directional Coupler Geometry from Electromagnetic Near-Field Distribution” OSA Continuum 3 (8), 2222-2231 (2020)

6. H. Greener*, E. Kyoseva*, H. Suchowski, “Detuning-modulated universal composite pulses,” (*equal contribution) arXiv:2012.04401 **In review.**

1.2 Conference Presentations and Awards

Conference Presentations

1. Israel Physical Society (IPS) Annual Meeting, Oral Presentation, Feb. 2021
2. IPS Annual Meeting, Oral Presentation, WIS, Feb. 2020
3. QIMV: Quantum Technologies, Poster, Rome, Apr. 2019 E. Kyoseva, H. Greener, and H. Suchowski, "Detuning-modulated composite pulses for integrated photonic circuits," in Quantum Information and Measurement (QIM) V: Quantum Technologies, OSA Technical Digest (OSA, 2019), paper T5A.9.
4. Oasis7, Poster, Tel Aviv, Apr. 2019 Fred Chaoul Nano Workshop, Oral Presentation and poster, Dead Sea, Israel, Feb. 2019
5. Nanometa Conference, Oral Presentation, Seefeld, Tirol, Austria, Jan. 2019
6. CLEO Conference, Poster, San Jose, CA, USA, May 2018 H. Greener, M. Mrejen, U. Arieli, and H. Suchowski, "Multifrequency Near Field Scanning Optical Microscopy (MF-SNOM)," in Conference on Lasers and Electro-Optics, OSA Technical Digest (online) (OSA, 2018), paper JTh2A.66.
7. IPS Student Meeting, Oral Presentation, Acre, Israel, Mar. 2018
8. Gordon Research Conference: Quantum Control of Light and Matter, Poster, Mt. Holyoke, Mass., USA, Aug. 2017
9. FRISNO 2017, Poster, Ein Gedi, Israel, Mar. 2017
10. Oasis6, Poster (prize winner), Tel Aviv, Feb. 2017 UK-Israel Shaoul Fund IAS International Workshop: Emerging Applications of Nanostructures, Oral presentation, poster flash presentation (prize winner), TAU, Feb. 2017
11. IPS Annual Meeting, Oral Presentation, TAU, Dec. 2016
12. TAU LMI Center Opening Symposium, Poster flash presentation (prize winner), TAU, Oct. 2016
13. XIN Winter School: Physics at the Edge, Poster flash presentation, TAU, Jan. 2016
14. Materials and Mechanisms of Superconductivity, Poster, Geneva, Switzerland, Aug. 2015

Awards

1. 2019 Marian Gertner Institute Scholarship *Excellence in Research for PhD Candidates*
2. 2019 Tel Aviv University Center for Nanoscience and Nanotechnology Excellence Award *Excellence in Research for PhD Candidates*
3. 2018 Council for Higher Education Planning Budgeting Committee Scholarship *Full scholarship for excellent PhD Candidate in High-Tech Fields of Studies*
4. 2018 Nelis Hensen Tolpin Solomon Scholarship *Excellence in Research and Teaching for Junior Staff - in recognition of contribution to reformulating the 2nd year student laboratory.*
5. 2017 Wladimir Schreiber Scholarship *Excellence in Teaching for Junior Staff*
6. 2017 Oasis6 Conference Poster Competition *Second prize winner*
7. 2017 UK-Israel Shaoul Fund IAS International Workshop Poster Competition *First prize winner*
8. 2017 TAU LMI Center Opening Symposium Poster Competition *Prize winner*
9. 2016 KLA Tencor Scholarship *Excellence in Research and Teaching for Junior Staff*
10. 2015 Tel Aviv University Center for Nanoscience and Nanotechnology Travel Scholarship *Awarded a travel grant to an international conference*
11. 2015 Waidman Paul Scholarship *Excellence in Teaching for Junior Staff*

Introduction

2

> *A scientist in a laboratory is not merely a technician. She is also a child placed before natural phenomena which impress her like a fairy tale!*
>
> **— Marie Curie**
> (Nobel Prize Physicist)

The field of light matter interactions is a playground in which photons play a central role in both exciting and probing physical systems. The discoveries and breakthroughs in the field act as a feedback mechanism, pushing current limits of resolution, bandwidth, fabrication, therefore enabling even more discoveries and breakthroughs. Naturally, the field has exploded in the recent two decades. New cutting-edge fields, such as ultra-fast pulsed lasers, nano-scaled meta-materials, Silicon nanophotonics and sub-wavelength resolution imaging, have emerged, breaking barriers, reshaping experimental paradigms and leading current technologies. On an even more recent timescale, during the past five years, quantum technologies have steadily begun to leap over the boundary of a theoretical prospect and have become an achievable near-term goal.

During my PhD, I performed research on two fronts of light-matter interactions: near-field scanning optical microscopy (SNOM) with measurements of photo-induced phenomena in highly correlated electron systems, and composite pulses for quantum coherent control and quantum information processing (QIP). While there is no directly apparent link between these two research fronts, they cover two aspects of control of nanophotonic devices. My studies resulted in three first-authored published manuscripts, one second-authored publication and one first-authored publication that is currently in review.

In order to prepare the grounds for a broad study of dynamics in the near-field, I theoretically derived and experimentally applied a multifrequency near-field optical imaging method that results in enhanced sensitivity for the detection of weak near-field signals. In Chapter 2.1 of this work, I introduce scattering-type scanning near field optical microscopy (sSNOM), a non-invasive imaging technique, based on the atomic force microscope (AFM). Its spatial resolution is limited mainly by the apex of the probing tip (approximately 15nm), and by the inadequate discrimination of near-field optical signals from a much stronger far-field background. Thus, the achievement of high sensitivity in such measurements is an ongoing challenge. In publication 1, presented in Chapter 3.1, I theoretically derived and experimentally showed that this scheme allows for a two-fold enhanced sensitivity in the measurement of an optical near field signal as a function of tip-sample distance. Our

measurements of 500nm gold nanorods, with resolved optical features of the order of 7nm, imply that this enhanced sensitivity leads to an improved resolution in the x-y plane.

This technique, along with our lab's unique capability of 20fs temporal resolution, made it possible to probe structural and electro-optical inhomogeneities at the nanometer scale. Specifically, I chose to probe the underlying mechanisms of the photoinduced persistent conductivity amplification of the complex oxide interface, $LaAlO_3/SrTiO_3$. In currently unpublished results of this ongoing research, described in Chapter 4.1, I designed an experiment that clearly shows that the above phenomenon is well localized in $LaAlO_3/SrTiO_3$. The persistent photoconductivity at room temperature is a result of trapped electronic states between the layers of the two materials that do not transport via the 2DEG.

This knowledge, along with derived theories of quantum control, will enable the efficient coupling of such systems into photonic circuits, which are considered a candidate for solving current limitations of electronic devices. I detail the evolution of my research on composite pulses for quantum information processing in Chapter 2.2. In publication 2, provided in Chapter 3.2, which was featured on the cover of the Journal of Chemical Physics, I derived a general theory of composite pulses for higher order irreducible representation of SU(2) dynamics of N-level systems. Composite pulses are a series of pulses with specifically chosen phases, that compensate for the imperfections of a conventional single pulse. Thus their performance in steering a two-level system to a final state is feasible, accurate and robust. However, studies of such composite sequences impinged on multi-level systems have been lacking. The derivations of this work allow to tailor the dynamics of physical multi-level systems, without imposing the approximation to a two-state solution. The schemes result in high fidelity population transfer from any state of a multi-level system to its palindromic counterpart, which is robust to inaccuracies in both system and excitation parameters.

Furthermore, publication 3, featured in Chapter 3.3, details the derivation of a novel quantum control mechanism that can be implemented in any qubit architecture. Specifically, we developed a composite control scheme that takes into account systems with real coupling parameters, as previous schemes could only be implemented on systems with complex coupling parameters. Such systems include coupled waveguides, that are considered a strong contender for quantum information processing. I was awarded two merit-based scholarships of excellent research in 2019 for this work. In Chapter 4.2, I extend this scheme to create high-fidelity universal quantum gates. In both works, I translated the theoretical schemes to executable designs of integrated photonic waveguide couplers, which are patent pending. An ongoing collaboration between our group and Bar Ilan University will result in experimental demonstrations of the robustness of this technique.

The theoretical derivations of publication 3 and Chapter 4.2 provided a cornerstone for further collaborations I have participated in, including a deep-learning method to

reconstruct the geometry of the aforementioned coupled waveguide systems. Additionally, over the course of my PhD, I gained experience in mentoring undergraduate students and served as a junior advisor to their research projects. Among these, I guided and advised two students toward a nonlinear optics implementation of my theoretical work. These novel designs of nonlinear optics crystals are currently pending publication.

To summarize, this dissertation composed of published research papers is organized as follows. In Chapter 2, I provide a thorough introduction to my publications, which are enclosed in Chapter 3. Namely, in Chapter 2.1.1, I present an overview of SNOM, and lay out the details of my theoretical derivations of multifrequency SNOM, and describe the experimental setup in Chapter 2.1.2. In Chapter 2.2.1, I acquaint the reader with the foundations of composite pulses as a means to achieve quantum coherent control in two-level systems, and expand the landscape to multi-level systems with SU(2) symmetry. In Chapter 2.2.2, I propose harnessing the detuning parameter as a novel control knob for composite pulses, thus creating a composite pulse technique suitable for photonic integrated circuits. Further unpublished research is described in Chapter 4. Chapter 4.1 outlines the motivation and experimental setup and results of near-field measurements of persistent photoconductivity, while Chapter 4.2 is a comprehensive depiction of universal unitary detuning-modulated composite gates. Chapter 5 is a conclusion and outlook for future work.

2.1 Introduction to Near Field Optics and Dynamics

The basic experimental set-up in most optics research laboratories consists of a light source, either a continuous wave or pulsed laser, that illuminates a sample of interest. One can discover many physical properties of the sample, such as its absorption spectrum, by placing a detector behind the sample to measure the transmitted light and in an angle from it, to measure the reflected light. This technique enables one to obtain a spatial average of the sample's response to the light source. The fine details of the sample, such as a spatial inhomogeneity, cannot be resolved in this manner. This is due, of course, to Abbe's diffraction limit [1], that states that two features will not be resolved if the distance between them d is less than half the probing wavelength λ. Specifically, the limit is stated as:

$$d = \frac{\lambda}{2nsin\theta} \tag{2.1}$$

where $nsin\theta$ is the numerical aperture of the lens with which the object is being imaged in a medium with a refractive index of n. Namely, in far field optics, the evanescent fields created in a light-matter interaction do not propagate to the detector.

In the past few decades, tremendous progress has been made in optical imaging beyond the diffraction limit [2, 3, 4]. Near field microscopy has revolutionized this field, as it allows for noninvasive and nondestructive retrieval of deep sub-wavelength optical information, providing unprecedented information on optical properties of materials at the nanoscale [5, 6, 7, 8, 9, 10]. Thus the field has opened a window to phenomenon such as fundamental light-matter interactions, chemical reactions and transport in two-dimensional materials [11, 12, 13, 14, 15, 16, 17].

The apertureless version of the scattering near field scanning optical microscope (sSNOM) has expanded to the optical regime the topographic probing capabilities of the atomic force microscope (AFM). In traditional AFM, a cantilever with a sharp tip attached to it, is made to mechanically oscillate at its first flexural frequency. The tip is scanned over the surface of a sample of interest, and any deflection of it, caused by Van der Waals forces between the tip and sample, is monitored via a feedback mechanism, thus a topographical image can be formed. The sSNOM utilizes the AFM's sharp tip by dithering it in the proximity of a sample and illuminating it by focused light [18, 19, 20]. Owing to the nonlinearity of the light scattering process with respect to the tip-sample distance, high harmonic demodulation allows near field imaging with a spatial resolution mainly limited by the apex of the tip [18]. However, to date, a thoroughly background-free image necessitates implementing various schemes, such as pseudoheterodyne detection, an interferometric technique in which a phase modulated reference enables the extraction of the pure near field signal [21].

Here I will describe the theoretical basis of the model of sSNOM [18, 19, 20]. Employing a quasi-electrostatic approach for the tip-sample system, the tip is modeled

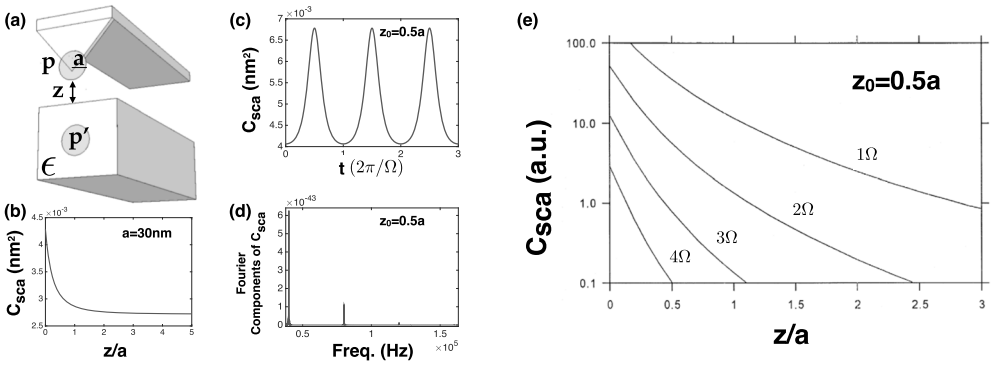

Fig. 2.1: Fundamentals of Near-Field Scanning Optical Microscopy. (a) Tip-sample system modelled as a polarized sphere p of radius a, oscillating at amplitude A at small distances z from sample of dielectric constant ϵ. (b) Scattering coefficient from a tip of radius $a = 30nm$ as a function of normalized tip-sample distance. (c) Scattering coefficient for a tip dithered at 40kHz, where the minimal tip-sample distance is half the radius of the tip. (d) Fourier transform of (c). (e) Fourier components of the scattering cross sections vs. minimum tip-sample distance when ditherting with a small modulation amplitude of half the tip radius (borrowed from [18]).

as a sphere of radius r and polarizability α, which is imaged in a sample of dielectric constant ϵ, set at a distance of z away from the tip, as shown in Figure 2.1(a). When applying an electric field, the tip is polarized with a dipole moment $p = \alpha E$ polarized perpendicular to the sample's surface, thus the electric field of the induced probe dipole is $E_{dipole} = \frac{p}{2\pi r^3}$. This induces surface charges on the sample whose fields can be described by use of the method of images. These image dipoles have a dipole moment $p' = \beta p$, where $\beta = (\epsilon - 1)(\epsilon + 1)$, which enhances the field at the probe dipole as:

$$p = \alpha(E + \frac{p'}{16\pi r^3}) \tag{2.2}$$

where $r = z + a$. Therefore, the effective polarizability is:

$$\alpha_{eff} = \frac{\alpha(1+\beta)}{1 - \frac{\alpha\beta}{16\pi r^3}} \tag{2.3}$$

with $\alpha = 4\pi r^3(\epsilon_p - 1)(\epsilon_p + 2)$, where ϵ_p is the dielectric constant of the tip. This enhancement is only significant at short distances $z < r$.

Now we apply Mie scattering theory, to calculate the electromagnetic field scattering cross-section of the probe tip

$$C_{scatt.} = \frac{k^4}{6\pi}|\alpha_{eff}|^2 \tag{2.4}$$

assuming the tip's radius is smaller than the illuminating wavelength [18]. This scattering cross-section, which is the origin of the weak near field signal of interest, is a non-linear function of the distance between the probe and sample, by virtue

of α_{eff}, as seen in Figure 2.1(b). Varying the tip-sample distance with time leads to a significant modulation of the above near-field scattering coefficient from the tip, while the scattered light from the cantilever body remains constant [22]. This is shown explicitly in Figure 2.1(c), where we calculate the scattering cross-section from a tip dithered at a frequency of 40kHz as a function of time for a minimal tip-sample distance of $z_0 = 0.5a$, where $a = 30nm$. A Fourier transform of this anharmonic function produces Figure 2.1(d), the Fourier components of the above. Figure 2.1(e), borrowed from [18], shows the Fourier components of the scattering cross-section as a function of the minimum tip-sample distance, when the tip is dithered with a small modulation amplitude of $z_0 = 0.5a$. Here one sees that by demodulating the detected scattered signal at the higher harmonic frequencies of the cantilever's motion, one achieves a narrower cross-section, with a more abrupt change of signal, as the tip approaches the sample. This is equivalent to effectively sharpening the probe tip. Nevertheless, while this process results in higher near field sensitivity to optical measurements, there is a trade-off, since the measured signal becomes significantly weaker at higher harmonic frequencies.

2.1.1 Multifrequency Excitation and Detection in SNOM (MFSNOM)

In this section, I will provide an introduction to the findings of increased near field optical sensitivity and background suppression of the detected signal in an experimental realization of a multifrequency sSNOM technique [23]. It has been previously shown in the atomic force microscopy community [24, 25] that mechanically exciting the AFM cantilever at two or more of its first flexural modes results in enhanced force sensitivity and improved resolution to topographic images [26]. The coupling between the two mechanical modes is at the origin of this so-called multifrequency AFM sub-atomic spatial resolution, as the higher harmonics of the first mode acts as an effective driving force for its higher eigenmodes [27].

In our research, we formulated a theoretical model, based on the bi-modal excitation of the AFM tip as described in Figure 2.2(a) and a multifrequency detection scheme in SNOM (MF-SNOM), schematically shown in Figure 2.2(b). It predicts a set of experimental parameters relevant for the suppression of optical background in the detected signal. We observe that in the multimodal excitation method, the solution space for these parameters spreads over a two-dimensional plane, thus allowing further degrees of freedom in near-field measurements. We experimentally show that this scheme allows for a further enhanced sensitivity in the measurement of a near field signal as a function of tip-sample distance. This z-axis sensitivity is directly related to the in-plane spatial resolution in such measurements [28]. From our findings, we see that this enhanced sensitivity seems to lead to an improved resolution in the x-y plane. We believe that this is a feasible method that will allow for enhanced sensitivity, improved resolution and background-free near field images.

In order to gain a more intuitive understanding of the above in the context of multifrequency tip excitation, we employed a simplified scattering model [30] to express the bi-modal near field scattering amplitude as a function of the the bi-modal motion of the tip at its first two flexural frequencies $f_1 = \omega/2\pi$ and $f_2 = \omega'/2\pi$, represented by $z(t) = Acos(\omega t) + Bcos(\omega' t)$.

The detected signal function is the sum of the near-field scattering amplitude $K[z(t)] = exp\{-z(t)/d\}$, where d is the typical distance for which the near-field term decays, and a z motion artifact, due to optical interference (background) $W[z(t)] = sin[\frac{4\pi z}{\lambda} + \frac{\pi}{4}]$. Thus, the detected signal function is a sum of the above $S(t) = W(t) + bK(t)$, where b is the scattering weight, dependent on the scaling of the scatterer volume, which in our case, is the spherical tip. For the multifrequency case:

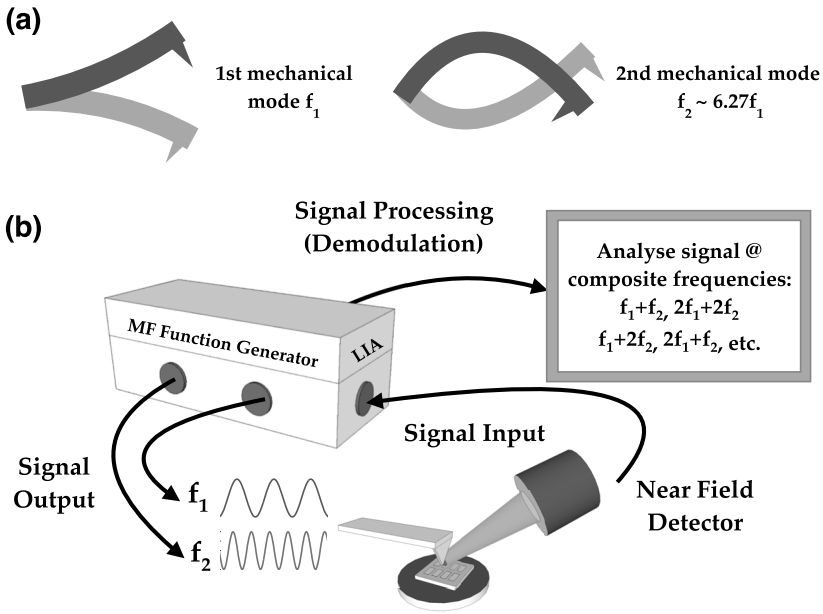

Fig. 2.2: Schematic experimental set-up of Multifrequency Near Field Scanning Optical Microscopy. (a) Simultaneous bi-modal excitation of cantilever in multifrequency near field scanning optical microscopy at two first flexural frequencies, where commonly $f_2 \approx 6.27 f_1$ [29]. (c) Scheme of experimental set-up.

$$
\begin{aligned}
z(t) &= A\cos(\omega t) + B\cos(\omega' t) \\
S(t) &= \sin\left[\frac{4\pi}{\lambda} A\cos(\omega t) + \frac{4\pi}{\lambda} B\cos(\omega' t)\right] + b e^{-(A\cos(\omega t)+B\cos(\omega' t))/b} \\
&= \frac{1}{\sqrt{2}} \sin\left[\frac{4\pi}{\lambda} A\cos(\omega t)\right] \left\{\cos\left[\frac{4\pi}{\lambda} B\cos(\omega' t)\right] - \sin\left[\frac{4\pi}{\lambda} B\cos(\omega' t)\right]\right\} \\
&+ \frac{1}{\sqrt{2}} \cos\left[\frac{4\pi}{\lambda} B\cos(\omega' t)\right] \left\{\sin\left[\frac{4\pi}{\lambda} B\cos(\omega' t)\right] + \cos\left[\frac{4\pi}{\lambda} B\cos(\omega' t)\right]\right\} \\
&+ b e^{-(A\cos(\omega t)+B\cos(\omega' t))/b}
\end{aligned}
$$

Here we can assume that the tip oscillation amplitudes A and the typical distance for near field decay are much smaller than the illuminating wavelength, and expand the signal to order $O(x^4)$. Separating the different frequency terms leads to a series of the different coefficients detectable via a lock-in amplifier, such as:

$$
\begin{aligned}
S(t) &\approx DC \\
&+ \left[\frac{1}{\sqrt{2}}\frac{4\pi}{\lambda} - \frac{b}{d}\right] A cos\left(\omega t\right) \\
&- \frac{1}{2}\left[\frac{1}{\sqrt{2}}\left(\frac{4\pi}{\lambda}\right)^2 + \frac{b}{d^2}\right] AB cos\left[\left(\omega + \omega'\right) t\right] \\
&- \left[\frac{1}{\sqrt{2}}\left(\frac{1}{2}\frac{4\pi}{\lambda}\right)^2 + \frac{1}{4}\frac{b}{d^2}\right] A^2 cos\left(2\omega t\right) \\
&+ \left[\frac{1}{\sqrt{2}}\left(\frac{1}{2}\frac{4\pi}{\lambda}\right)^4 + \frac{1}{32}\frac{b}{d^4}\right] A^2 B^2 cos\left[\left(2\omega + 2\omega'\right) t\right] \\
&+ \left[\frac{1}{\sqrt{2}}\frac{4}{3}\left(\frac{4\pi}{\lambda}\right)^4 + \frac{1}{192}\frac{b}{d^4}\right] A^4 cos\left(4\omega t\right)
\end{aligned}
$$

If we define an optical contrast factor R_n as the ratio between the scattering term in each coefficient that decays as $1/d^n$ and the background artifact that scales as $1/\lambda^n$ of each n harmonic demodulated signal, the advantage in detecting the signal at certain frequencies in comparison to others becomes clear. The enhancement in R_n for higher orders of n leads to increased sensitivity to near-field signal, compared to the optical background. From this point forth, we will refer to detection at a certain harmonic n as *demodulation*. We show this explicitly by assuming that for large tip-sample distances, such as $d = 50nm$, the near-field scattering term in R_1 is of the order of the background term, thus:

$$
\begin{aligned}
b &= \frac{4\pi d}{\sqrt{2}\lambda} \\
R_1 &= 1
\end{aligned}
$$

and for the second order optical contrast factor:

$$
R_2 = \frac{b}{d^2}\frac{\sqrt{2}\lambda}{16\pi^2} = \frac{4\pi d}{\sqrt{2}\lambda}\frac{1}{d^2}\frac{\sqrt{2}\lambda}{16\pi^2} = \frac{\lambda}{4\pi d} = \frac{780nm}{4\pi 50nm} = 1.24
$$

This demodulation term is only enhanced by a factor or 1.24 compared to R_1. Now we perform the same calculation for shorter tip-sample distances. For example, if $d = 10nm$ we can assume a significant near field scattering term. Since b scales with the volume of the scattering particle d^3 meaning that $\frac{b}{d^3} \sim const$ we could calculate a new scattering weight b, according to its previously calculated value

λnm	$\frac{R_{2\omega}}{R_{\omega}}$	$\frac{R_{4\omega}}{R_{2\omega}} = \frac{R_{2(\omega+\omega')}}{R_{\omega+\omega'}}$
660	5.25	27.6
1200	9.5	91.7
1580	12.5	160

Tab. 2.1: Calculated values of the optical contrast enhancement for demodulation at different harmonics of the mono-modal and bi-modal excitation frequencies for specified illuminating wavelengths.

$$\begin{aligned} \frac{b}{d^3} &= \frac{0.57}{50nm^3} = \frac{b}{10nm^3} \Longrightarrow b = 4.56 \times 10^{-3} \\ R_1 &= 0.04 \\ R_2 &= 0.248 \end{aligned}$$

This time, the second harmonic signal is enhanced six-fold compared to the first, which is a significant enhancement of the near-field signal compared to the optical background.

A numerical calculation of the values of R_n as a function of illuminating wavelength for different values of n in the mono-modal case and in the bi-modal case leads to a practical result. We find that implementing the bi-modal excitation method allows to obtain the same values of this optical contrast factor with demodulation at lower harmonics of the sum of the bi-modal frequencies. Namely, the optical contrast obtained via mono-modal excitation and demodulation at $n = 2\omega$ is the same as that achieved via bi-modal excitation and demodulation at $n' = \omega + \omega'$. A few values of these enhancement factors are shown in Table 2.1.

For the case of bi-modal tip excitation, we find a clear advantage in demodulating the detected signal at certain frequencies in comparison to others. For example, demodulation at the second harmonic of the sum of the two frequencies $2(\omega + \omega')$ at an illuminating wavelength of 1580nm leads to a 160 fold contrast enhancement, compared with demodulation at the first harmonic of the sum of these two frequencies. This is the same enhancement achieved in mono-modal excitation while demodulating the detected signal at the fourth harmonic of the tip oscillation frequency, compared with demodulation at the second harmonic of this single frequency.

Similarly, the same near field detection enhancement is predicted to occur for bi-modal excitation and demodulation at $2\omega + \omega'$ and for mono-modal excitation and demodulation at 3ω. Namely, we can achieve high optical contrast for lower demodulation frequencies, thus obtain a stronger signal.

An additional advantage in multifrequency excitation SNOM is the wider range of tip oscillation amplitudes suitable for eliminating far-field background from the near-field signal. This could be achieved by expanding the finding [31] that the total intensity of the signal measured by the detector in a mono-modal SNOM

setup produces a non-vanishing background term at all n harmonics of the signal, which is directly proportional to $J_n(2ka)$. In this term, a is the single tip oscillation amplitude, and k is the wave vector of the illuminating field. In order to suppress the background, one must choose a in a way that mathematically nullifies this term.

In order to begin this derivation, we define three electromagnetic fields that take part in the SNOM measurement setup and are considered "optical background" (as opposed to the optical near-field signals). These are the field backscattered by the tip shaft E_F , the back reflection of the sample E_S, and the light reflected back by the lens E_L, where:

$$\begin{aligned} E_F &= E_F^0 e^{-i\Delta\phi_{FL}} \\ E_S &= E_S^0 e^{-i\Delta\phi_{SL}} \\ E_L &= E_L^0 \end{aligned} \tag{2.5}$$

and the phases $\Delta\phi_{iL}$ are related to the optical path differences accumulated by the fields scattered from the tip and by the sample with respect to the one scattered by the lens, in their travel from the laser to the detector:

$$\begin{aligned} \Delta\phi_{FL} &= 2k\left[l_0 - a(t)\right] \\ \Delta\phi_{SL} &= 2k\left[l_0 - z(t)\right] \end{aligned} \tag{2.6}$$

The total intensity measured by the detector in the SNOM setup is:

$$\begin{aligned} BKG &= |E_F + E_S + E_L|^2 \\ &= |E_F|^2 + |E_S|^2 + |E_L|^2 \\ &+ 2Re\left(E_F^* E_S\right) + 2Re\left(E_F^* E_L\right) + 2Re\left(E_L^* E_S\right) \end{aligned} \tag{2.7}$$

One can easily show that given

$$\begin{aligned} z(t) &= z_0 + \Delta z(t) \\ C_0 &= |E_F|^2 + |E_S|^2 + |E_L|^2 \\ B_{FS} &= 2|E_F E_S| \\ B_{FL} &= 2|E_F E_L| \\ B_{SL} &= 2|E_S E_L| \\ \phi_0 &= 2kl_0 \\ \phi_1 &= 2k\left(l_0 - z_0\right) \\ \phi_2 &= 2kz_0 \end{aligned}$$

the background could be written as

$$
\begin{aligned}
BKG &= C_0 + \left[B_{FS} cos\left(\phi_2 + 2k\Delta z(t)\right) + B_{FL} cos\phi_0\right] cos\left(2ka(t)\right) \\
&+ \left[B_{FS} sin\left(\phi_2 + 2k\Delta z(t)\right) + B_{FL} sin\phi_0\right] sin\left(2ka(t)\right) \\
&+ B_{LS} cos\left(\phi_1 - 2k\Delta z(t)\right)
\end{aligned}
$$

which is the sum of a DC signal with a series of harmonics with amplitudes that depend on both the tip vibration amplitude and its distance from the sample.

In order to extend this to the multifrequency SNOM case, we use the Jacobi-Anger relations for real-valued expressions [32]:

$$
\begin{aligned}
cos\left(\gamma cos\theta\right) &= J_0\left(\gamma\right) + 2\sum_{n=1}^{\infty}\left(-1\right)^n J_{2n}\left(\gamma\right) cos\left(2n\theta\right) \\
cos\left(\gamma cos\theta\right) &= 2\sum_{n=0}^{\infty}\left(-1\right)^n J_{2n+1}\left(\gamma\right) cos\left[\left(2n+1\right)\theta\right]
\end{aligned}
$$

and plug in the bi-modal tip oscillation amplitudes

$$
a(t) = a_1 cos\left(\omega_1 t\right) + a_2 cos\left(\omega_2 t\right)
$$

such that

$$
\begin{aligned}
cos\left(2ka(t)\right) = & \\
& \left[J_0\left(2ka_1\right) + 2\sum_{n=1}^{\infty}\left(-1\right)^n J_{2n}\left(2ka_1\right) cos\left(2n\omega_1 t\right)\right] \times \\
& \left[J_0\left(2ka_2\right) + 2\sum_{n=1}^{\infty}\left(-1\right)^n J_{2n}\left(2ka_2\right) cos\left(2n\omega_2 t\right)\right] \\
- & \left[2\sum_{n=0}^{\infty}\left(-1\right)^n J_{2n+1}\left(2ka_1\right) cos\left[\left(2n+1\right)\omega_1 t\right]\right] \times \\
& \left[2\sum_{n=0}^{\infty}\left(-1\right)^n J_{2n+1}\left(2ka_2\right) cos\left[\left(2n+1\right)\omega_2 t\right]\right]
\end{aligned}
$$

and

$$
\begin{aligned}
sin\left(2ka(t)\right) &= \left[2\sum_{n=0}^{\infty}\left(-1\right)^{n}J_{2n+1}\left(2ka_1\right)cos\left[\left(2n+1\right)\omega_1 t\right]\right]\times \\
&\quad \left[J_0\left(2ka_2\right)+2\sum_{n=1}^{\infty}\left(-1\right)^{n}J_{2n}\left(2ka_2\right)cos\left(2n\omega_2 t\right)\right] \\
&+ \left[J_0\left(2ka_1\right)+2\sum_{n=1}^{\infty}\left(-1\right)^{n}J_{2n}\left(2ka_1\right)cos\left(2n\omega_1 t\right)\right]\times \\
&\quad \left[2\sum_{n=0}^{\infty}\left(-1\right)^{n}J_{2n+1}\left(2ka_2\right)cos\left[\left(2n+1\right)\omega_2 t\right]\right]
\end{aligned}
$$

Thus, the background term of the DC component in the bimodal case is:

$$
\begin{aligned}
BKG_0(a_1,a_2,\Delta z) &= C_0 + B_{SL}cos\left[2k\Delta z(t)-\phi_1\right] \\
&+ \left[B_{FS}cos\left(\phi_2+2k\Delta z(t)\right)+B_{FL}cos\phi_0\right]\left[J_0\left(2ka_1\right)J_0\left(2ka_2\right)\right] \\
&+ 0
\end{aligned}
\tag{2.8}
$$

Since $B_{FS} \gg B_{SL}$, the prevalent term of equation 2.8 will be a *product* of two Bessel functions:

$$
BKG_0 \propto J_0\left(2ka_1\right)J_0\left(2ka_2\right)
$$

Thus, generalizing this analytic derivation to the bi-modal excitation technique results in an extension of the available solutions for background suppression from a single tip oscillation amplitude to a two-dimensional plane of possible sets of the two oscillation amplitudes for each mode of excitation. This is derived from the fact that the new background term for all harmonics is proportional to the product of two Bessel functions:

$$
BKG_n \propto J_n\left(2ka_1\right)\times J_n\left(2ka_2\right) \tag{2.9}
$$

In this case, the solution space expands, and one is free to choose from a set of available tip oscillation amplitudes a_1 and a_2, in order to completely cancel this term. It should be stressed once again that here, the signal should be demodulated at the composite harmonics of the two mechanical frequencies of the tip.

2.1.2 Experimental Setup of MFSNOM

In order to examine optical near-field measurements with the multifrequency SNOM technique, we used plasmonic nanostructure arrays, comprised of Au nanobars and split ring resonators (SRR). These were fabricated via standard electron beam lithography, and deposited with a height of 100nm on an ITO substrate. The near-

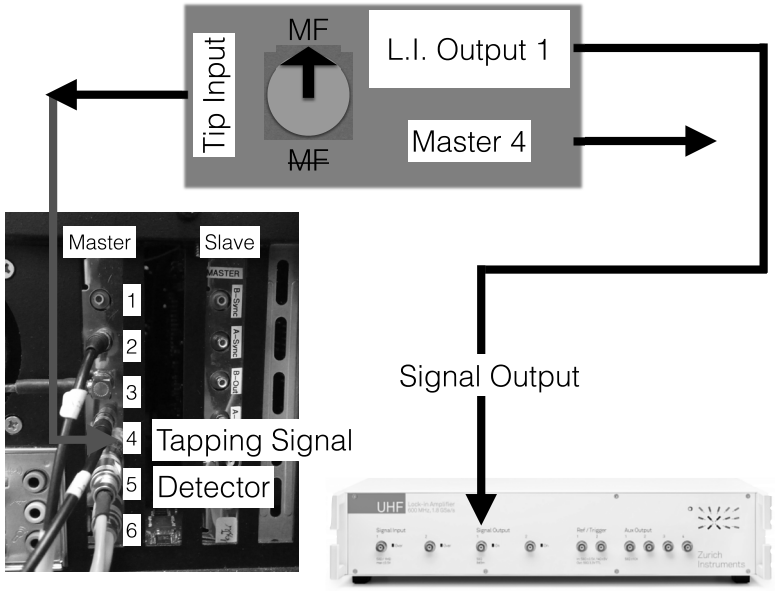

Fig. 2.3: Multifrequency SNOM excitation technical setup. See text for details.

field measurements were done using a NeaSpec neaSNOM, illuminated with a tunable CW laser (Toptica CTL1550) between 1550-1580nm. We used a Zurich Instruments UHF Lock-in Amplifier, with its many available oscillators, to externally drive the AFM cantilever on the one hand, and to demodulate the detected scattered signal at any frequency of our choice on the other hand. Figure 2.2(b) depicts a schematic representation of the experimental set-up.

Below are the technical details for setting up a multifrequency excitation and detection experiment. In Fig. 2.3 I show how I connect the signal output of the UHFLI to a switch that toggles between the multifrequency and mono-modal excitation. The switch inputs to the tip the UHFLI signal output by connecting it directly to input 4 of the master board of the NeaSpec, which is the tapping signal. In Fig. 2.4, output 5 of the master board of the NeaSpec, which is the SNOM signal, is split to the optical detector and to the signal input of the UHFLI, where it is demodulated at the relevant frequencies according to the above theory. The two auxillary outputs of the UHFLI are connected to input 5 and 6 of the NeaSpec slave board, that are detected and processed as separate image channels on the NeaSpec software.

I refer the reader to publication 1 [23] in Chapter 3.1, for a detailed description of my experimental results and analysis.

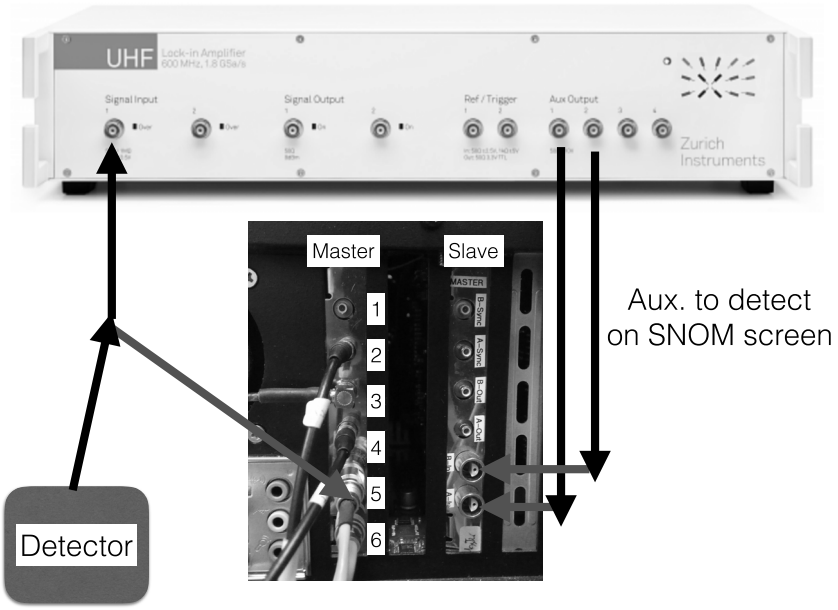

Fig. 2.4: Multifrequency SNOM detection technical setup. See text for details.

2.2 Introduction to Composite Pulses for Quantum Coherent Control

Quantum coherent control is a field of research which aims to solve the problem of efficiently steering a quantum system from an initial state to a final state. Such complete population transfer (CPT) has been the focus of extensive research these past few decades. This is generally achieved by shaping the duration and area of an electromagnetic pulse impinged on a system in order to excite it, and by employing various techniques ensuring this excitation is robust to inaccuracies in the system parameters and the pulse shape itself. Such control is desired for obtaining high fidelity in quantum computation and quantum information processing [33, 34], coherent manipulation of population inversion in atomic and molecular quantum systems [35, 36, 37, 38], directional optical waveguides [39] and spin control in nuclear magnetic resonances [40].

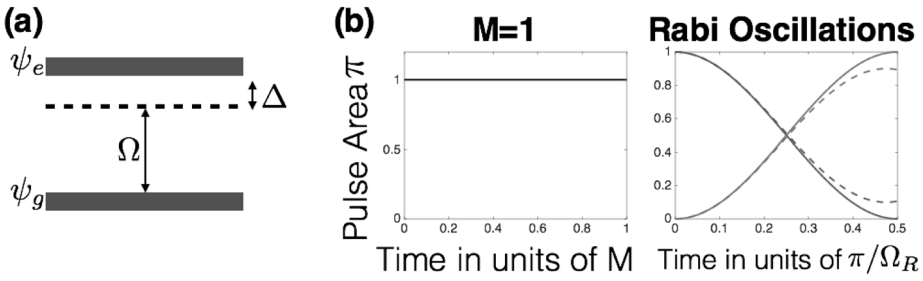

Fig. 2.5: Dynamics of a two-level system. (a) A general two-level coupled system, with a ground ψ_g and excited ψ_e level, coupling between adjacent levels Ω and detuning Δ. (b) Left: A single pulse on a two-level system with zero detuning leads to Rabi oscillations. Right: The intensity evolution of the system for the initial condition $\psi_1 = (1, 0)$. Solid line: Pulse area A. Dashed line: Same pulse area with detuning of $\Delta = \pi/15$.

To state the general problem, we consider a two-level system, shown in Fig. 2.5(a) with a Rabi frequency for electric dipole transitions $\Omega(t)$. One can excite this system by using a laser with a frequency ω_L that is not the exact frequency of the energy gap ω in this two-level system. Thus, we introduce the detuning parameter $D(t) = \int_{t_0}^{t} \Delta(t')dt'$ where $\Delta = \omega - \omega_L$. The coherent dynamics of this qubit system $\{|1\rangle, |2\rangle\}$ is described by the time-dependent Schrodinger equation [35]:

$$i\hbar\partial_t \begin{bmatrix} c_1(t) \\ c_2(t) \end{bmatrix} = \frac{\hbar}{2} \begin{bmatrix} -\Delta(t) & \Omega(t) \\ \Omega^*(t) & \Delta(t) \end{bmatrix} \begin{bmatrix} c_1(t) \\ c_2(t) \end{bmatrix}. \tag{2.10}$$

For time-independent coupling, one can perform a unitary transformation to introduce the unitary propagator of this operation:

$$U(\delta t) = \begin{bmatrix} \cos\left(\frac{A}{2}\right) + i\frac{\Delta}{\Omega_g}\sin\left(\frac{A}{2}\right) & -i\frac{\Omega}{\Omega_g}\sin\left(\frac{A}{2}\right) \\ -i\frac{\Omega}{\Omega_g}\sin\left(\frac{A}{2}\right) & \cos\left(\frac{A}{2}\right) - i\frac{\Delta}{\Omega_g}\sin\left(\frac{A}{2}\right) \end{bmatrix}. \tag{2.11}$$

with the generalized Rabi frequency $\Omega_g = \sqrt{\Omega^2 + \Delta^2}$ and $A = \Omega_g t$, the pulse area, which is a product of the generalized Rabi frequency with time.

By impinging the system with a constant resonant pulse ($\Delta = 0$), one achieves the well-known Rabi oscillations [41]. Thus, in order to achieve complete population transfer from the ground state to the excited state of a two-level system, one can apply a so-called π-pulse, seen in Fig. 2.5(b). The solid blue and red lines in Fig. 2.5(b) show complete population inversion of two levels, while the dashed lines show a decreased fidelity, due to a detuning of $\pi/15$, in units of the coupling, between the excitation laser frequency and the Rabi frequency of the system. From this example, it is clear that this solution is very sensitive to experimental constraints. Namely, the state transfer, or the fidelity of the operation, is affected by errors in the target parameters, which include the coupling, detuning and pulse area. For this reason, other analytic time dependent methods were derived for precise state transfer. These include the Landau-Zener, Rosen-Zener and Allen-Eberly models [42, 43, 35], which allow for an adiabatic solution for very robust population inversion of a two-level system. These examples require very long and precise manipulation of the system and excitation parameters, which are not always feasible under experimental consequences.

Another well-known class of analytical solutions available for robust population inversion of two-level quantum systems are composite pulses. Composite pulses are a sequence of pulses with specifically chosen phases, commonly used in nuclear magnetic resonance (NMR), and for broadband population inversion by ultrashort pulses [44, 45, 46, 47, 48, 49, 50, 51], which overcome experimental constraints and relax the need for a perfect system and excitation mechanism. Since NMR spectroscopy requires precise pulse excitation for spin population inversion, attention was turned to designing composite sequences to compensate for conventional single pulse imperfections [52]. These may be due to spatial inhomogeneity, resonance offset and bandwidth. Thus the performance of composite pulses in guiding a system to a final state is feasible, accurate and robust. The traditionally quintessential composite pulse sequence is Levitt's widely used spin population inversion schemes for NMR excitation [48]. This composite pulse enables a two-level spin $j = \frac{1}{2}$ system to undergo accurate excitation, regardless of the pulse or system's imperfections, by steering the system step-wise through three pulses described by a total propagator

$$U_{Total} = U_3 U_2 U_1 \tag{2.12}$$

where each ingredient propagator is calculated according to eq. 2.11 with complex coupling parameters $\Omega_i = A_i e^{-i\phi_i}$, where $i = 1, 2, 3$. Each ingredient pulse has a specifically chosen pulse amplitude and phase to correct for errors.

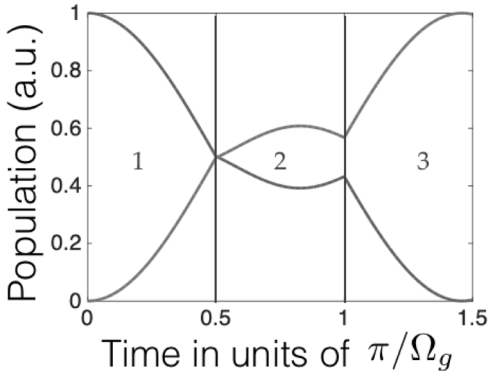

Fig. 2.6: Complete population transfer in two-level system with detuning of $\Delta = \pi/15$, in units of the coupling, by three-piece composite pulse sequence for nuclear magnetic resonance.

$$\begin{aligned} A_1 &= \tfrac{\pi}{2} \qquad \phi_1 = 0 \\ A_2 &= \pi \qquad \phi_2 = \tfrac{\pi}{2} \\ A_2 &= \tfrac{\pi}{2} \qquad \phi_3 = 0 \end{aligned} \tag{2.13}$$

Continuing our example of a two-level system with detuning $\Delta = \pi/15$, in units of the coupling, this self-correcting composite pulse sequence leads to complete population inversion, as seen in Fig. 2.6.

This scheme has since opened a wide variety of different composite pulse sequences, that revolutionized the field of NMR and its applications. While Levitt's composite solution, which is comprised of pulses with rectangular temporal shape, is suitable for NMR experiments, it fails to maintain its efficient nature for pulses of ultrashort timescales. Thus a different composite pulse scheme was suggested by Torosov *et al.* [53, 54] for pulse envelopes of smooth temporal shape , such as Gaussian pulses. Using these solutions, one can accurately excite two-level optical systems by tailoring the phases of a composite ultrashort pulse sequence regardless of the exact ingredient pulse shapes.

This was done by solving for a sequence of N pulses of area A_k (where A was popularly chosen to remain constant at $A = \pi$) and phases ϕ_k.

$$U^N = U_{\phi_N}(A_N)...U_{\phi_1}(A_1) \tag{2.14}$$

where each ingredient propagator reads

$$U_\phi(A) = \begin{bmatrix} a & be^{-i\phi} \\ -b^* e^{i\phi} & a^* \end{bmatrix} \tag{2.15}$$

for the Cayley-Klein parameters $a = cos(\frac{A}{2})$ and $b = -isin(\frac{A}{2})$. For instance, a broadband composite sequence is achieved for:

$$\phi_k^N = (N + 1 - 2\left\lfloor \frac{k+1}{2} \right\rfloor)\left\lfloor \frac{k}{2} \right\rfloor \frac{\pi}{N} \tag{2.16}$$

where the square brackets denote the floor value of $\lfloor (k+1)/2 \rfloor$ and $\lfloor k/2 \rfloor$.

Here, the $k = 1, ..., N$ pulses nullify the first $2N-1$ derivatives of the off-diagonal element of the total propagator at $A = \pi$. Thus the total infidelity is of the order of $O(\epsilon^{2N})$.

Generally speaking, in most traditional phase-modulated composite pulses, the infidelity, or total pulse error is mitigated as a function of the total number of pulses. This creates a trade-off between the total length of the composite pulse sequence and its infidelity.

In Chapter 2.2.1, I will present an extension of composite pulses sequences to N-level systems with SU(2) symmetry. In Chapter 2.2.2, I will provide a rigorous derivation of a novel class of detuning-modulated composite pulses. Due to the required organization of this dissertation, my unpublished work on a comprehensive derivation and study of universal detuning-modulated composite gates is presented in Chapter 4.2.

2.2.1 Composite Pulses in N-level Systems with SU(2) Symmetry

Despite the broad implementation of the above-mentioned schemes for two-level systems, studies of the multi-level case have remained sparse in the field of NMR [55, 52], atomic and optical systems. A handful of schemes have been suggested for the evolution of multi-level systems, such as adiabatic elimination, Electromagnetically-Induced-Transparency, stimulated Raman adiabatic passage (STIRAP) and the Landau-Zener picture [56, 57, 58, 59, 60, 61]. These have been thoroughly studied to achieve the controlled evolution of a three-level system to a chosen final state. The Morris-Shore transformation has been used [62, 63] to reduce a multilevel system composed of N degenerate ground states and one excited state to an effective two-level system with exact analytic solutions. Yet all of these require the fine-tuning of experimental parameters in order to achieve efficient population inversion between the ground state and the excited state.

Cook, Shore and Hioe [64, 65] introduced a method of exciting an N-level system with SU(2) symmetry, to achieve an extension of Rabi oscillations between palindromic states. SU(2) is the special unitary Lie algebra group of $2x2$ matrices with a determinant value of 1. Mathematically, these are defined as

$$\begin{matrix} [a & be^{-i\phi} \\ -b^* e^{i\phi} & a^* \end{matrix} \tag{2.17}$$

where $\alpha, \beta \in$ and $|\alpha|^2 + |\beta|^2 = 1$. This group is isomorphic to the special orthogonal group of order 3, or SO(3), which represents rotations on a sphere. Pauli matrices are a useful basis in SU(2) to describe the dynamics of two-level physical systems

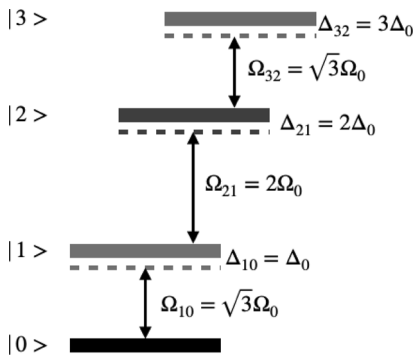

Fig. 2.7: Example of a four-level system with non-degenerate levels and SU(2) symmetry.

such as molecules and spins, as well as the energy transfer between a coupled waveguide photonic system, as I will discuss in a later chapter.

I now expand the composite pulse schemes developed for NMR and ultrashort temporal pulses to the general case of an N-level system with SU(2) symmetry. We consider non-degenerate levels, in which the diagonal elements of the Hamiltonian representing the system's dynamics are the cumulative detunings Δ_n of the excitation laser frequency from each Bohr frequency, and the off-diagonal elements link the different dipole transition moments between each two adjacent levels to the exciting electric field amplitude whose carrier frequency matches the Bohr frequency of this exact transition, namely Ω_n (i.e. the Rabi frequency for a transition between two adjacent levels). A variety of N-level solutions has been presented over the years, and in our manuscript, we refer to the Jacobi solution, given by $\Omega_n = \Omega_0\sqrt{n(N-n)}$ and $\Delta_n = n\Delta_0 + D_0$. By using the irreducible matrix representation for SU(2) symmetry it was shown [65] that these off-diagonal elements are not equidistant.

For example, consider the four-level system in Fig. 2.7. One can illuminate this system and excite one of three level pairs, with one of three fields: $\epsilon_{L1}(t) = A_{L1}e^{i\omega_{L1}t}$ with detuning $\Delta_1 = \omega_{L1} - \omega_{10}$, $\epsilon_{L2}(t) = A_{L2}e^{i\omega_{L2}t}$ with detuning $\Delta_2 = \omega_{L2} - \omega_{21}$ or $\epsilon_{L3}(t) = A_{L3}e^{i\omega_{L3}t}$ with detuning $\Delta_3 = \omega_{L3} - \omega_{32}$. In this case, the Rabi frequencies are $\Omega_1 = 2A_{L1}(t)d_{10}/\hbar$, $\Omega_2 = 2A_{L2}(t)d_{21}/\hbar$, and $\Omega_3 = 2A_{L3}(t)d_{32}/\hbar$. Assuming the Jacobi solution, and choosing $D_0 = 0$, we set the excitation laser frequencies, such that the detunings are $\Delta_1 = \Delta_0$, $\Delta_2 = 2\Delta_0$ and $\Delta_3 = 3\Delta_0$. One can also chose the values of A to comply with the Rabi frequencies in this solution are $\Omega_1 = \sqrt{3}\Omega_0$, $\Omega_2 = 2\Omega_0$ and $\Omega_3 = \sqrt{3}\Omega_0$.

Thus, systems that portray SU(2) symmetry enable one to express the Hamiltonian of the N-level system in a compact and generalized form, and generally the levels are not constrained to be equal. Many physical systems portray these symmetries (e.g. topological insulators and $p_x + ip_y$ superconductors), thus the conditions of the following derivations may be useful in the future for exciting such systems.

Furthermore, little composite pulse sequences have been derived for N-level systems in the past [55]; this has led us to derive a generalization of the NMR spin inversion scheme to a spin j system, displaying SU(2) symmetry. In the case of a magnetically

excited two-level system, the spacings between the levels are known to be equal. The Hamiltonian which describes such $N = 2j + 1$-level systems exists in a space spanned by the generators of the SO(3) group:

$$\hat{H} = Re(\Omega)\hat{\sigma_x} + Im(\Omega)\hat{\sigma_y} + \Delta\hat{\sigma_z} \tag{2.18}$$

where σ_i are the Pauli matrices of spin j. These dynamics can be geometrically described by trajectories on the so-called Majorana sphere [66], a generalization of the Bloch sphere for N-level systems with SU(2) symmetry.
In publication 2, presented in Chapter 3.2, I lay out a full derivation of the dynamics of an N-level system, coherently driven by composite pulses. The paper includes a lengthy introduction, along with a thorough description of the Majorana geometric representation of these dynamics.
By choosing specific values of Ω, given $\Delta = 0$, we achieved robust population inversion via ultrashort pulses between the first and the Nth level of an N-level system with SU(2) symmetry. This was done by employing the composite sequences derived by Torosov *et al.* [53]; particularly broadband (BB), narrowband (NB) and passband (PB) excitation schemes and by employing the well-known three-pulse NMR sequence [48]. Furthermore, our approach allows for precise control of the above processes in population inversion between palindromic states, namely between levels m and $N - m + 1$. These enable the controlled manipulation of the dynamics of excitation processes in multi-level materials, for the design of high fidelity infrastructure for quantum information.

2.2.2 Detuning Modulated Composite Pulses (DMCPs)

With the advent of quantum computers and high demand for accurate methods of quantum information processing (QIP), an immediate need for high-fidelity quantum state preparation and transfer emerged for any qubit architecture. This conveys a substantial challenge in practical realizations of QIP, where the admissible error of NIST-era quantum operations is smaller than 10^{-4} [33]. Such realizations for quantum computation hardware include trapped ions, atomic systems and transmon qubits. An additional promising candidate for advancing quantum technologies is integrated photonic circuits due to their scalability and on-chip integration capacity. The fidelity of operations in a photonic circuit remains below the QIP due to unavoidable fabrication errors. Even small systematic errors, i.e., due to imperfections in fabrication or in the experimental control knobs, reduce the fidelity of state transfer below the fault-tolerant threshold.

Plenty of scientific endeavours have been made to tackle the problem of accurate light transfer in photonic waveguide systems. These include methods of chirped adiabatic passage [67], and the previously-mentioned techniques STIRAP [68, 69], and a more recent application of adiabatic elimination to waveguide systems [70, 71]. Yet, all of these solutions rely on adiabatic, or very gradual, changes of one of the system parameters with respect to another. Thus, these solutions result in rather long propagation distances that are not scalable.

Our initial motivation for this work was to develop the first composite-pulses adaptation suitable for implementation in photonic waveguide systems. In the previous sections, I discussed composite pulses (CPs) as a powerful tool to correct for control and system errors in two- and multi-level systems with SU(2) symmetry. CPs have been applied in physical realizations of QIP including trapped ions and atomic systems [54, 72, 73]. However, CPs have not previously been used to correct for errors in photonic waveguide systems, as existing sequences require control of the *phase* of the coupling, which in integrated photonics is a real parameter. Our present research is the first to address this limitation and to derive CPs for any qubit architecture including integrated photonic systems.

In publication 3, featured in Chapter 3.3, we utilize off-resonant detunings as the control parameters to derive new families of CPs for high-fidelity unitary gate preparation within the quantum error threshold. The prerequisites of this derivation include the notion that the propagation of light in a coupled waveguide system is analogous to the time evolution of electron population in atomic levels. In Fig. 2.8, I highlight the main points of this analogy to the simplest configuration of two adjacent waveguides. When light is injected into an individual waveguide, it holds an uncoupled light propagating mode with an evanescent field tail that extends beyond the geometric boundaries of the waveguide. A second waveguide, placed in proximity to the first, is a perturbation to to this evanescent field. This is the origin of the coupling between the two waveguides, thus the light injected into

the first waveguide will eventually leak into its neighbor. The spatial exchange of the light will oscillate in a manner similar to Rabi oscillations in an atomic system. Mathematically, this is described by the coupled mode equations [39]:

$$\begin{array}{ll} \frac{d}{dz}E_1(z) & = i\beta_a E_1(z) + i\kappa_{12}E_2(z) \\ \frac{d}{dz}E_2(z) & = i\beta_b E_2(z) + i\kappa_{12}E_1(z) \end{array} \tag{2.19}$$

Here, $E_i(z)$ is the electromagnetic field amplitude in each waveguide and β_i is the respective complex propagation constant of the individual uncoupled mode (see Fig. 2.8). Using perturbation theory, the coupling is approximated by:

$$\kappa_{ij} = \frac{\omega}{2}\int\int[\epsilon(x,y) - \epsilon^{(j)}(x,y)]\overrightarrow{E}_{\perp}^{(i)}E_{\perp}^{(j)}dxdy \tag{2.20}$$

ω is the frequency of the electromagnetic field propagating in the system and $\epsilon(x,y)$ and $\epsilon^{(j)}(x,y)$ are the permittivity distributions of the coupled waveguide system and waveguide j. We can solve eq. 2.19 for its eigenmodes by assuming a solution of the form $E_i = A_i e^{i\beta z}$. The eigenmodes are a superposition of the symmetric and antisymmetric uncoupled waveguide modes, namely:

$$\begin{array}{ll} E_1(z) = & a_1(\Delta + \sqrt{\Delta^2+\kappa_{12}^2})e^{i\beta_+ z} + a_2(\Delta - \sqrt{\Delta^2+\kappa_{12}^2})e^{i\beta_- z} \\ E_2(z) = & a_1\kappa_{12}e^{i\beta_+ z} + a_2\kappa_{12}e^{i\beta_- z} \end{array} \tag{2.21}$$

where

$$\begin{array}{ll} \beta_\pm = & \frac{\beta_a+\beta_b}{2} \pm \sqrt{\Delta^2+\kappa_{12}^2} \\ \Delta = & \frac{\beta_a-\beta_b}{2} \end{array} \tag{2.22}$$

The couple mode equation is finally linearized to:

$$\begin{bmatrix} E_1(z) \\ E_2(z) \end{bmatrix} = \begin{bmatrix} cos(\Omega_g z) + i\frac{\Delta}{\Omega_g}sin(\Omega_g z) & i\frac{\kappa_{12}}{\Omega_g}sin(\Omega_g z) \\ i\frac{\kappa_{12}}{\Omega_g}sin(\Omega_g z) & cos(\Omega_g z) - i\frac{\Delta}{\Omega_g}sin(\Omega_g z) \end{bmatrix} \begin{bmatrix} E_1(0) \\ E_2(0) \end{bmatrix} e^{i\Omega z}. \tag{2.23}$$

where $\Omega_g = \sqrt{\Delta^2+\kappa_{12}^2}$ and $\kappa_{12} = \frac{\beta_a+\beta_b}{2}$. If we assume that $E_1(0) = 1$ and $E_2(0) = 0$, the light propagation in each waveguide spatially oscillates in intensity, as depicted in Fig. 2.9.

The aim of this research was to utilize the detuning as a control parameter and create a step-wise steering of light from one waveguide to another. By changing the relative widths of different segments of the coupled waveguides, we were able to achieve complete light transfer that is robust to errors in target segment lengths, widths and distances between the waveguides. It is important to note that while this work was initially developed with a photonic implementation in mind, we derived a **very general** and comprehensive theory that can be used on any qubit system and any multi-level system with SU(2) symmetry. Furthermore, Chapter 4.2 is a direct

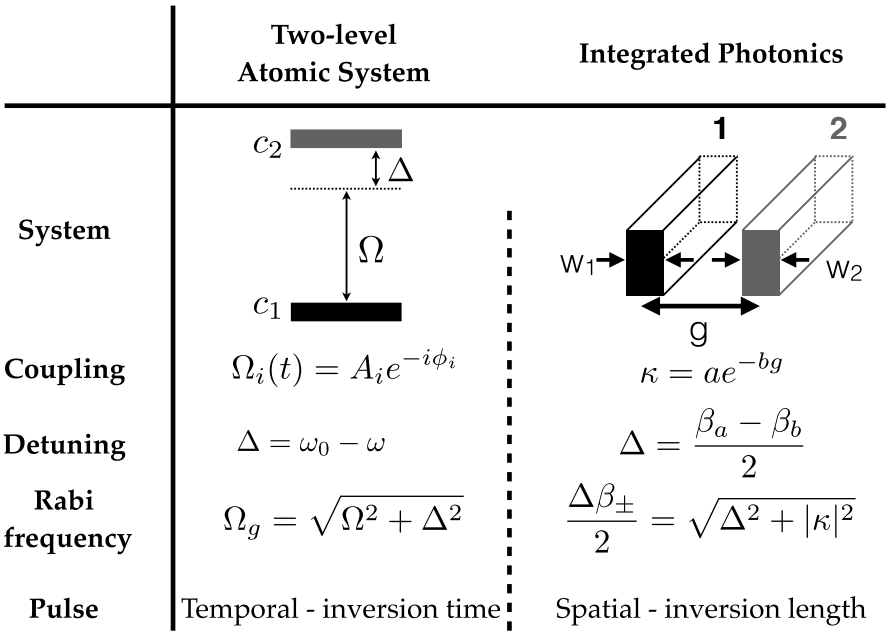

Fig. 2.8: Comparison between control parameters in a two-level atomic system and a two-waveguide integrated photonic circuit. The ground state in the integrated circuit is the light intensity injected to waveguide 1 (black). Due to the proximity between the two waveguides set at a distance g, the light intensity couples κ into waveguide 2, after a propagation distance (inversion length) that is a function of g. If both waveguides are identical in material and geometry, they are said to be "on-resonance", otherwise there is a real-valued detuning Δ which is set by the difference in the respective propagation constants of the waveguides β_i.

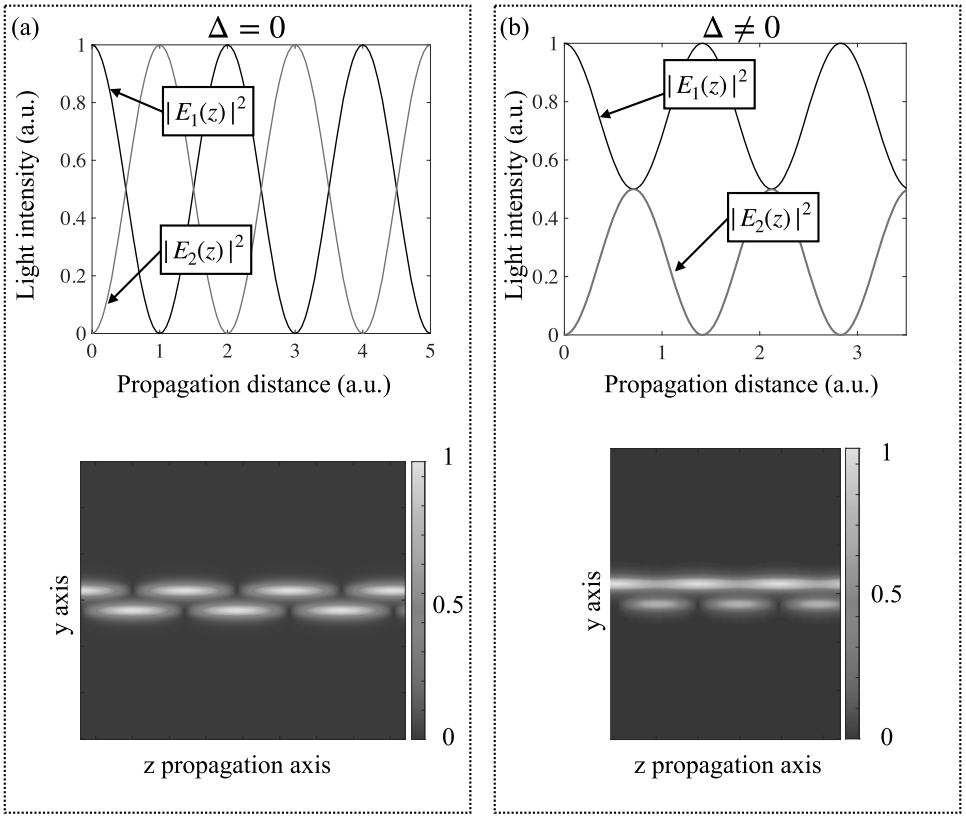

Fig. 2.9: Light intensity vs. propagation distance in coupled waveguide systems. (a) Simulated propagation of light in two identical *resonant* waveguides, with $\Delta = 0$. The light intensity spatially oscillates between the two adjacent waveguides, fully coupling from one to the other. (b) Simulated propagation of light in two *detuned* waveguides, with $\Delta \neq 0$. One waveguide is wider than its neighbor, resulting in *incomplete* light transfer.

(but not yet published) extension of this work to universal detuning-modulated composite pulses to create unitary gates suitable for QIP.

In what follows, we solve eq. 2.10, and assume $\Omega(t)$ and $\Delta(t)$ real and constant, which is well-suited for the foreseen implementation in coupled waveguides and in optical elements for generating higher harmonics. Regardless of this assumption, our pulses are also valid in systems with complex coupling parameters.

The unitary propagator of the time evolution governed by eq. 2.10 is found according to $U(t,0) = e^{-i/\hbar \int_0^t H(t)dt}$, which for constant Ω and Δ reads as eq. 2.11.

The propagator $U(\delta t)$ evolves the state of the qubit from the initial time t_0 to the final time t according to $\mathbf{c}(t) = U(\delta t)\mathbf{c}(t_0)$. If the initial state of the qubit at t_0 is $|1\rangle$, the population of the excited state $|2\rangle$ at time t is found by the modulus squared of the off-diagonal propagator element $|U_{12}(\delta t)|^2$.

Assuming a composite pulse sequence comprising N individual off-resonant pulses with Rabi frequencies Ω_n and detunings Δ_n, the propagator for the total composite pulse sequence is given by the product $U^{(N)}(T,0) = U_N(\delta t_N)\, U_{N-1}(\delta t_{N-1}) \ldots U_1(\delta t_1)$ where $\delta t_n = (t_n - t_{n-1})$ is the duration of the n^{th} pulse ($t_0 = 0$ and $t_N \equiv T$). We require that the composite sequence produces a complete qubit flip at the end of the evolution, such that the off-diagonal element of the total sequence fulfills $|U_{12}^{(N)}(T,0)|^2 = 1$.

For example, given a $N = 2$-piece composite pulse sequence with $\Delta_1/\Omega = a$ and $\Delta_2/\Omega = b$:

$$U^{(N=2)}(T,0) = \begin{pmatrix} cos\frac{A}{2} + i\frac{a}{\sqrt{1+a^2}} sin\frac{A}{2} & -i\frac{1}{\sqrt{1+a^2}} sin\frac{A}{2} \\ -i\frac{1}{\sqrt{1+a^2}} sin\frac{A}{2} & cos\frac{A}{2} - i\frac{a}{\sqrt{1+a^2}} sin\frac{A}{2} \end{pmatrix} \times \begin{pmatrix} cos\frac{A}{2} + i\frac{b}{\sqrt{1+b^2}} sin\frac{A}{2} & -i\frac{1}{\sqrt{1+b^2}} sin\frac{A}{2} \\ -i\frac{1}{\sqrt{1+b^2}} sin\frac{A}{2} & cos\frac{A}{2} - i\frac{b}{\sqrt{1+b^2}} sin\frac{A}{2} \end{pmatrix} \tag{2.24}$$

Plugging in $A = \pi$, this is:

$$U^{(N=2)}(T,0) = \begin{bmatrix} \frac{-1-ab}{\sqrt{1+a^2}\sqrt{1+b^2}} & \frac{a-b}{\sqrt{1+a^2}\sqrt{1+b^2}} \\ \frac{b-a}{\sqrt{1+a^2}\sqrt{1+b^2}} & \frac{-1-ab}{\sqrt{1+a^2}\sqrt{1+b^2}} \end{bmatrix} \tag{2.25}$$

Thus, comparing this total propagator to a $\alpha = \pi$ rotation around the $\hat{x}$ axis of the Bloch sphere:

$$R_x(\alpha) = \begin{bmatrix} cos\frac{\alpha}{2} & -isin\frac{\alpha}{2} \\ -isin\frac{\alpha}{2} & cos\frac{\alpha}{2} \end{bmatrix} \tag{2.26}$$

we find the detuning parameters necessary to achieve complete state transfer for a two-piece DMCP are $(a,b) = \pm(1,-1)$.

In order to derive a robust composite sequence that corrects for imperfections in the pulse area, we nullify the partial derivatives of the off-diagonal element of the total propagator $\frac{\partial^k}{\partial A^k}|U_{12}^{(N)}(T,0)|^2$, at $A = \pi$. This element is the state transition

probability $p = \frac{\Omega}{\Omega_g} sin^2(\frac{A}{2})$. We assume, for example, that the error lies solely in the pulse area $A = \pi(1 + \epsilon)$ that is decoupled from the coupling and the detuning parameters Ω and Δ. Thus, nullifying up to the k^{th} derivatives ensures that the error in the state transition probability is of the order of ϵ^{k+1}.

A *first-order* pulse is achieved by nullifying up to the fourth derivative ($k = 1, 2, 3$) and are robust to an error in the pulse area up to the order of $O(\epsilon^4)$. *Second-order* composite sequences, are achieved by nullifying up to the sixth derivative of the off-diagonal propagator element and are robust up to the order of an error in the pulse area of $O(\epsilon^6)$.

In contrast to previous works [53], the pulse area A for an off-resonant pulse is a function of all systematic parameters—pulse duration, amplitude, and detuning—thus, the detuning-modulated composite pulses presented here are *robust against various systematic errors by design*.

The results of this work are described and illustrated in publication 3, featured in Chapter 3.3. A thorough derivation of additional work on detuning-modulated composite pulses is available in Chapter 4.2 and in the Appendix. Specifically, in Chapter 4.2, I present my unpublished work (which is currently in review) on a comprehensive theory to derive detuning-modulated universal unitary gates, enabling robust state transfer from *any* initial state. In the Appendix, I lay out the technique to realize detuning-modualted composite pulses in quantum integrated photonic circuits.

Published Manuscripts

3

3.1 Paper 1: Multifrequency excitation and detection scheme in apertureless scattering near-field scanning optical microscopy

Optics Letters

Multifrequency excitation and detection scheme in apertureless scattering near-field scanning optical microscopy

H. Greener,[1,2] M. Mrejen,[1,2] U. Arieli,[1,2] and H. Suchowski[1,2,*]

[1]School of Physics and Astronomy, Tel Aviv University, Tel Aviv 69978, Israel
[2]Center for Light-Matter Interaction, Tel Aviv University, Tel Aviv 69978, Israel
*Corresponding author: haimsu@post.tau.ac.il

Received 20 June 2017; revised 16 July 2017; accepted 18 July 2017; posted 19 July 2017 (Doc. ID 298072); published 9 August 2017

Near-field scanning optical microscopy has revolutionized the study of fundamental physics, as it is one of very few label-free optical noninvasive nanoscale-resolved imaging techniques. However, its resolution remains strongly limited by the poor discrimination of weak near-field optical signals from a far-field background. Here, we theoretically and experimentally demonstrate a multifrequency excitation and detection scheme in apertureless near-field optical microscopy that exceeds current state-of-the-art sensitivity and background suppression. We achieved a twofold enhancement in sensitivity and deep subwavelength resolution in optical measurements. This method offers rich control over experimental degrees of freedom, breaking the ground for noninterferometric complete retrieval of the near-field signal. © 2017 Optical Society of America

OCIS codes: (180.4243) Near-field microscopy; (180.5810) Scanning microscopy; (240.6380) Spectroscopy, modulation.

https://doi.org/10.1364/OL.42.003157

In the past few decades, tremendous progress has been made in optical imaging beyond the diffraction limit [1–3]. Near-field microscopy has revolutionized this field, as it allows for noninvasive and nondestructive retrieval of deep subwavelength optical information, providing unprecedented information on optical properties of materials at the nanoscale [4–9]. Thus, the field has opened a window to phenomenon such as fundamental light-matter interactions, chemical reactions, and transport phenomenon in two-dimensional materials [10–18]. The apertureless version of the scattering near-field scanning optical microscope (sSNOM) has expanded to the optical regime from the topographic probing capabilities of the atomic force microscope (AFM). The sSNOM utilizes the AFM's sharp tip by dithering it in the proximity of a sample and illuminating it by focused light [19–21]. Owing to the nonlinearity of the light scattering process with respect to the tip-sample distance, high harmonic demodulation allows near-field imaging with a spatial resolution mainly limited by the apex of the tip [19,22]. However, to date, a thoroughly background-free image necessitates implementing various schemes, such as pseudoheterodyne detection, an interferometric technique in which a phase modulated reference enables the extraction of the pure near-field signal [23].

In this Letter, inspired by the recently introduced multifrequency AFM scheme resulting in subatomic topographic resolution [24–27], we introduce our newly formulated theoretical model, based on the bimodal excitation of the AFM cantilever as described in Fig. 1(a) and a multifrequency detection scheme in scattering SNOM (MF-SNOM). Our model

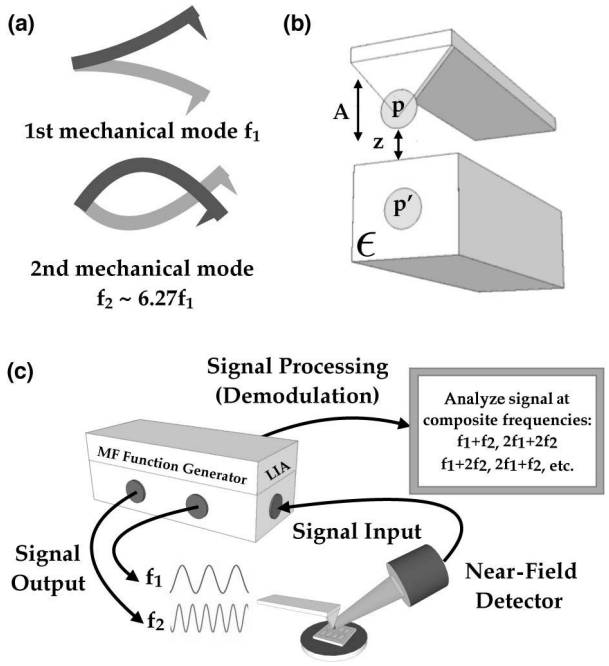

Fig. 1. (a) Simultaneous bimodal excitation of cantilever in multifrequency near-field scanning optical microscopy at two first flexural frequencies [28]. (b) Tip-sample system modeled as a polarized sphere of radius a, oscillating at amplitude A at small distances z from the sample of dielectric constant ε. (c) Scheme of experimental setup.

predicts a set of experimental parameters relevant for the suppression of optical background in the detected signal. We observe that in the multimodal excitation method, the set of possible experimental parameters spans over a two-dimensional plane, thus enabling further degrees of freedom in near-field measurements. We experimentally show that this scheme allows for further enhanced sensitivity in the measurement of a near-field signal as a function of tip-sample distance. From our current findings, we see that this enhanced sensitivity seems to lead to an improved resolution in the x–y plane. We believe that this is a feasible method that will allow for enhanced sensitivity, improved resolution, and background-free near-field images.

The theoretical basis of our model employs a quasi-electrostatic approach for the tip-sample system. The tip is modeled as a polarized sphere p of radius r, which is imaged in a sample of dielectric constant ϵ, set at a distance of z away from the tip, as shown in Fig. 1(b). Using the method of images, one can calculate an effective polarizability α_{eff}, and apply Mie scattering theory, to calculate the electromagnetic field scattering cross-section of the probe tip $C_{\text{scatt.}} = \frac{k^4}{6\pi}|\alpha_{\text{eff}}|^2$, assuming its radius is smaller than the illuminating wavelength (k is the wavenumber of the illuminating wave) [19]. This scattering cross-section, which is at the origin of the weak near-field signal of interest, is a nonlinear function of the distance between the probe and sample, by virtue of α_{eff}. Varying the tip-sample distance with time leads to a significant modulation of the above near-field scattering coefficient from the tip, while the scattered light from the cantilever body remains constant [29]. Therefore, by demodulating the detected scattered signal at the higher harmonic frequencies of the cantilever's motion, one could achieve a narrower cross-section, with a more abrupt change of signal, as the tip approaches the sample. This is equivalent to effectively sharpening the probe tip. Nevertheless, while this process results in higher near-field sensitivity to optical measurements, there is a trade-off, since the measured signal becomes significantly weaker at higher harmonic frequencies.

In our analysis, we employed a simplified scattering model [30] to express the bimodal near-field scattering amplitude as a function of the bimodal motion of the tip at its first two flexural frequencies, $f_1 = \omega/2\pi$ and $f_2 = \omega'/2\pi$, represented by $z(t) = A\cos(\omega t) + B\cos(\omega' t)$. The detected signal function is the sum of the near-field scattering amplitude $K[z(t)] = \exp\{-z(t)/d\}$, where d is the typical distance for which the near-field term decays, and a z motion artifact, due to optical interference (background) $W[z(t)] = \sin[\frac{4\pi z}{\lambda} + \frac{\pi}{4}]$. Thus, the detected signal function is a sum of the above:

$$S(t) = W(t) + bK(t), \tag{1}$$

where b is the scattering weight, dependent on the scaling of the scatterer volume, which in our case, is the spherical tip.

We expand the signal to the fourth order, assuming that the tip excitation amplitudes and the typical distance for near-field decay are much smaller than the illuminating wavelength. Separating the different frequency terms leads to a series of the different coefficients one could detect via a lock-in amplifier, such as

$$S(t) \approx \text{DC} + \frac{1}{2}\left[\frac{1}{\sqrt{2}}\left(\frac{4\pi}{\lambda}\right)^2 + \frac{b}{d^2}\right]AB\cos[(\omega+\omega')t] + \left[\frac{1}{\sqrt{2}}\left(\frac{1}{2}\frac{4\pi}{\lambda}\right)^4 + \frac{1}{32}\frac{b}{d^4}\right]A^2B^2\cos[(2\omega+2\omega')t]. \tag{2}$$

We define an optical contrast factor R_n as the ratio between the scattering term in each coefficient that goes as $1/d^n$ and the background artifact that goes as $1/\lambda^n$ of each n harmonic demodulated signal; the advantage in detecting the signal at certain frequencies in comparison to others becomes clear. An enhancement in R_n for higher orders of n leads to increased sensitivity to the near-field signal, compared to the optical background. From this point forth, we will refer to detection at a certain harmonic n as *demodulation*. Implementing the bimodal excitation method allows us to obtain the same values of this optical contrast factor by demodulation at lower harmonics of the sum of the bimodal frequencies. Namely, the optical contrast obtained via monomodal excitation and demodulation at $n = 2\omega$ is the same as that achieved via bimodal excitation and demodulation at $n' = \omega + \omega'$. A few values of these enhancement factors are shown in Table 1.

In particular, we find a clear advantage, leading to a 160-fold contrast enhancement, in demodulating the detected signal at the second harmonic of the sum of the two frequencies $2(\omega + \omega')$ for an illuminating wavelength of 1580 nm, compared to demodulation at $\omega + \omega'$. This is the same enhancement achieved in monomodal excitation while demodulating the detected signal at the fourth harmonic of the tip oscillation frequency, compared to demodulation at the second harmonic of this single frequency. Similarly, the same near-field detection enhancement is predicted to occur for bimodal excitation and demodulation at $2\omega + \omega'$ and for monomodal excitation and demodulation at 3ω. Thus, one could achieve a high optical contrast for lower demodulation frequencies, and obtain a stronger signal.

We generalized to the multifrequency regime the finding of Ref. [31] that the total intensity of the signal measured by the detector in a monomodal SNOM setup produces a nonvanishing background term at all n harmonics of the signal, directly proportional to $J_n(2ka_1)$. In this term, a_1 is the single tip oscillation amplitude, and k is the wavenumber of the illuminating field. To suppress the background, one must choose a_1 in a way that mathematically cancels this term. Bimodal excitation results in an extension of the available solutions for background suppression from a single tip oscillation amplitude to a two-dimensional plane of possible sets of the two oscillation amplitudes for each mode of excitation. This is derived from the new background term being proportional to the *product* of two Bessel functions, namely,

$$BKG_n = J_n(2ka_1) \times J_n(2ka_2). \tag{3}$$

Table 1. Calculated Values of the Optical Contrast Enhancement for Specified Illuminating Wavelengths

λ nm	$\frac{R_{2\omega}}{R_{\omega}}$	$\frac{R_{4\omega}}{R_{2\omega}} = \frac{R_{2(\omega+\omega')}}{R_{\omega+\omega'}}$
660	5.25	27.6
1200	9.5	91.7
1580	12.5	160

Thus, in this case, the solution space expands, and one can choose from a set of available tip oscillation amplitudes a_1 and a_2 to completely cancel this term, while demodulating the signal at the composite harmonics of the two mechanical frequencies of the tip.

To examine optical near-field measurements with the multifrequency SNOM technique, we used plasmonic nanostructure arrays, comprising Au nanobars and split ring resonators (SRRs). These were fabricated via standard electron beam lithography, and deposited with a height of 100 nm on an indium tin oxide substrate. The near-field measurements were done using a modified NeaSpec neaSNOM, illuminated with a tunable CW laser (Toptica CTL1550) between 1550 and 1580 nm, with 20 mW delivered to the tip. We used a Zurich Instruments UHF 600 MHz lock-in amplifier, with its many available oscillators, to externally drive the AFM cantilever on the one hand, and to demodulate the detected scattered signal at any frequency of our choice on the other hand. Figure 1(c) depicts a schematic representation of the experimental setup.

To compare the traditional monomodal SNOM technique with our bimodal method, we performed two different sets of measurements. First, the tip was made to mechanically vibrate monomodally at its first flexural frequency $f_1 = 70$ kHz, a characteristic value slightly different for each tip, at a free oscillation amplitude of $a_1 = 100$ nm, and the near-field optical signal was collected at this frequency and its higher harmonics. Next, the bimodal excitation method was employed; the tip was vibrated simultaneously at *two* of its first flexural frequencies, f_1 and $f_2 = 420$ kHz, at oscillation amplitudes of $\approx(a_1 = 100$ nm, $a_2 = 100$ nm), and the collected near-field optical signal was demodulated at multifrequency harmonics, theoretically predicted to display the same near-field-to-background contrast as their monomodal counterparts, such as $f_1 + f_2$, which is equivalent to $2f_1$. We note that in all our measurements, we used the same external lock-in amplifier, with the same detection parameters, such that the two measurements are comparable.

We initially measured the detected near-field signal of a single point of high signal intensity in each nanostructure as a function of the tip-sample distance to test the near-field sensitivity of this technique. Figure 2(a) is a comparison of these measurements, employing the standard monomodal method, demodulated at $4f_1$ versus the bimodal technique, demodulated at $2(f_1 + f_2)$. It is apparent that the bimodal method exhibits the desirable tip sharpening effect [19], as its narrower signal abruptly changes closer to the sample, with a faster rise of approach of $1/z^3$, compared to $1/z^2$, for the monomodal measurements. A further support for this claim is the twofold enhancement in the sensitivity of this measurement exhibited by the decrease in the FWHM. The FWHM marked in the bimodal measurement is 20 nm, roughly half of that extracted from the monomodal measurement, 37 nm. This implies that the signal detected via the monomodal method at $z = 35$ nm [blue curve in Fig. 2(b)], for example, contains an optical background that is absent from the signal detected via the bimodal method [red curve in Fig. 2(b)].

To examine whether the enhanced sensitivity translates into improved resolution, we performed a complete near-field scan of a 540 nm Au nanobar, illuminated with polarization along its long axis, employing both techniques, shown in Fig. 3. The inset of Fig. 3(a) is a near-field image obtained by monomodal excitation and signal demodulation at $4f_1$. The inset of

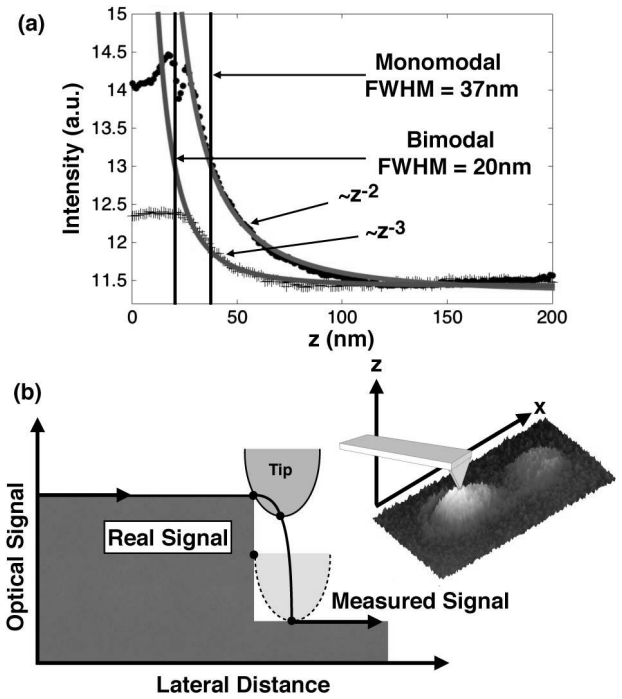

Fig. 2. (a) Measured (black) and fitted (blue and red) near-field sensitivity measurements. (b) Cartoon of optical signal obtained via a near-field scan; accuracy of measurement is proportional to effective tip size.

Fig. 3(b) is the same image obtained by bimodal excitation and signal demodulation at $2f_1 + 2f_2$. We note low intensity points, located at the left edge and the middle of the sample, that appear sharper in the image obtained by the bimodal excitation method. We quantified this by plotting the signal intensity, proportional to the near-field scattering, as a function of lateral distance, measured along the white-dotted line in each of the above images.

The low intensity points in each figure are depicted by dips in these line plots. While the FWHM of the left dip obtained in Fig. 3(a) is 10.4 nm, it is narrowed down to 6.7 nm in the bimodal measurement in Fig. 3(b). Moreover, the FWHM of the middle dip decreases by a factor of over 2 in the bimodal scheme, implying an increase in spatial resolution. This finding complies with the notion that the spatial resolution of SNOM measurements is directly proportional to the z axis sensitivity

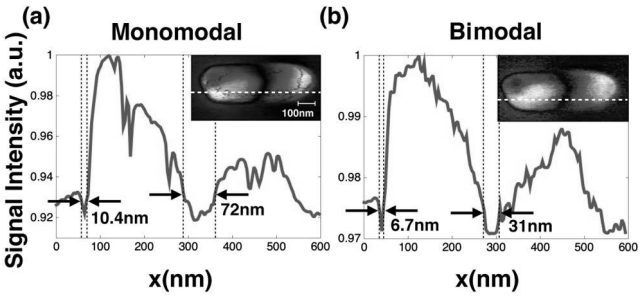

Fig. 3. Comparison of near-field optical image obtained by (a) monomodal excitation and detection on $4f_1$ and (b) bimodal excitation and detection on $2f_1 + 2f_2$. The line plots of the signal intensity versus lateral distance, measured along the white-dotted line in the inset images.

[32,33], as depicted in Fig. 2(b). Namely, a bulkier probe will at the same time be less depth sensitive and smear the lateral details as well as the optical signal, thus leading to a decrease in resolution. The increase in resolution is consistent, although not as prominent, for third-harmonic measurements, obtained via monomodal excitation and detection at $3f_1$ and via bimodal excitation and detection at $f_1 + 2f_2$ (not shown).

Furthermore, in the above comparisons, the monomodal excitation measurements exhibit so-called "z artifacts." These include parasitic low-intensity streaks in the inset of Fig. 3(a), originating from topographic features, that do not appear in the bimodal measurements, along with reduced topographic artifacts at the edge of the sample.

Figure 4(a) is a theoretical simulation of the tip oscillation amplitude values for complete background suppression, according to Eq. (3) calculated for the experimental variables of the images in Fig. 3, where $\lambda = 1550$ nm. The red line in Fig. 4(a) represents the single value of this amplitude in the monomodal case of $a_1 \approx 300$ nm. The blue range of values are the tip oscillation amplitude pairs (a_1, a_2) one could chose to suppress the background contribution to near-field measurements using the bimodal technique. We chose experimental values to maximize the near-field signal, while ensuring that this amplitude is at least a factor smaller than the illuminating wavelength, so that the theoretical model holds. Figure 4(b) is the same calculation, where the signal is demodulated at $3f_1$ in the monomodal case, and at $f_1 + 2f_2$ in the bimodal case. In Fig. 4(c) the signal is demodulated at $2f_1$ in the monomodal case and at $f_1 + f_2$ in the bimodal case. The range of available tip oscillation amplitudes expands as the bimodal demodulation frequencies rises, where the single oscillation amplitude, which depends on the illuminating wavelength, remains the same.

In conclusion, we have theoretically introduced a novel multifrequency excitation and demodulation technique to efficiently extract a near-field signal with improved sensitivity and deep subwavelength resolution reaching $\lambda/230$. Our experimental results demonstrate an enhanced tip-sharpening effect for bimodal excitation versus monomodal excitation leading to improved spatial resolution. This is a comprehensive and feasible experimental method due to its many degrees of freedom, resulting in background suppression and increased optical contrast with a high signal-to-noise ratio. The richness of the technique allows the conventional near-field scattering-type method to be expanded to detect weaker near-field signals at lower demodulation harmonics, thus enabling their thorough measurement. Our proof of concept breaks the ground for an unmatched capability of near-field optical detection, without compromising the subwavelength spatial resolution.

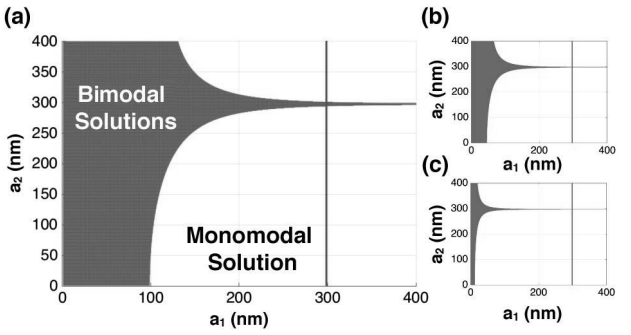

Fig. 4. Simulation of tip oscillation amplitude values for complete optical background suppression; comparison of monomodal versus multifrequency technique. See text for details.

Funding. Israel Science Foundation (ISF) (1433/15); PAZY Young Researcher Grant.

REFERENCES

1. L. Novotny and B. Hecht, *Principles of Nano-Optics*, 2nd ed. (Cambridge University, 2012).
2. A. Lewis, M. Isaacson, A. Harootunian, and A. Muray, Ultramicroscopy **13**, 227 (1984).
3. D. Pohl, W. Denk, and M. Lanz, Appl. Phys. Lett. **44**, 651 (1984).
4. E. Betzig, J. K. Trautman, T. D. Harris, J. S. Weiner, and R. L. Kostelak, Science **251**, 1468 (1991).
5. Y. Inouye and S. Kawata, Opt. Lett. **19**, 159 (1994).
6. F. Zenhausern, Y. Martin, and H. Wickramasinge, Science **269**, 1083 (1995).
7. B. Knoll and F. Keilmann, Nature **399**, 134 (1999).
8. L. Novotny, *Progress in Optics*, E. Wolf, ed. (Elsevier, 2007), Vol. **50**, p. 137, Chap. 5.
9. J. T. Robinson, S. F. Preble, and M. Lipson, Opt. Express **14**, 10588 (2006).
10. A. Y. Nikitin, E. Yoxall, M. Schnell, S. Vélez, I. Dolado, P. Alonso-Gonzalez, F. Casanova, L. E. Hueso, and R. Hillenbrand, ACS Photon. **3**, 924 (2016).
11. E. A. Muller, B. Pollard, and M. B. Raschke, J. Phys. Chem. Lett. **6**, 1275 (2015).
12. A. David, B. Gjonaj, and G. Bartal, Phys. Rev. B **93**, 121302 (2016).
13. Z. Fei, A. S. Rodin, W. Gannett, S. Dai, W. Regan, M. Wagner, M. K. Liu, A. S. McLeod, G. Dominguez, M. Thiemens, A. H. Castro Neto, F. Keilmann, A. Zettl, R. Hillenbrand, M. M. Fogler, and D. N. Basov, Nat. Nanotechnol. **8**, 821 (2013).
14. O. Khatib, J. D. Wood, A. S. McLeod, M. D. Goldflam, M. Wagner, G. L. Damhorst, J. C. Koepke, G. P. Doidge, A. Rangarajan, R. Bashir, E. Pop, J. W. Lyding, M. H. Thiemens, F. Keilmann, and D. N. Basov, ACS Nano **9**, 7968 (2015).
15. C.-Y. Wu, W. J. Wolf, Y. Levartovsky, H. A. Bechtel, M. C. Martin, F. D. Toste, and E. Gross, Nature **541**, 511 (2017).
16. D. N. Basov, M. M. Fogler, and F. J. Garca de Abajo, Science **354**, 1309 (2016).
17. K.-D. Park, O. Khatib, V. Kravtsov, G. Clark, X. Xu, and M. B. Raschke, Nano Lett. **16**, 2621 (2016).
18. F. Hu, Y. Luan, M. E. Scott, J. Yan, D. G. Mandrus, X. Xu, and Z. Fei, Nat. Photonics **11**, 356 (2017).
19. B. Knoll and F. Keilmann, Opt. Commun. **182**, 321 (2000).
20. R. Hillenbrand, B. Knoll, and F. Keilmann, J. Microsc. **202**, 77 (2000).
21. F. Keilmann and R. Hillenbrand, Philos. Trans. R. Soc. A **362**, 787 (2004).
22. D. P. Tsai, C. W. Yang, S.-Z. Lo, and H. E. Jackson, Appl. Phys. Lett. **75**, 1039 (1999).
23. N. Ocelic, A. Huber, and R. Hillenbrand, Appl. Phys. Lett. **89**, 101124 (2006).
24. J. R. Lozano and R. Garcia, Phys. Rev. Lett. **100**, 076102 (2008).
25. R. Garcia, *Amplitude Modulation Atomic Force Microscopy* (Wiley-VCH, 2010).
26. D. Garcia-Sanchez, A. San Paulo, M. J. Esplandiu, F. Perez-Murano, L. Forró, A. Aguasca, and A. Bachtold, Phys. Rev. Lett. **99**, 085501 (2007).
27. R. Hillenbrand, M. Stark, and R. Guckenberger, Appl. Phys. Lett. **76**, 3478 (2000).
28. R. W. Stark and W. M. Heckl, Surf. Sci. **457**, 219 (2000).
29. E. Ash and G. Nichols, Nature **237**, 510 (1972).
30. M. Labardi, S. Patane, and M. Allegrini, Appl. Phys. Lett. **77**, 621 (2000).
31. P. G. Gucciardi, G. Bachelier, and M. Allegrini, J. Appl. Phys. **99**, 124309 (2006).
32. D. Keller, Surf. Sci. **253**, 353 (1991).
33. L. Martíez, M. Tello, M. Díaz, E. Román, R. Garcia, and Y. Huttel, Rev. Sci. Instrum. **82**, 023710 (2011).

132.66.11.211 {ts '2020-11-05 07:24:20'}

3.2 Paper 2: Composite Pulses in N-level systems with SU(2) symmetry and their geometrical representation on the Majorana sphere

The Journal of Chemical Physics

Composite pulses in N-level systems with SU(2) symmetry and their geometrical representation on the Majorana sphere

Cite as: J. Chem. Phys. **148**, 074101 (2018); https://doi.org/10.1063/1.5013672
Submitted: 14 November 2017 . Accepted: 08 January 2018 . Published Online: 15 February 2018

H. Greener, and H. Suchowski

COLLECTIONS

This paper was selected as Featured

View Online Export Citation CrossMark

ARTICLES YOU MAY BE INTERESTED IN

Path integrals with higher order actions: Application to realistic chemical systems
The Journal of Chemical Physics **148**, 074106 (2018); https://doi.org/10.1063/1.5000392

Perspective: Quantum Hamiltonians for optical interactions
The Journal of Chemical Physics **148**, 040901 (2018); https://doi.org/10.1063/1.5018399

Communication: The electronic entropy of charged defect formation and its impact on thermochemical redox cycles
The Journal of Chemical Physics **148**, 071101 (2018); https://doi.org/10.1063/1.5022176

Meet the Next Generation of Quantum Analyzers
And Join the Launch Event on November 17th

Register now
Zurich Instruments

© 2018 Author(s).

AIP Publishing

THE JOURNAL OF CHEMICAL PHYSICS **148**, 074101 (2018)

Composite pulses in N-level systems with SU(2) symmetry and their geometrical representation on the Majorana sphere

H. Greener[1,2] and H. Suchowski[1,2,a)]
[1]*School of Physics and Astronomy, Tel Aviv University, Tel Aviv 69978, Israel*
[2]*Center for Light-Matter Interaction, Tel Aviv University, Tel Aviv 69978, Israel*

(Received 14 November 2017; accepted 8 January 2018; published online 15 February 2018)

High fidelity and robustness in population inversion is very desirable for many quantum control applications. We expand composite pulse schemes developed for two-level dynamics and present an analytic solution for the coherent evolution of an N-level quantum system with SU(2) symmetry, for achieving high fidelity and robust population inversion. Our approach offers a platform for accurate steering of the population transfer in physical multi-level systems, which is crucial for fidelity in quantum computation and achieving fundamental excitations in nuclear magnetic resonances and atomic physics. We also introduce and discuss the geometrical trajectories of these dynamics on the Majorana sphere as an interpretation, allowing us to gain physical insight on the dynamics of many-body or high-dimensional quantum systems. *Published by AIP Publishing.* https://doi.org/10.1063/1.5013672

I. INTRODUCTION

Complete population transfer (CPT) from one quantum state to another has been the focus of extensive research these past few decades. This is generally achieved by shaping the duration and area of an electromagnetic pulse impinged on a system in order to excite it and by employing various techniques ensuring this excitation is robust to inaccuracies in the system parameters and the pulse shape itself. Such control is desired for obtaining high fidelity in quantum computation and quantum information processing,[1,2] coherent manipulation of population inversion in atomic and molecular quantum systems,[3–6] directional optical waveguides,[7] and spin control in nuclear magnetic resonances.[8]

A handful of solvable models have been suggested and widely used for the coherently induced dynamics of two-level quantum systems. These include Rabi oscillations, in which a constant external field oscillating near the resonance of a two-level system is applied to achieve population inversion[9] due to an exact odd number of so-called π pulses. This solution is very sensitive to experimental constraints, such as a mismatch between the frequency of the external field and the system's resonance, known as detuning. Thus, other time-dependent methods were derived, including the Landau-Zener, Rosen-Zener, and Allen-Eberly models,[3,10,11] which allow for an adiabatic solution for very robust population inversion of a two-level system. However, these examples require very long and precise manipulation of the system and excitation parameters, which are not always feasible under experimental consequences.

Another class of analytical coherent solutions are composite pulses, which overcome such experimental constraints, and relax the need for a perfect system and excitation mechanism. These are a sequence of pulses with specifically chosen phases, commonly used in nuclear magnetic resonance (NMR), and for broadband population inversion by ultrashort pulses.[12–19] Since NMR spectroscopy requires precise pulse excitation for spin population inversion, attention was turned to designing composite sequences to compensate for conventional single pulse imperfections.[18] These may be due to spatial inhomogeneity, resonance offset, and bandwidth. Thus the performance of composite pulses in guiding a system to a final state is feasible, accurate, and robust.

Among these pulse sequences are Levitt's widely used spin population inversion schemes for NMR excitation.[16] This composite pulse enables a two-level spin $j = \frac{1}{2}$ system to undergo accurate excitation, regardless of the pulse or system's imperfections, by steering the system step-wise through three pulses. This scheme has since opened a wide variety of different composite pulse sequences, which revolutionized the field of NMR and its applications. While Levitt's composite solution, which is comprised of pulses with rectangular temporal shape, is suitable for NMR experiments, it fails to maintain its efficient nature for pulses of ultrashort time scales. Thus a different composite pulse scheme was suggested more recently by Torosov *et al.*[20,21] for pulse envelopes of smooth temporal shape, such as Gaussian pulses. Using these solutions, one can accurately excite two-level optical systems by tailoring the phases of a composite ultrashort pulse sequence regardless of the exact ingredient pulse shapes.

Despite the success of the above schemes for two-level systems, studies of the multi-level case have remained sparse in the field of NMR,[18,22] atomic, and optical systems. Adiabatic elimination, Electromagnetically-Induced-Transparency, stimulated Raman adiabatic passage (STIRAP), and the Landau-Zener picture[23–28] are solutions which have been thoroughly studied to achieve the controlled evolution of a three-level system to a chosen final state. Another one of the known solutions for N-level coherent dynamics was

a)Electronic mail: haimsu@post.tau.ac.il

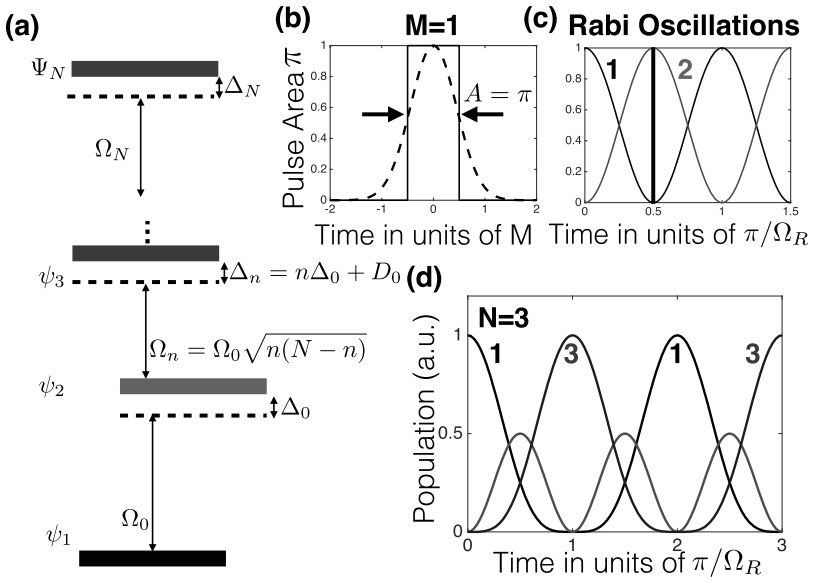

FIG. 1. Coupling scheme in atomic physics. (a) General N-level coupled system, with a ground ψ_1 and excited ψ_N level, coupling between adjacent levels Ω_n and detunings Δ_n. (b) Continuous line: A single ($M = 1$) pulse of rectangular temporal shape, defined as a π pulse. Dashed line: A single π pulse of Gaussian temporal shape. (c) The population evolution of a two-level system for the initial condition $\psi_1 = (1, 0)$ under a single π pulse. Population inversion is marked by a black dashed line at $t = j\pi/\Omega_R$, where for a two-level system, $j = 0.5$. (d) The population evolution of a three-level system for the initial condition $\psi_1 = (1, 0)$. Population inversion occurs at $t = j\pi/\Omega_R$, where for a three-level system $j = 1$.

suggested by Cook and Shore[29] as a generalization of the Rabi solution, and further developed by Hioe for other schemes of systems with SU(2) symmetry.[30] This symmetry dictates that the Hamiltonian of a ladder-connected N-level system lies entirely in the subspace spanned by the three generators of the SU(2) group. These are the angular momentum operators of spin $j = \frac{1}{2}(N-1)$, which comply to the commutation relation $[\hat{\sigma_i}, \hat{\sigma_j}] = i\hat{\sigma_k}$. Thus the Hamiltonian is written as

$$H(t) = c_1(t)\hat{\sigma_x} + c_2(t)\hat{\sigma_y} + c_3(t)\hat{\sigma_z} + c_0\hat{I}, \tag{1}$$

where $c_i(t)$ are arbitrary functions of time and $\hat{I}$ is the identity matrix.

In this case, one could still apply specific pulses which result in Rabi oscillations by considering specific time independent couplings and detuning parameters between adjacent levels, which do not have to be equidistant. Figure 1(a) depicts an example of a general N-level coupled system with SU(2) symmetry $\psi_1, \psi_2, \ldots, \psi_N$, which is dictated by a sequence of Rabi frequencies $\Omega_n = \Omega_0\sqrt{n(N-n)}$, where Ω_0 is the coupling between the first two levels which is a complex scaling factor, and the detunings $\Delta_n = n\Delta_0 + D_0$, where D_0 is an arbitrary real number.[29]

Yet, all of the above solutions require the fine-tuning of experimental parameters in order to achieve efficient population inversion between the ground state and the excited state; this problem can be solved by employing composite pulse sequences. In this work, we expand the composite pulses schemes developed for NMR and ultrashort temporal pulses to the general case of an N-level system with SU(2) symmetry.

In NMR, although a composite pulse scheme was derived for a very specific case of an anharmonic three-level system,[22] the lack of available solutions for multi-level systems has been mentioned.[18] It is in this setting that we introduce a generalization of the NMR spin inversion scheme to a spin j system, displaying SU(2) symmetry. In such systems, this symmetry is characterized by equal spacings between each level. This is not the general case in atomic systems, which can portray SU(2) symmetry without equidistant level spacings; therefore, these schemes can be further applied to optical systems. Particularly, we show that we can achieve robust population inversion via ultrashort composite pulses between the first and the Nth level of an N-level system with SU(2) symmetry. This is achieved by employing the composite sequences derived by Torosov *et al.*,[20] particularly broadband (BB), narrowband (NB), and passband (PB) excitation schemes. Furthermore, our approach allows for precise control of the above processes in population inversion between palindromic states, namely between levels m and $N - m + 1$. These enable the controlled manipulation of the dynamics of excitation processes in multi-level materials, for the design of high fidelity infrastructure for quantum information.

Last, we show that the evolution of the solutions to the composite pulse schemes can be interpreted and visualized as trajectories on a Majorana sphere,[31,32] the only means available today to compactly visualize N-level dynamics with SU(2) symmetry on a unit sphere. This representation provides a useful tool to feasibly portray the temporal evolution of many-level dynamics. It will allow to gain insight on high-dimensional or many-body systems, such as quantum entanglement in multiqubit systems,[33,34] spinor boson gases,[35,36] and geometric phases in many-body systems.[37–39]

The paper is organized as follows. In Sec. II, we introduce pulse-induced coherent dynamics of a multi-level system and formulate NMR and ultrashort pulse sequences for N-level systems. In Sec. III, we employ the Majorana representation to geometrically depict these dynamics. Section IV provides a brief discussion and summary.

II. COMPOSITE PULSE SCHEMES FOR POPULATION INVERSION IN N-LEVEL SYSTEMS

We start by describing the coherent dynamics of an N-level system, shown in Fig. 1(a), by a time dependent Schrodinger equation, where the probability amplitude for the nth level is[3,29,40]

$$i\frac{d}{dt}\psi_n(t) = \sum_{n'=1}^{N} H_{nn'}(t)\psi_{n'}(t). \tag{2}$$

In the case where N = 2, the Hamiltonian in the rotating-wave-approximation (RWA), in which the applied field intensity is low and near resonance, is

$$H = \frac{\hbar}{2}\begin{pmatrix} 0 & \Omega(t)e^{-iD(t)} \\ \Omega^*(t)e^{iD(t)} & 0 \end{pmatrix}, \tag{3}$$

where $\Omega(t)$ is the Rabi frequency for electric dipole transitions and the detuning between the laser carrier frequency and the energy gap in a two-level system is described by $D(t) = \int_{t_i}^{t} \Delta(t')dt'$, $\Delta = \omega_0 - \omega$, in which ω denotes the laser carrier frequency and $\omega_0 = (E_2 - E_1)/\hbar$ is the Bohr transition frequency between the two levels.

The propagator describing the SU(2) dynamics of the two-level system is $\hat{U} = \int_{t_i}^{t} \exp[iH(t')t']dt'$, such that $\psi(t_f) = \hat{U}\psi(t_i)$. Thus, for the special case of resonant lossless excitation, i.e., $\Delta = 0$, one could define the area of a pulse as $A = \int_{t_0}^{t_f} \Omega(t')dt'$. A single rectangular shaped pulse of area $A = \pi$, shown as the continuous line in Fig. 1(b), will lead to the commonly-known Rabi oscillations between the two levels, as shown in Fig. 1(c). The propagator describing the evolution of the above system excited by a sequence of M pulses with areas A_{t_k} and phases ϕ_k is given by the product $U_M = U_{\phi_{t_f}}(A_{t_f}) \ldots U_{\phi_{t_i}}(A_{t_i})$ (see Appendix A).

We first show that the description of a propagator specifying M pulses can immediately be extended to an N-level system with SU(2) dynamics, described by the Hamiltonian given in Eq. (1), where $\hat{\sigma_i}$ are presented in their $N \times N$ form. In the case of interest where the RWA is applied and the couplings are non-vanishing only between adjacent levels, we can write $c_1(t) = Re\{\Omega(t)\}$, $c_2(t) = Im\{\Omega(t)\}$, $c_3(t) = \Delta(t)$ and $c_0(t) = 0$. Thus for a sequence of M pulses with a constant area A and phases ϕ_k, where $k = 1, \ldots, M$, the Rabi frequency for step k is $\Omega_k(t) = Ae^{-i\phi_k}$, and the system evolves into a final state as $\psi(t_f) = e^{iH_M t} \ldots e^{iH_1 t}\psi(t_0)$, where the Hamiltonian is described by the irreducible representation of an N-level system with SU(2) symmetry:

$$H_k(t) = Re\{\Omega_k(t)\}\hat{\sigma}_x + Im\{\Omega_k(t)\}\hat{\sigma}_y + \Delta(t). \tag{4}$$

We recall that in order to achieve population inversion in a two-level system, one must apply a so-called π pulse on the system. Namely, one must ensure that $\frac{\theta}{2} = \Omega_R t$ where $\theta = \pi$. In our generalization to the N-level case, by applying a single π pulse, the population will flow from level 1 to level N in a characteristic time we refer to as the "population inversion time" $\tau = \pi/\Omega_R$. Figure 1(d) is an example of such Rabi oscillations for an $N = 3$ level system. Note a twofold increase in the typical time for population inversion between the two and three level systems. This is consistent with the fact that the time for population inversion is proportional to the respective spin value j multiplied by the number of pulses M impinged on the system, $\tau = jM\pi/\Omega_R$, where in the simplest case, $M = 1$.

However, a single pulse does not account for imperfections of a quantum system due to spatial inhomogeneity or a resonance offset. Moreover, a temporally inaccurate single pulse will not suffice to excite such a system. Such problems were at the origin of the emergence of the composite pulse as a possible solution. In the following, we will present our explicit expansion of composite pulse sequences derived for spin inversion in NMR via radiofrequency pulses and sequences derived for ultrashort Gaussian temporal shaped pulses to the general case of N-level systems with SU(2) symmetry.

The field of nuclear magnetic resonance spectroscopy has traditionally been considered the first to popularize composite pulses. Spin echo pulse sequences that compensate for static field inhomogeniety were initially used to achieve spin population inversion via radiofrequency (rf) pulses. This scheme was further expanded and improved by Levitt *et al.*[16] to compensate for inhomogeneous single pulses and detuning effects of a spin $\frac{1}{2}$ system. Thus, three ingredient rf pulses of arbitrary inaccurate shape performed consecutively on a two-level spin $\frac{1}{2}$ system, result in a robust population inversion. This is known as the NMR spin population inversion composite scheme.

In order to generalize Levitt's[16] NMR spin $\frac{1}{2}$ population inversion composite pulse to a three-level spin $j = 1$ system, we choose

$$\begin{aligned} A_{\tau_1} &= \tfrac{\pi}{2} \qquad \phi_{\tau_1} = 0, \\ A_{\tau_2} &= \pi \qquad \phi_{\tau_2} = \tfrac{\pi}{2}, \\ A_{\tau_3} &= \tfrac{\pi}{2} \qquad \phi_{\tau_3} = 0. \end{aligned} \tag{5}$$

We find that by exciting the ground state of this system, the inversion is between the first and third states, and each pulse should be applied for a duration of $\tau_i = \pi/\Omega_R$, as seen in Fig. 2(a). The total population inversion time is $\tau = 3\pi/\Omega_R$, consistent with the notion that $\tau = Mj\pi/\Omega_R$, where M is the total number of ingredient pulses in the composite scheme.

Figures 2(b) and 2(c) are examples of complete population inversion in three-level spin $j = 1$ and five-level spin $j = 2$ systems, compensated by the above composite sequence for pulse area inaccuracies of $A = \pi + \delta$, where $\delta = \pi/30$. Over 99% fidelity is achieved in both cases. To compare for $\delta = \pi/10$, over 96% fidelity is measured at the expected time of complete population inversion. A few examples of transition probability profiles for full spin population inversion as a function of deviations from the pulse area in units of π are shown in Fig. 2(e) for two-level spin $j = \frac{1}{2}$ (black), three-level $j = 1$ (red), five-level $j = 2$ (blue), and nine-level $j = 4$ (green) systems.

Furthermore, by varying the initial conditions of the system, one could achieve robust spin inversion between any two palindromic states, namely between levels $m \leftrightarrow m' = N - m + 1$. To demonstrate this, we calculated the dynamics of a five-level spin $j = 2$ system exposed to the NMR spin inversion composite pulse, set at $\Psi(t = 0) = \Psi_2$. In Fig. 2(d), one sees that an efficient inversion occurs between the 2nd and 4th states, along a population inversion time of $\tau = 6\pi/\Omega_R$, equivalent to the coherence time of the same system set at the initial condition of $\Psi(0) = \Psi_1$, seen in Fig. 2(c).

While Levitt's composite scheme has made a huge impact in NMR, and consequentially in MRI, its nature is inadequate for the excitation of dynamics in other two-level systems. An example of these include optical systems, controlled by ultrashort pulses, which are more prone to inaccuracies in pulse

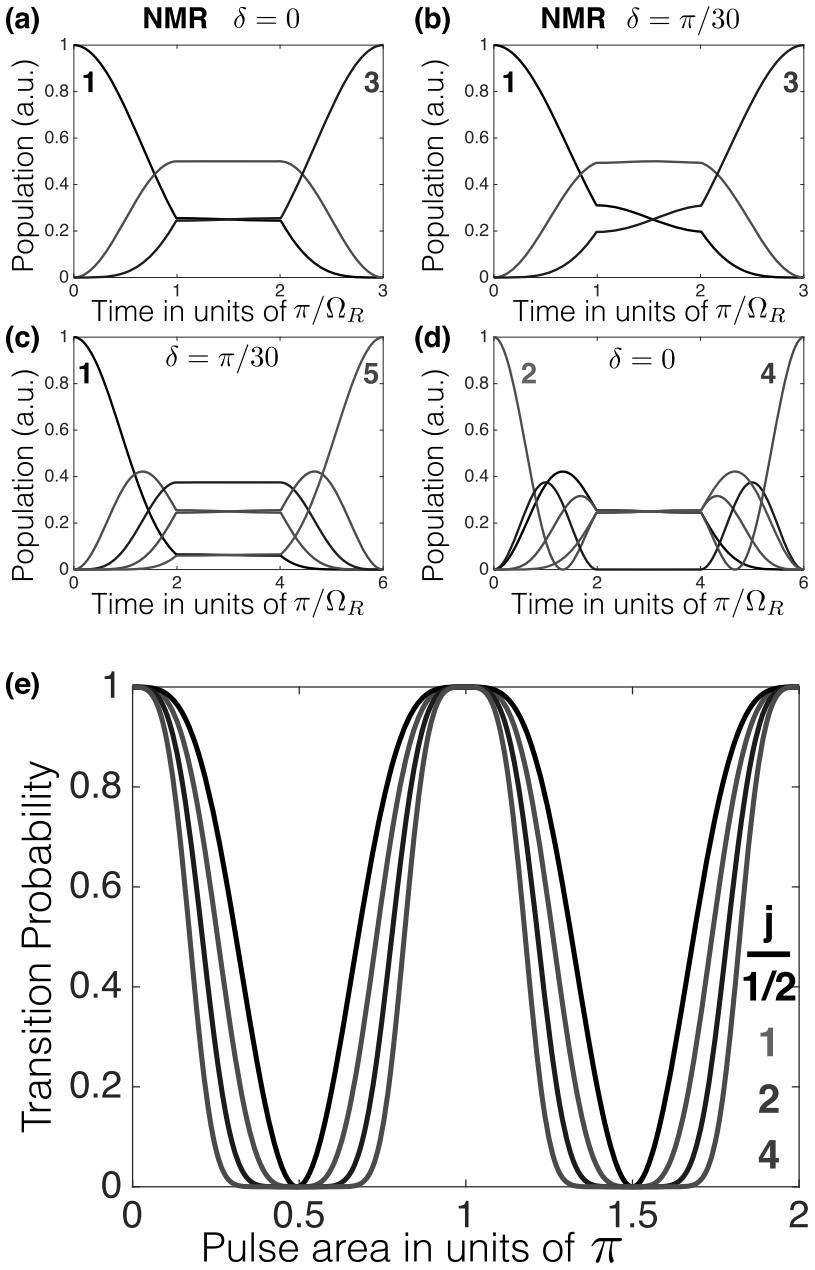

FIG. 2. NMR population inversion scheme in N-level systems. (a) Population inversion plot for three-level spin $j = \frac{1}{2}$ system excited by a completely accurate π pulse ($\delta = 0$). (b) Same system with $\delta = \pi/30$. (c) Population inversion plot for five-level spin $j = 2$ system with $\delta = \pi/30$. (d) Population inversion of palindromic levels. Here, $\Psi(0) = \Psi_2$ with $\delta = 0$. (e) Transition probability for full spin population inversion as a function of deviations from the pulse area δ in units of π for various spin j systems. Over 99% fidelity is achieved for pulse area inaccuracies of $A = \pi + \delta$, where $\delta = \pi/30$, in the case of a two-level and five-level system (see text for details).

area due to their smooth temporal shape. A comparison of a rectangular radiofrequency and a Gaussian ultrashort temporal pulse shape is shown in Fig. 1(b). The rectangular temporal shaped pulse can accurately be designed with a pulse area of π, while for the ultrashort Gaussian pulse, this conveys a challenge. For this reason, Torosov *et al.*[20,21] designed a series of composite pulse sequences to accurately achieve an arbitrarily flat inversion profile by tailoring the phases of the ingredient pulses. Thus, a broadband (BB) pulse scheme[20] for a two-level system is achieved by introducing such a composite sequence in which a flat top of the excitation profile is required at a pulse area of $A = \pi$. Alternatively, one could require a flat bottom of the excitation profile at pulse area $A = 0$ in order to achieve narrowband (NB) pulses,[20] or both a flat top at $A = \pi$ *and* a flat bottom at $A = 0$ to achieve a passband (PB) pulse.[20]

We now expand the composite pulse sequences for smooth temporal pulse shapes[20] to N-level systems with SU(2) symmetry, and achieve complete population inversion between levels 1 and N excited by an ill-defined ultrashort π pulse [see Fig. 1(b)]. We find that the number of pulses M dictates the achieved fidelity of the excited state. This can be shown in Fig. 3(a) in which a three-level system is excited with a single π pulse with an inaccuracy of $\delta = 0.3\pi$. Figure 3(b) shows the same system, excited by $M = 5$ composite pulses for broadband inversion. The system is fully steered to the excited state by a population inversion time of $\tau = 5\pi/\Omega_R$. This pulse sequence also proves useful for higher order systems, such as the five-level system shown in Figs. 3(c) and 3(d). This time, a longer composite pulse sequence is necessary in order to achieve complete population inversion.

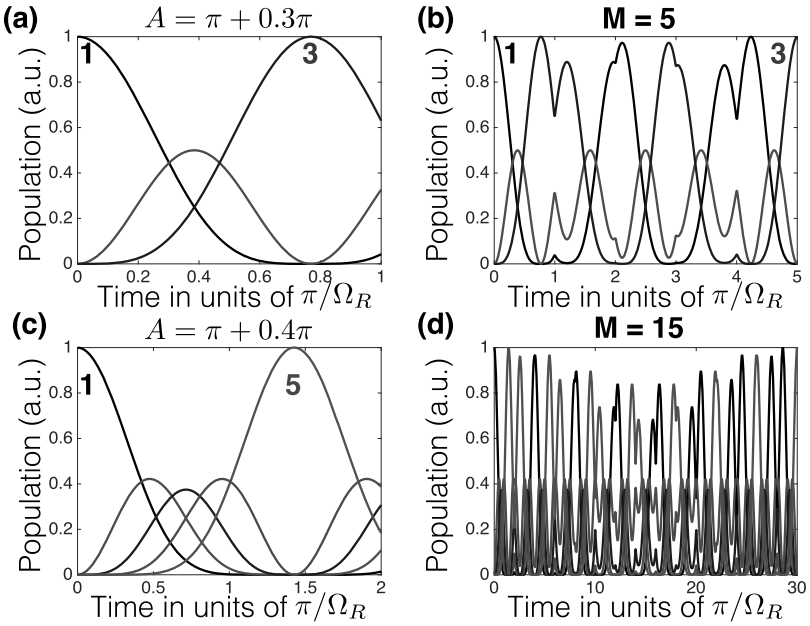

FIG. 3. Broadband (BB) population inversion scheme in N-level systems. (a) Three-level system exposed to single pulse of inaccurate area $A = \pi + 0.3\pi$. (b) Same system exposed to $M = 5$ BB composite pulses results in full population inversion from state 1 to state 3. (c) Five-level system exposed to single pulse of inaccurate area $A = \pi + 0.4\pi$. (d) Same system exposed to $M = 15$ BB composite pulses results in full population inversion from state 1 to state 5.

In order to present the fidelity of population inversion in N-level systems, in Fig. 4, we calculated the transition probability to the desired excited level as a function of the different pulse areas in units of π. Figures 4(a) and 4(b) show the transition probabilities for a broadband composite pulse sequence[20] comprised of $M = 5$ and $M = 15$ pulses, respectively, for a two-level (in blue), three-level (red), five-level (yellow), and nine-level (purple) system. Note that the fidelity broadens for larger values of ingredient pulses M and for smaller values of levels N.

Figure 4(c) shows the transition probabilities for a narrowband composite pulse sequence[20] comprised of $M = 5$ pulses for several N-level systems. It is noticeable that in this case, the fidelity is narrower for larger values of N. In Fig. 4(d), we calculated the transition probabilities as a function of the pulse area for several N-level systems, given a passband excitation of $M = 7$ composite pulses.[20] Here, the fidelity of the passband excitation scheme narrows and sharpens for larger values of N. We refer the reader to Appendix B for a discussion on palindromic population inversion in this case, where we present examples of various N-level systems accurately steered from level m to level $m' = N - m + 1$.

This generalization of composite ultrashort pulses in the broad framework of expanding these pulse schemes for N-level systems with SU(2) symmetry is suitable for the coherent excitation of optical systems, in which the level spacing does not have to be equidistant. The ability to prepare quantum states with high fidelity will be very useful for quantum information processing, robust state preparation in cooling schemes, and efficient coherent manipulation of atomic and molecular quantum systems.

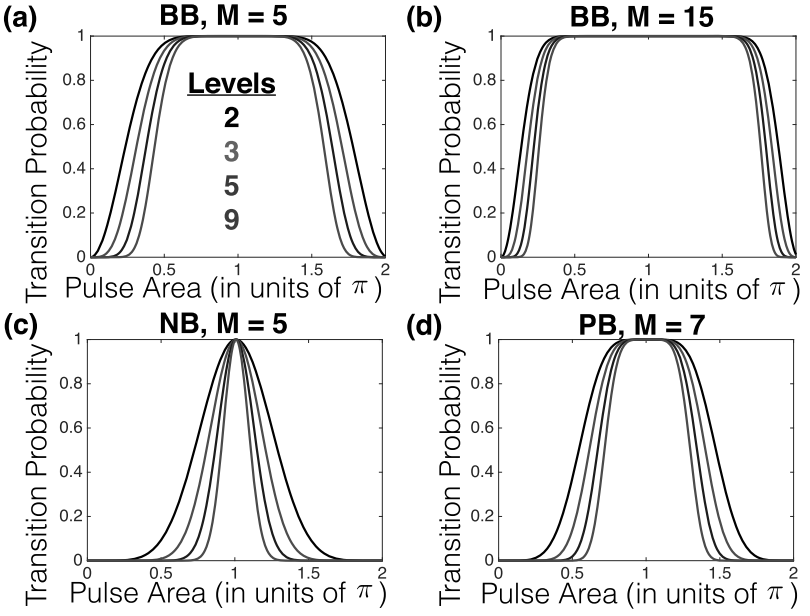

FIG. 4. Transition probabilities for composite pulse sequences in N-level systems. (a) Transition probabilities for $M = 5$ broadband (BB) composite sequences as a function of the area of the pulses for a two-level (black), three-level (red), five-level (blue), and nine-level (green) system. (b) Transition probabilities for $M = 15$ broadband composite sequences as a function of the area of the pulses for the same N-level systems as (a). (c) Transition probabilities for $M = 5$ narrowband (NB) composite sequences as a function of the area of the pulses for N-level systems. (d) Transition probabilities for $M = 7$ passband (PB) composite sequences as a function of the area of the pulses for N-level systems.

III. MAJORANA REPRESENTATION OF COMPOSITE PULSES IN N-LEVEL SYSTEMS WITH SU(2) SYMMETRY AS POINTS ON THE BLOCH SPHERE

The geometric interpretation of the dynamics in N-level systems is desirable in order to gain insight on these quantum states. The Majorana representation provides an elegant and compact means of portraying the evolution of an N-level system with SU(2) symmetry on a unit sphere. Here, we use this description to display the time evolution of an N-level system, as a Bloch sphere has traditionally been used to represent the dynamics of a two-level system.[1,41,42]

Without loss of generality, in the Bloch sphere representation, each spin $\frac{1}{2}$ equivalent state can be written as $|\psi\rangle = \cos\frac{\theta}{2}|\downarrow\rangle + e^{i\phi}\sin\frac{\theta}{2}|\uparrow\rangle$, where $\theta \in [0, \pi]$ and $\phi \in [0, 2\pi]$. It is easily seen that the basis vectors correspond to the North and South poles of a unit sphere. Thus, the Rabi oscillations presented as solid lines in Fig. 1(c) are conveniently described by a complete circular trajectory on a unit sphere. This geometric description was extended by E. Majorana[31,32] to describe higher order dynamics. In this representation, a spin S state is described by $2S$ points on a unit sphere, each representing spin $\frac{1}{2}$ particles, coupled, so their total spin equals S. We employ the Majorana representation to visualize the coherent dynamics of an N-level system, driven by the composite pulse schemes introduced in Sec. II, in the temporal domain. A comprehensive derivation is available in Appendix C, with an example of composite pulse dynamics of a three-level system in Appendix D.

Imposing the Hamiltonian given by Eq. (4) on the initial state $|1\rangle = (1, 0, 0)$ results in *two* Majorana points with trajectories similar to the single point on a Bloch sphere, representing the dynamics of a two-level system. In the three-level case, the two points begin on the North pole of the Majorana sphere and

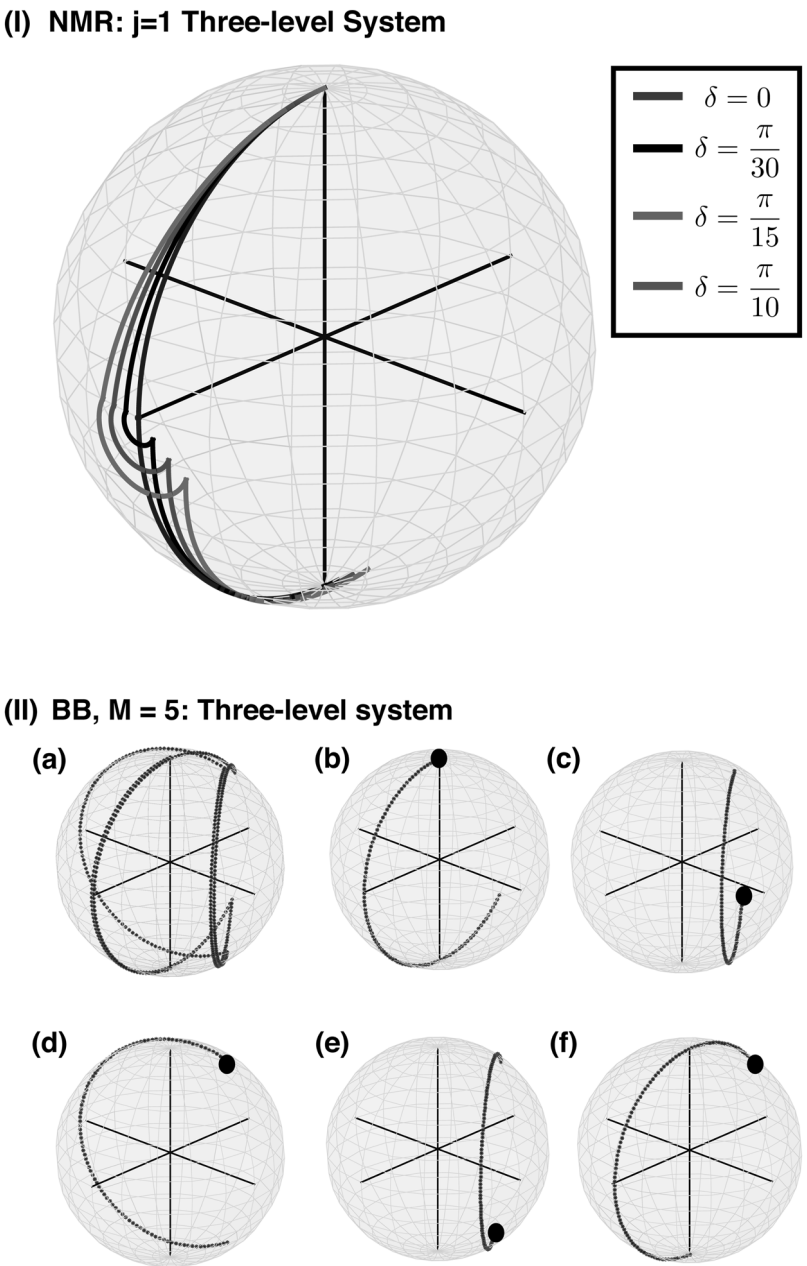

FIG. 5. Majorana representation of composite pulses in N-level systems. (I) Trajectories of two overlapping Majorana points of a three-level spin $j = 1$ system for various pulse area inaccuracies: $\delta = 0$ (blue), $\delta = \pi/30$ (black), $\delta = \pi/15$ (red), and $\delta = \pi/10$ (green). (II) (a) Broadband excitation of N = 3 level system by $M = 5$ composite pulses, where $\psi(t = 0) = |1\rangle$. The two Majorana overlapping points (blue and red) begin their trajectories on the North pole and evolve to the South pole according to the five trajectories shown in the following sub-figures. (b) Overlapping trajectories of the two Majorana points (MP) during the first of five composite pulses, beginning their motion at the North pole, indicated by a black dot in the figure. [(c)–(f)] Trajectories of the MPs during the second, third, fourth, and fifth of five composite pulses, respectively.

perform a full rotation around its $\hat{y}$ axis. For the initial state $|2\rangle = (0, 1, 0)$, the trajectories of both points are complimentary, namely, one point begins its trajectory on the North pole and the other on the South pole.

The Majorana representation of the NMR composite pulse sequence for a general spin j population inversion is shown in Fig. 5(I), for the case of a three-level spin $j = 1$ system, with the initial condition of $\Psi(t = 0) = |1\rangle$. This initial condition results in two overlapping Majorana points, which begin their trajectories at the North pole of the sphere. We show the time evolution of the different trajectories for the system, exposed to the NMR spin inversion pulse, for different pulse shape inaccuracies, from $\delta = 0$ to $\delta = \pi/10$, in the supplementary material. We also show how the initial condition of $\Psi(0) = \Psi_2$ results in two complementary trajectories of the two Majorana points.

The various ultrashort composite pulses sequences acting on a three level system also result in informative trajectories on the Majorana sphere, as seen in Fig. 5(II). A broadband composite sequence of $M = 5$ ingredient pulses, shown in Fig. 5(a) creates two overlapping Majorana points that quickly begin to move from their initial position on the North pole of the unit sphere, along a counter-clockwise direction. The different trajectories of the Majorana points for each of the 5 ingredient pulses are shown in Figs. 5(b)–5(f) (see supplementary material for the time evolution of these representations). Here, one sees how the three-level system is efficiently steered stepwise from its initial state at the North pole to its final state at the South pole of the Majorana sphere.

This visualization clearly shows the benefits of composite pulses in N-level systems with SU(2) symmetry. Trajectories that do not reach the South pole translate to states with lower fidelity. Composite pulse schemes enable complete population inversion, even between palindromic states, seen in the supplementary material.

IV. CONCLUSION

In conclusion, in this work we analytically expanded composite pulse schemes to N-level systems with SU(2) symmetry, allowing for accurate and robust customized population transfer. We generalized the commonly used NMR spin inversion scheme for the spin j case. This allows one to apply to an N-level system any composite scheme from the rich variety of sequences developed for radio frequency excitation of two-level systems. Additionally, we have shown that ultrashort composite pulses, and specifically the broadband, narrowband, and passband solutions[20] can be utilized in multi-level systems, described within the dynamics of the irreducible SU(2) model. Our method enables the coherent control of dynamics in physical multi-level systems, without imposing the approximation to a two-level solution. We have also shown a geometric representation of the composite pulse evolution of SU(2) symmetric N-level systems on the Majorana sphere. This description is advantageous, as it provides a feasible, intuitive means to grasp complex dynamics in multi-dimensional Hilbert space. We believe that this expansion of composite pulse schemes, along with such intuitive visualization, will lead to new findings and possibly new solutions for coherent control of complicated higher order systems.

SUPPLEMENTARY MATERIAL

See supplementary material for three movies of the Majorana representation of composite pulses in three-level systems: (1) NMR composite pulse for spin inversion of a $j = 1$ three-level system for different values of pulse inaccuracy Δ. (2) NMR composite pulse for spin inversion of the same system, with the initial condition $\psi(t = 0) = \psi_2$, where the pulse inaccuracy is $\Delta = \pi/15$. (3) Three-level system population inversion via five broadband composite pulses, in which the pulse inaccuracy value is $\Delta = 0.3\pi$.

ACKNOWLEDGMENTS

This work was financially supported by ERC-StG grant MIRAGE 20-15, Israel Science foundation Grant No. 1433/15, and a PAZY Young Investigator grant.

APPENDIX A: COHERENT DYNAMICS OF N-LEVEL SYSTEMS

The propagator describing the evolution of a two-level system can be simplified and parametrized in terms of complex Cayley-Klein parameters[30] with a constant phase shift in the Rabi frequency,

$$U_\phi(A_t) = \begin{pmatrix} a & be^{-i\phi} \\ -b^* e^{i\phi} & a^* \end{pmatrix}, \tag{A1}$$

where in the case of time-independent coupling,

$$\begin{aligned} a &= \cos\left(\frac{1}{2}\Omega_R t\right) - i\frac{\Delta}{\Omega_R}\sin\left(\tfrac{1}{2}\Omega_R t\right) \\ b &= i\frac{\Omega_0}{\Omega_R}\sin\left(\frac{1}{2}\Omega_R t\right) \end{aligned} \tag{A2}$$

and

$$\begin{aligned} \Omega_R &= \sqrt{\Delta^2 + |\Omega_0|^2} \\ \Omega_0 &= Ae^{-i\phi}. \end{aligned} \tag{A3}$$

In the case of an exact resonance ($\Delta = 0$), the Cayley-Klein parameters depend only on the pulse area $\hat{U} = \hat{U}(A)$.

Now, we can expand this to the SU(2) symmetric N-level case. Since $\hat{H(t)}$ is given by Eq. (4), for different values of t, the vectors representing the N states of an N-level system are transformed among themselves by the transformations of the SU(2) group. This means that if one finds the set of parameters $a(t)$, $b(t)$ for the two-level case, an immediate solution to the Schrodinger Eq. (2) is found from the $N = 2j + 1$ representation of the unitary group $D^j[a(t), b(t)]$,

$$\psi_m^{(j)}(t) = \sum_{m'=-j}^{j} D_{mm'}^{(j)}\left[a(t), b(t)\right] C_{m'}^{(j)}(0), \tag{A4}$$

where $m = -j, -j + 1, \ldots, j$, and the matrix elements are given as[30,43]

$$\begin{aligned} D_{mm'}^{(j)} = \sum_{\mu} &\frac{\sqrt{(j-m)!\,(j+m)!\,(j-m')!\,(j+m')!}}{p!q!r!s!} \\ &\times a^p a^{*q} b^r \left(-b^*\right)^s. \end{aligned} \tag{A5}$$

Here, $p = j - m - \mu$, $q = j + m' - \mu$, $r = \mu$, and $s = m - m' + \mu$ and $C^{(j)}_{m'}(0)$ is the initial condition vector of the system.

Thus, in our notation, a spin j system is interchangeable with an N-level system of this representation, with SU(2) symmetry. For example, for a $j = 1$ three-level system, the matrix is

$$D^{(j=1)}(a,b) = \begin{pmatrix} a^2 & \sqrt{2}ab & b^2 \\ -\sqrt{2}ab^* & |a|^2 - |b|^2 & \sqrt{2}a^*b \\ -b^{*2} & -\sqrt{2}a^*b^* & a^{*2} \end{pmatrix}. \quad \text{(A6)}$$

It is important to stress that there are a number of solutions for the coherent dynamics of such systems with non-equidistant level spacings.[29]

APPENDIX B: PALINDROMIC POPULATION INVERSION IN N-LEVEL SYSTEMS VIA BROADBAND ULTRASHORT COMPOSITE PULSES

Taking advantage of the unique property of palindromic excitation of N-level systems with SU(2) symmetry, we calculated the evolution of several such systems exposed to a broadband composite pulse scheme[20] with different initial conditions. Figure 6(a) shows a three-level system excited by $M = 5$ ingredient pulses, with the initial condition of $\psi(0) = \psi_2$. The system remains in this state, as it is its own palindromic counterpart. Figure 6(b) is a five-level system excited by the same broadband composite pulse sequence, with the initial condition of $\psi(0) = \psi_2$. This time, the system evolves into the final state ψ_4. Figures 6(c) and 6(d) present the evolution of a nine-level system excited by a broadband composite sequence of $M = 15$ pulses, with the initial conditions ψ_2 and ψ_3, which evolve into the final states ψ_8 and ψ_7 respectively.

APPENDIX C: THE MAJORANA REPRESENTATION

The basis for the spin states of a spin-S particle is given as

$$|S, M\rangle,\ M = -S, \ldots, +S,$$

thus an arbitrary pure spin state can be written as $|\xi\rangle = \sum_{M=-S}^{S} \xi_M |S, M\rangle$, where ξ_M is a complex number for each M. We define the spin S state as a symmetrized tensor product of spin $\frac{1}{2}$ states, $|\tilde{\xi}\rangle = \frac{A}{(2S)!} \sum_P \otimes_{k=1}^{2S} \phi_k$, with components given by $\phi_k = \alpha_k |\uparrow\rangle_k^M + \beta_k |\downarrow\rangle_k^M$, where $k = 1, ..., 2S$, and where P are the permutations of the signs $\uparrow$ and $\downarrow$.

To obtain the spin $\frac{1}{2}$ vectors, if $|\tilde{\xi}\rangle$ is known, one must define the Majorana polynomial[31]

$$P_{Majo}\left(|\tilde{\xi}\rangle; x\right) = \sum_{M=-S}^{S} \binom{2S}{S+M}^{1/2} \tilde{\xi}_M x^{S+M}. \quad \text{(C1)}$$

Here, we denote a spin S system by $2S$ decimal numbers, such that

$$|i\rangle_d = \sum_{j=0}^{2S} |S, j - S\rangle, \quad \text{(C2)}$$

where $i = 0, 1, 2, \ldots, 2S$. Given a state vector of a spin S system $\phi = \sum_{i=0}^{2S} C_i |i\rangle_d$, where C_i is the weight of each of the $2S$ states $|i\rangle_d$, the corresponding Majorana polynomial becomes

$$P_{Majo}(\phi; x) = \sum_{i=0}^{2S} \binom{2S}{i}^{1/2} C_i x^i. \quad \text{(C3)}$$

Using the roots of the Majorana polynomial, every spin S state can be mapped as $2S$ points on the Bloch sphere,[33] namely,

$$x_k = \tan\frac{\theta_k}{2} e^{i\phi_k}, \quad \text{(C4)}$$

where θ_k, ϕ_k are the angular coordinates on a sphere. In Eq. (C4), one can see that $x_k = -\beta_k/\alpha_k$, thus $\alpha_k = 0$ corresponds to $\theta_k = \pi$.

It can be shown[33] that if the Majorana polynomial defined as in Eq. (C1) is a rotation of the spin vector $|\xi\rangle$ by a spin rotation matrix $D^{(S)}(\alpha, \beta, \gamma)$, this corresponds to rotating the point configuration of $|\xi\rangle$ by $R(\alpha, \beta, \gamma) \in SO(3)$, parametrized by the Euler angles.

Therefore, applying the Hamiltonian given by Eq. (4) on an N-level system acts as a rotation of all the Majorana points on the sphere. Thus, the trajectory of these points is

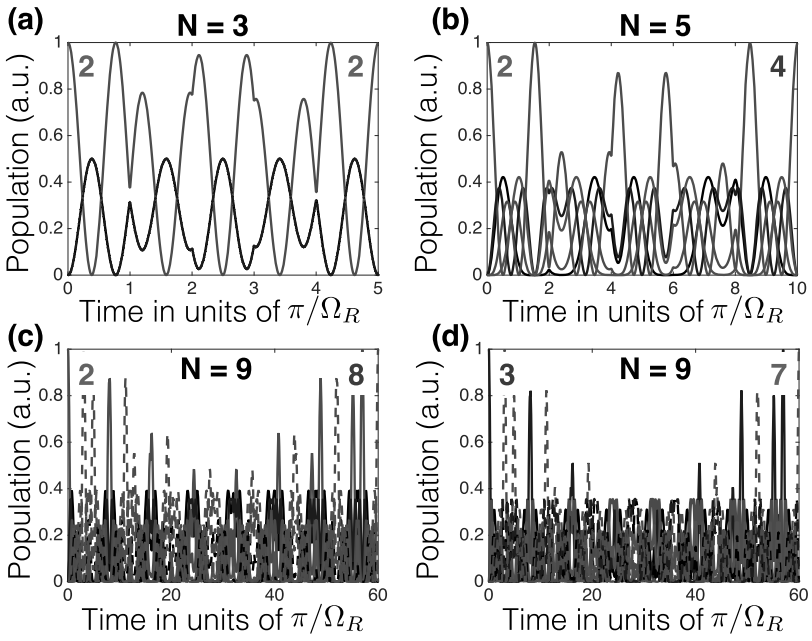

FIG. 6. Palindromic population inversion in N-level systems via broadband composite pulses. (a) Population evolution of a three-level system with the initial condition $\psi(0) = \psi_2$ excited by $M = 5$ broadband composite pulses. (b) Five-level system excited by $M = 5$ broadband composite pulses, with the initial condition $\psi(0) = \psi_2$. (c) Nine-level system excited by $M = 15$ broadband composite pulses, with the initial condition $\psi(0) = \psi_2$. (d) Same system and excitation as (c), with the initial condition $\psi(0) = \psi_3$.

interpreted as the temporal evolution of the multi-level system dynamics.

APPENDIX D: EXAMPLE OF MAJORANA REPRESENTATION FOR COMPOSITE PULSE DYNAMICS IN A THREE-LEVEL SYSTEM

In the following we will demonstrate this visualization procedure for composite pulse dynamics in a three-level system. Consider a three level spin 1 system composed of three states: $|1\rangle \equiv |1, -1\rangle \equiv (1, 0, 0)$, $|2\rangle \equiv |1, 0\rangle \equiv (0, 1, 0)$ and $|3\rangle \equiv |1, 1\rangle \equiv (0, 0, 1)$, with dynamics described by the Hamiltonian given by Eq. (4). This time,

$$\hat{H} = \frac{\pi}{\sqrt{2}} \begin{pmatrix} 0 & 1 & 0 \\ 1 & 0 & 1 \\ 0 & 1 & 0 \end{pmatrix}. \tag{D1}$$

The eigenvalues and eigenvectors of this Hamiltonian $AV = V D$ are

$$D = \pi \begin{pmatrix} -1 & 0 & 0 \\ 0 & 0 & 0 \\ 0 & 0 & 1 \end{pmatrix} \quad V = \frac{1}{2} \begin{pmatrix} 1 & -\sqrt{2} & 1 \\ -\sqrt{2} & 0 & \sqrt{2} \\ 1 & \sqrt{2} & 1 \end{pmatrix}.$$

We use the Majorana representation to describe these eigenvectors in terms of those of a two level system, completely represented by the basis of two eigenstates $|\uparrow\rangle$ and $|\downarrow\rangle$. One could define the symmetric (S) and antisymmetic (A) states for each spin 1/2,

$$\begin{aligned} |S\rangle_i &= \frac{|\uparrow\rangle_i + |\downarrow\rangle_i}{\sqrt{2}}, \\ |A\rangle_i &= \frac{|\uparrow\rangle_i - |\downarrow\rangle_i}{\sqrt{2}}, \end{aligned} \tag{D2}$$

where for a spin S system, $i = 1, \ldots, 2S$ and in the case where $S = 1$, $i = 1, 2$.

Recalling that the state vector of a two-level system on the Bloch sphere can be described by $|\psi\rangle = \cos\frac{\theta}{2}|\uparrow\rangle + e^{i\phi}\sin\frac{\theta}{2}|\downarrow\rangle$, we now extend this to the N-level case. By calculating the roots of the Majorana polynomial in Eq. (C3) for the different eigenvectors $\overrightarrow{V}$, we find the values of (θ_i, ϕ_i) for the $2S = 2$ points on the Majorana sphere, thus enabling a convenient representation of the spin 1 system in the basis of two spin 1/2 states,

$$\begin{aligned} \overrightarrow{v_\alpha} &= |S\rangle_1 + |S\rangle_2, \\ \overrightarrow{v_\beta} &= |S\rangle_1 + |A\rangle_2, \\ \overrightarrow{v_\gamma} &= |A\rangle_1 + |A\rangle_2. \end{aligned} \tag{D3}$$

Now, we can describe the different levels of a spin 1 system in terms of these eigenvectors,

$$\begin{aligned} |1\rangle &= \frac{1}{2}\left(\overrightarrow{v_\alpha} + \overrightarrow{v_\gamma} - \sqrt{2}\overrightarrow{v_\beta}\right), \\ |2\rangle &= \sqrt{2}\left(\overrightarrow{v_\gamma} - \overrightarrow{v_\alpha}\right), \\ |3\rangle &= \frac{1}{2}\left(\overrightarrow{v_\alpha} + \overrightarrow{v_\gamma} + \sqrt{2}\overrightarrow{v_\beta}\right). \end{aligned} \tag{D4}$$

[1] M. Nielsen and I. Chuange, *Quantum Computation and Quantum Information* (Cambridge University Press, Cambridge, 2000).
[2] A. Sørensen and K. Mølmer, Phys. Rev. Lett. **82**, 1971 (1999).
[3] L. Allen and J. Eberly, *Optical Resonance and Two Level Systems* (Dover, New York, 1975).
[4] J. Gong and S. A. Rice, Phys. Rev. A **69**, 063410 (2004).
[5] J. Gong and S. Rice, J. Chem. Phys. **120**, 9984 (2004).
[6] H. Suchowski, Y. Silberberg, and D. B. Uskov, Phys. Rev. A **84**, 013414 (2011).
[7] A. Yariv, IEEE J. Quantum Electron. **9**, 9 (1973).
[8] J. Keeler, *Understanding NMR* (John Wiley and Sons, New York, 2005).
[9] I. I. Rabi, J. R. Zacharias, S. Millman, and P. Kusch, Phys. Rev. **53**, 318 (1938).
[10] C. Zener, Proc. R. Soc. London, Ser. A **137**, 696 (1932).
[11] N. Rosen and C. Zener, Phys. Rev. **40**, 502 (1932).
[12] E. L. Hahn, Phys. Rev. **80**, 580 (1950).
[13] H. Y. Carr and E. M. Purcell, Phys. Rev. **94**, 630 (1954).
[14] H. M. Cho, R. Tycko, A. Pines, and J. Guckenheimer, Phys. Rev. Lett. **56**, 1905 (1986).
[15] H. K. Cummins, G. Llewellyn, and J. A. Jones, Phys. Rev. A **67**, 042308 (2003).
[16] M. H. Levitt and R. Freeman, J. Magn. Reson. **33**, 473 (1979).
[17] R. Freeman, S. P. Kempsell, and M. Levitt, J. Magn. Reson. **38**, 453 (1980).
[18] M. H. Levitt, Prog. Nucl. Magn. Reson. Spectrosc. **18**, 61 (1986).
[19] R. Tycko, Phys. Rev. Lett. **51**, 775 (1983).
[20] B. T. Torosov and N. V. Vitanov, Phys. Rev. A **83**, 053420 (2011).
[21] B. T. Torosov, E. S. Kyoseva, and N. V. Vitanov, Phys. Rev. A **92**, 033406 (2015).
[22] M. H. Levitt, D. Suter, and R. R. Ernst, J. Chem. Phys. **80**, 3064 (1984).
[23] J. R. Kuklinski, U. Gaubatz, F. T. Hioe, and K. Bergmann, Phys. Rev. A **40**, 6741 (1989).
[24] J. Oreg, F. T. Hioe, and J. H. Eberly, Phys. Rev. A **29**, 690 (1984).
[25] K. Bergmann, H. Theuer, and B. W. Shore, Rev. Mod. Phys. **70**, 1003 (1998).
[26] B. W. Shore, K. Bergmann, and J. Oreg, Z. Phys. D: At., Mol. Clusters **23**, 33 (1992).
[27] M. Fleischauer, A. Imamoglu, and J. Marangos, Rev. Mod. Phys. **77**, 633 (2005).
[28] N. V. Vitanov, A. A. Rangelov, B. W. Shore, and K. Bergmann, Rev. Mod. Phys. **89**, 015006 (2017).
[29] R. J. Cook and B. W. Shore, Phys. Rev. A **20**, 539 (1979).
[30] F. T. Hioe, J. Opt. Soc. Am. B **4**, 1327 (1987).
[31] E. Majorana, Nuovo Cimento **9**, 43 (1932).
[32] F. Bloch and I. I. Rabi, Rev. Mod. Phys. **17**, 237 (1945).
[33] H. Mäkelä and A. Messina, Phys. Rev. A **81**, 012326 (2010).
[34] H. D. Liu and L. B. Fu, Phys. Rev. A **94**, 022123 (2016).
[35] R. Barnett, D. Podolsky, and G. Refael, Phys. Rev. B **80**, 024420 (2009).
[36] B. Lian, T.-L. Ho, and H. Zhai, Phys. Rev. A **85**, 051606 (2012).
[37] P. Bruno, Phys. Rev. Lett. **108**, 240402 (2012).
[38] P. Ribeiro, J. Vidal, and R. Mosseri, Phys. Rev. Lett. **99**, 050402 (2007).
[39] P. Ribeiro, J. Vidal, and R. Mosseri, Phys. Rev. E **78**, 021106 (2008).
[40] B. Shore, *The Theory of Coherent Atomic Excitation* (Wiley, New York, 1990), Vol. I.
[41] M. Born and E. Wolf, *Principles of Optics* (Cambridge University Press, Cambridge, 1999).
[42] F. Bloch, Phys. Rev. **70**, 460 (1946).
[43] M. Hamermesh, *Group Theory and Its Application to Physical Problems* (Addison-Wesley, Reading, Mass, 1962), p. 354.

3.3 Paper 3: Detuning-modulated composite pulses for high-fidelity robust quantum control

Detuning-modulated composite pulses for high-fidelity robust quantum control

Elica Kyoseva,[1,2,3,*] Hadar Greener,[2,3] and Haim Suchowski[2,3]
[1]*Institute of Solid State Physics, Bulgarian Academy of Sciences, 72 Tsarigradsko Chaussee, 1784 Sofia, Bulgaria*
[2]*Condensed Matter Physics Department, School of Physics and Astronomy, Tel Aviv University, Tel Aviv 69978, Israel*
[3]*Center for Light-Matter Interaction, Tel Aviv University, Tel Aviv 69978, Israel*

(Received 10 September 2018; revised manuscript received 1 August 2019; published 25 September 2019)

We introduce a control method for off-resonant robust quantum information processing suited for quantum integrated photonics. We utilize detunings as control parameters to derive a family of composite pulses for high-fidelity complete population transfer. The presented detuning-modulated composite sequences can be implemented within the decay lifetime of the qubit and correct for control inaccuracies in various parameters including pulse strength, duration, detuning, phase jitter, Stark shift, and unwanted frequency chirps. We implement the proposed robust sequences in an integrated photonics platform to achieve complete light transfer insensitive to fabrication errors.

DOI: 10.1103/PhysRevA.100.032333

I. INTRODUCTION

Quantum information processing (QIP) relies on high-fidelity quantum state preparation and transfer. This presents a challenge in practical realizations of QIP where the admissible error of quantum operations is smaller than 10^{-4} [1]. Thus small systematic errors due to imperfections in fabrication or in the experimental control knobs reduce the fidelity of state transfer below the fault-tolerant threshold. A powerful tool to correct for systematic errors is composite pulses (CPs), which were initially developed in the field of nuclear magnetic resonance [2–9]. A composite pulse is a sequence of pulses with different areas and/or phases that implement accurate and robust quantum gates. To this end, CPs are designed for resonant or adiabatic interactions with complex coupling parameters [10–12] and were successfully used to achieve complete population transfer (CPT) in quantum systems in both rf and ultrashort pulses [13].

More recently, CPs found applications in matching higher harmonic generation processes [14] and in designing polarization rotators [15,16], as well as in QIP realizations including trapped ions [17] and atomic systems [18,19]. Another promising candidate for advancing QIP technologies is integrated photonic circuits due to their scalability and on-chip integration capacity [20–22]. However, to date, the gate fidelity remains below the QIP threshold due to unavoidable fabrication errors. CPs have not been previously used to correct for such errors as existing CP sequences require control of the phase of the coupling, whereas in integrated photonic circuits it is a real parameter. The present research is the first to address this limitation and to derive CPs that can be used in any qubit architecture including integrated photonics.

In this paper, we introduce the first composite sequences designed for off-resonant robust qubit inversion. We realize the desired high-fidelity population transfer by suitably choosing the detuning parameters while maintaining constant coupling throughout the constituent pulses. The presented general approach to derive detuning-modulated composite pulses of an arbitrary length N has a minimal pulse overhead and robust transfer is realized even for $N = 2$. In our analysis we consider a generic qubit which has many physical realizations including atomic and photonic systems (Fig. 1). We show that our sequences are stable to inaccuracies in various systematic parameters—coupling strength, duration, phase jitter, and resonance offsets—and achieve fidelities well above the QIP gate error threshold within the temporal lifetime of the system. Finally, we lay out the general recipe to implement the presented detuning-modulated composite sequences in integrated photonic systems for broadband high fidelity optical switching.

II. DETUNING-MODULATED COMPOSITE PULSES

The dynamics of a qubit $\{|1\rangle, |2\rangle\}$ driven coherently by an external electromagnetic field [Fig. 1(a)] is governed by the Schrödinger equation

$$i\hbar\partial_t \begin{bmatrix} c_1(t) \\ c_2(t) \end{bmatrix} = \frac{\hbar}{2} \begin{bmatrix} -\Delta(t) & \Omega(t) \\ \Omega^*(t) & \Delta(t) \end{bmatrix} \begin{bmatrix} c_1(t) \\ c_2(t) \end{bmatrix}. \quad (1)$$

Here, $[c_1(t), c_2(t)]^{\mathrm{T}}$ is the probability amplitudes vector, $\Omega(t)$ is the Rabi frequency of the transition, and $\Delta(t) = (\omega_0 - \omega)$ is the real-valued detuning between the laser frequency ω and the Bohr transition frequency of the qubit ω_0. In what follows, we assume $\Omega(t)$ and $\Delta(t)$ real and constant, which is well suited for the foreseen implementation in coupled waveguides and in optical elements for generating higher harmonics. However, we note that our composite sequences can also be implemented in physical systems with complex $\Omega(t)$.

*elkyoseva@gmail.com

 ©2019 American Physical Society

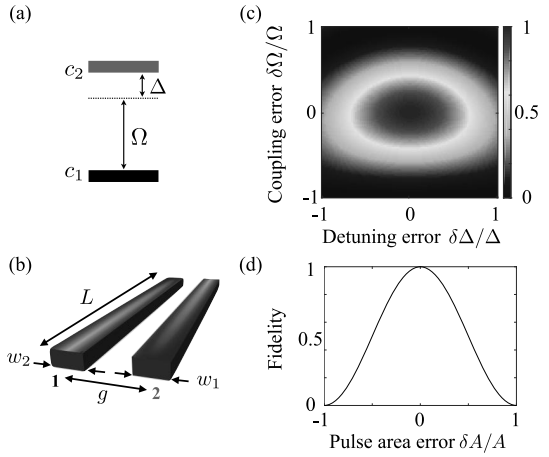

FIG. 1. Coherent qubit dynamics. Qubit realization in (a) an atomic system driven by a field with Rabi frequency Ω and detuning Δ and in (b) coupled waveguides of widths w_1 and w_2 at a distance g. (c) Population transfer fidelity as a function of detuning and coupling errors. (d) Resonant Rabi oscillations. The permissible gate infidelity is $<10^{-4}$.

The unitary propagator corresponding to Eq. (1) is found according to $U(t,0) = e^{-i/\hbar \int_0^t H(t)dt}$ and reads

$$U(\delta t) = \begin{bmatrix} \cos\left(\frac{A}{2}\right) + i\frac{\Delta}{\Omega_g}\sin\left(\frac{A}{2}\right) & -i\frac{\Omega}{\Omega_g}\sin\left(\frac{A}{2}\right) \\ -i\frac{\Omega}{\Omega_g}\sin\left(\frac{A}{2}\right) & \cos\left(\frac{A}{2}\right) - i\frac{\Delta}{\Omega_g}\sin\left(\frac{A}{2}\right) \end{bmatrix}. \tag{2}$$

Here, $\Omega_g = \sqrt{\Omega^2 + \Delta^2}$ is the generalized Rabi frequency and $A = \Omega_g \delta t$ is the pulse area with $\delta t = (t - t_0)$ being the pulse duration. The propagator $U(\delta t)$ evolves the state of the qubit from the initial time t_0 to the final time t according to $\mathbf{c}(t) = U(\delta t)\mathbf{c}(t_0)$. If the initial state of the qubit at t_0 is $|1\rangle$, the population of the excited state $|2\rangle$ at time t is given by the modulus squared of the off-diagonal propagator element $|U_{12}(\delta t)|^2$.

We assume the most general composite pulse sequence comprising N individual off-resonant pulses with Rabi frequencies Ω_n and detunings Δ_n. Given the individual pulse propagator $U_n(\delta t_n)$ from Eq. (2), the propagator for the total composite pulse sequence is expressed by the product

$$U^{(N)}(T,0) = U_N(\delta t_N)\, U_{N-1}(\delta t_{N-1}) \ldots U_1(\delta t_1), \tag{3}$$

where $\delta t_n = (t_n - t_{n-1})$ is the duration of the nth pulse ($t_0 = 0$ and $t_N \equiv T$). Below, we focus on the case of ingredient π pulses, i.e., $A_n = A = \pi$, which is easily realized by setting the pulse durations according to $\delta t_n = \pi/\sqrt{\Omega_n^2 + \Delta_n^2}$.

A. General propagator matrix

We require that the composite sequence produces a preselected single-qubit rotation T on the Bloch sphere at an angle θ,

$$T = \begin{bmatrix} \cos\theta & -i\sin\theta \\ -i\sin\theta & \cos\theta \end{bmatrix}. \tag{4}$$

That is, at the end of the pulse sequence the propagator from Eq. (3) should implement the target T. The exact form of the off-diagonal element of the composite propagator for an arbitrary *even* $N = 2n$ *pulse sequence* is given by

$$\left|U_{12}^{(2n)}(T,0)\right| = \prod_{s=1}^{2n} \frac{|\Omega_s|}{\sqrt{\Omega_s^2 + \Delta_s^2}} \left| \sum_{i=1}^{2n} (-1)^{i+1} \frac{\Delta_i}{\Omega_i} + \sum_{i<j<k=1}^{2n} (-1)^{i+j+k} \frac{\Delta_i}{\Omega_i}\frac{\Delta_j}{\Omega_j}\frac{\Delta_k}{\Omega_k} + \cdots + \sum_{i<\cdots<m=1}^{2n} (-1)^{i+\cdots+m+1} \underbrace{\frac{\Delta_i}{\Omega_i} \cdots \frac{\Delta_m}{\Omega_m}}_{2n-1} \right|, \tag{5}$$

while for an *odd* $N = (2n+1)$ *pulse sequence* by

$$\left|U_{12}^{(2n+1)}(T,0)\right| = \prod_{s=1}^{2n+1} \frac{|\Omega_s|}{\sqrt{\Omega_s^2 + \Delta_s^2}} \left| 1 + \sum_{i<j=1}^{2n+1} (-1)^{i+j+1} \frac{\Delta_i}{\Omega_i}\frac{\Delta_j}{\Omega_j} + \sum_{\substack{i<j< \\ k<l=1}}^{2n+1} (-1)^{i+j+k+l} \frac{\Delta_i}{\Omega_i}\frac{\Delta_j}{\Omega_j}\frac{\Delta_k}{\Omega_k}\frac{\Delta_l}{\Omega_l} + \cdots + \sum_{i<\cdots<m=1}^{2n+1} (-1)^{i+\cdots+m+1} \underbrace{\frac{\Delta_i}{\Omega_i} \cdots \frac{\Delta_m}{\Omega_m}}_{2n} \right|. \tag{6}$$

We require that $|U_{12}^{(N)}(T,0)| = |\sin\theta|$.

B. Complete population transfer

Below we focus on providing the protocol for the derivation of composite sequences, which produce a robust complete population inversion. The same protocol can be followed for any other rotation angle θ and we provide an example for $\theta = \pi/2$ in the Appendix.

For target $\theta = \pi$, we require that the modulus squared of the off-diagonal element from Eq. (3) should be equal to 1, $|U_{12}^{(N)}(T,0)| = 1$. To fulfill this condition we use the set of detunings $\{\Delta_n\}$ as *free control parameters*. We find that for a complete population inversion they need to obey a general analytical condition depending on the parity of N. For an even $N = 2n$, the condition is

$$1 + \sum_{i<j=1}^{2n} (-1)^{i+j+1} \frac{\Delta_i}{\Omega_i}\frac{\Delta_j}{\Omega_j} + \cdots + \sum_{i<\cdots<m=1}^{2n} (-1)^{i+\cdots+m+1} \underbrace{\frac{\Delta_i}{\Omega_i} \cdots \frac{\Delta_m}{\Omega_m}}_{2n \text{ times}} = 0, \tag{7}$$

while for an odd $N = (2n+1)$ it reads

$$\sum_{i=1}^{2n+1} (-1)^{i+1} \frac{\Delta_i}{\Omega_i} + \sum_{i<j<k=1}^{2n+1} (-1)^{i+j+k} \frac{\Delta_i}{\Omega_i}\frac{\Delta_j}{\Omega_j}\frac{\Delta_k}{\Omega_k} + \cdots + \sum_{i<\cdots<m=1}^{2n+1} (-1)^{i+\cdots+m+1} \underbrace{\frac{\Delta_i}{\Omega_i} \cdots \frac{\Delta_m}{\Omega_m}}_{(2n+1) \text{ times}} = 0. \tag{8}$$

Note that the above Eq. (7) or (8), depending on the parity of the composite pulse, is the only condition that the detuning and coupling parameters need to fulfill in order to realize a population inversion in the system.

The next step in our protocol is to find which subset of the solutions to Eqs. (7) and (8) produce an excitation profile that is maximally robust to variations in the pulse area A at selected value(s) of A. This is achieved mathematically by nullifying the even derivatives of the propagator element $\frac{\partial^k}{\partial A^k}|U_{12}^{(N)}(T,0)|^2$ at $A=\pi$. Note that the odd derivatives are always equal to zero. Thus for a *first-order CP* realizing a robust composite sequence that corrects for imperfections in the pulse area we need to nullify the second derivative, while for a *second-order CP*—the second and the fourth derivatives simultaneously. Note, that in contrast to previous works [10,11,18], the pulse area A for an off-resonant pulse is a function of all systematic parameters—pulse duration, amplitude, and detuning—and thus the detuning-modulated composite pulses presented here are *robust against various systematic errors*.

C. First-order composite pulses: Sign-alternating Δs

In the following we provide analytical solutions for broadband pulse sequences of arbitrary lengths N. In order to obtain the elegant analytical solutions for arbitrary N presented below we assume that the detuning and coupling parameters values are not completely arbitrary but they have equal ratios $|\frac{\Delta_i}{\Omega_i}|=|\frac{\Delta_j}{\Omega_j}|,\ \forall i,j$. The uncovered pulse symmetries represent a powerful analytical quantum control tool and allow for finding sequences of arbitrary lengths in a straightforward manner. The presented sequences will be straightforward to realize in NMR and in coupled waveguide qubits.

Our first-order composite pulse parameters are antisymmetric along their length, i.e., $\frac{\Delta_i}{\Omega_i}=-\frac{\Delta_{i+1}}{\Omega_{i+1}}\equiv\xi$ for $i=(1,\ldots,N-1)$. The rationale behind this is that the composite sequence needs to produce a change in the path of the state vector on the Bloch sphere (see the inset of Fig. 5). Then, the CPT conditions Eqs. (7) and (8) can be rewritten as the polynomial

$$\sum_{s=0}^{n}(-1)^s\binom{N}{N-2s}\xi^{N-2s}=0, \tag{9}$$

which is valid for both even $N=2n$ and odd $N=(2n+1)$ sequences. The roots of this polynomial provide the values of δ for which a complete population transfer is achieved and moreover $\frac{\partial^2}{\partial A^2}|U_{12}^{(N)}|^2$ at $A=\pi$ is nullified. For a flat-top broadband composite sequence we choose the root that minimizes the fourth derivative $\frac{\partial^4}{\partial A^4}|U_{12}^{(N)}|^2$ at $A=\pi$ (the polynomial is a symmetric function of ξ). Finally, we find that first-order detuning-modulated CPs of length N are realized for δ equal to the largest (in absolute value) root of the polynomial Eq. (9). In Table I we present the first several examples for CPs.

D. Second-order composite pulses: Antisymmetric Δs

Second-order CPs are of odd pulse length, $N=(2n+1)$, and similar to the first-order ones the ratios of the detunings and couplings are equal and antisymmetric with respect to the length of the pulse. That is, $\frac{\Delta_i}{\Omega_i}=-\frac{\Delta_{N+1-i}}{\Omega_{N+1-i}}\equiv\xi$, while the detuning of the middle pulse is $\Delta_{n+1}=0$. This antisymmetric arrangement fulfills the CPT condition Eq. (8) automatically and the second derivative is zero as it is proportional to the diagonal element of the propagator. To achieve a higher fidelity of the CPs we need to also nullify the fourth derivative $\frac{\partial^4}{\partial A^4}|U_{12}^{(N)}(T,0)|^2$ at $A=\pi$ and minimize the sixth. This task is simple numerically and in Table II we present a few examples of second-order CPs, which can easily be extended to large odd N.

TABLE I. First-order detuning-modulated CPs.

N	$\pm\left(\frac{\Delta_1}{\Omega_1},\frac{\Delta_2}{\Omega_2},\ldots\right)$
2	$(1,-1)$
3	$(1,-1,1)\sqrt{3}$
4	$(1,-1,1,-1)(\sqrt{2}+1)$

The above presented approach of tailoring the propagator element and its derivatives to achieve robustness against systematic parameters can be extended to implement other gates, i.e., create equal superposition between the states. In this case the propagator elements squared from (7) and (8) should be equal to $1/2$ and the derivatives with respect to any chosen systematic parameter should be nullified accordingly.

III. ROBUSTNESS OF THE DETUNING-MODULATED SEQUENCES

A. Pulse area errors and phase jitter

The infidelities of the first- and second-order composite sequences as a function of errors in the target pulse area are shown in Fig. 2. For easy reference, we include the fidelity of a resonant pulse and the QI gate error threshold [1]. Note that the infidelity of the population transfer is well below the QI benchmark even for $\delta A/A$ larger than 10% as compared to less than 1% for a resonant excitation. We achieve approximately an order of magnitude improvement in the error tolerance by adding a single pulse (first-order CP) and 1.5 orders of magnitude by adding two extra pulses (second-order CP). The pulse overhead scales as N, which is significantly better than that of previous proposals ($2N$) [10–12]. In our analysis we also allowed for Gaussian errors of 10% in the individual pulse areas and averaged over 100 times (with dashed curves). Note that any other first- and second-order pulses have similar robustness to the ones we show here as they nullify up to the same derivative of the propagator element and, for compactness, we have omitted them. Finally, we relaxed the assumption of real couplings Ω and allowed for a random

TABLE II. Second-order detuning-modulated CPs.

N	$\pm\left(\frac{\Delta_1}{\Omega_1},\frac{\Delta_2}{\Omega_2},\ldots,0,\ldots,\frac{\Delta_{N-1}}{\Omega_{N-1}},\frac{\Delta_N}{\Omega_N}\right)$
3	$(1,0,-1)\,2.5425$
5	$(1,-1,0,1,-1)\,5.09027$
7	$(1,-1,1,0,-1,1,-1)\,7.6375$

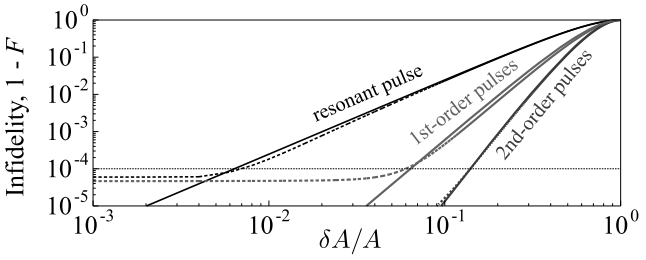

FIG. 2. Infidelity of the shortest first- (red) and second-order (blue) CPs vs area errors with (dashed curves) and without (solid curves) Gaussian noise of 10% in A averaged over 100 times. The point-dash blue curve shows the second-order pulse with a random phase error of 1%. The black curve shows the infidelity of a single resonant pulse and we also show the 10^{-4} QIP infidelity threshold.

phase jitter of 1% in the second-order pulse (dashed blue). We note that the error correction of our CPs is largely unaffected by such inaccuracies.

B. Detuning and coupling errors

We further examine the robustness of the detuning-modulated composite sequences in the presence of simultaneous detuning and coupling errors and show the population transfer fidelity in Fig. 3(a). We present the contour plots of the fidelity of the first-order (left) and second-order (right) CPs of length $N = 2$ and 3, respectively. Note that the contour plots for any other pulses from their respective families look similar. The area where the fidelity is above 90% is increased significantly as compared to that of a resonant pulse [Fig. 1(c)]. We also identify areas in the parameter space where the fidelity exhibits a notable stability against either detuning $\delta\Delta_i/\Delta_i$ or coupling $\delta\Omega/\Omega$ errors and mark them by horizontal and vertical cut lines in the contour plots. We zoom in on them in Figs. 3(b) and 3(c) and observe an increased robustness vs detuning and coupling errors.

C. In the presence of relaxation

As composite sequences require longer implementation times, it is important to test their fidelity against the lifetime of the system. Given relaxation, we substitute $\Delta \to (\Delta - i\gamma)$ in the diagonal elements of the Hamiltonian (1), and find the probability amplitude of each state according to $|c_i(t)|^2 e^{-\gamma t/2}$, where the relaxation time is $T_1 = \gamma^{-1}$. It is known that for free decay T_1 is independent of T_2 and there is an upper limit to the decoherence rate $T_2 \leqslant 2T_1$ [23,24]. We show the robustness of the population transfer with respect to γ in Fig. 4 where we have used experimentally reported decoherence values (Refs. [25–28]) to allow for γ of the order of Ω. The above analysis shows that the detuning-modulated sequences are a powerful tool for a robust qubit inversion even in the presence of decay or decoherence and that their implementation time is well within the decay time of the qubit.

IV. REALIZATION IN COUPLED WAVEGUIDES

The detuning-modulated CPs offer a unique solution to overcome inaccuracies in fabrication in integrated photonic

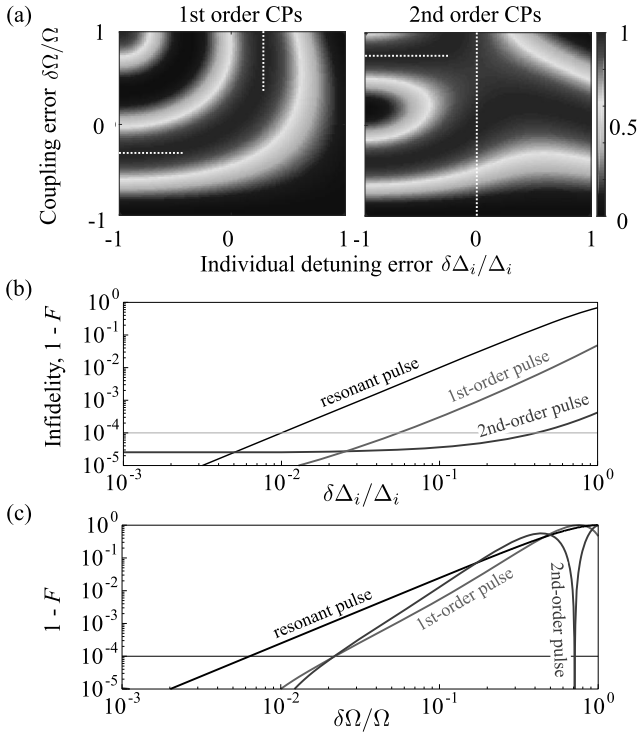

FIG. 3. Robustness of first- (left) and second-order (right) detuning-modulated sequences vs detuning and coupling errors. (a) Contour plots of the fidelity vs errors in both $\delta\Delta_i/\Delta_i$ and $\delta\Omega/\Omega$. The error tolerance is increased significantly as compared to the contour plot of a single resonant pulse, shown in Fig. 1(c). The infidelity, $1 - F$, along the horizontal (b) and vertical (c) cut lines from the contour plots from (a), where first-order pulses are in red and second-order pulses are represented with blue. For easy reference we show the 10^{-4} QIP infidelity threshold and the resonance pulse infidelity with black.

circuits. In Fig. 1(b), we show two evanescently coupled optical waveguides at a distance g measured from their center lines. Within the coupled-mode approximation [29], the amplitudes of the fundamental modes in the waveguides obey an equation analogous to Eq. (1) where the coupling is $\Omega = a\, e^{-bg}$ (a and b are material and geometry dependent). For constant g, Ω is also constant throughout the length. The system is on resonance if the waveguides have identical geometries; otherwise, there is a real-valued phase mismatch $\Delta = (\beta_1 - \beta_2)/2$ with $\beta_{1,2}$ being the respective propagation constants.

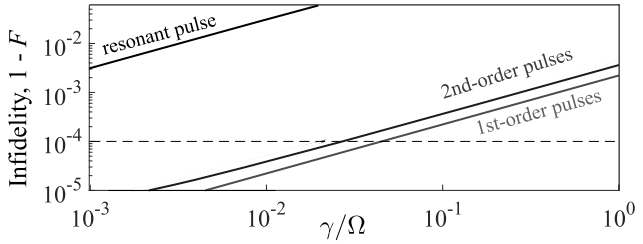

FIG. 4. Infidelity, $1 - F$, in log scale vs the decay rate in units of Ω for $N = 2$ first- and $N = 3$ second-order composite sequences and for a resonant pulse in red, blue, and black, respectively.

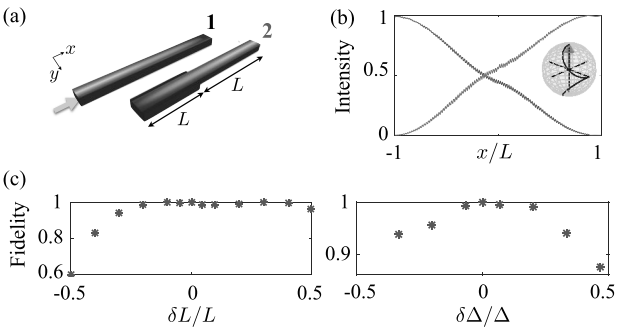

FIG. 5. Complete light transfer in a first-order $N = 2$ detuning-modulated composite waveguide coupler. (a) An out-of-scale schematic of the waveguide design with EME calculation. Light is initially injected in waveguide 1 and is then robustly transferred to waveguide 2. (b) Light intensity of waveguide 1 (blue, initially populated) and waveguide 2 (red, initially empty) vs normalized propagation length. The inset shows the path of the system's state vector on the Bloch sphere during the evolution. (c) Fidelity of the light transfer vs errors in (left) the propagation length L and (right) the target phase mismatch Δ.

Thus our sequences can be implemented by changing the waveguides' widths such that there are step changes in Δ along the length.

Figure 5(a) is an out-of-scale schematic of the $N = 2$ first-order CP in coupled waveguides of length $2L$. The width of waveguide 1, w_1, is fixed, while the width of waveguide 2 changes midlength from $1.034w_1$ to $0.966w_1$, realizing the required step change in Δ in Si on SiO_2 configuration. By employing an eigenmode expansion (EME) solver, we simulate the light propagation along the waveguides. We plot the light intensities in Fig. 5(b) along with the Bloch sphere path of the state vector. We realize a complete light switching and test its robustness to errors in the phase mismatch $\delta\Delta/\Delta$ and in the propagation length $\delta L/L$, shown in Fig. 5(c). We observe high fidelity light transfer in excellent agreement with the theoretical calculations (Figs. 2 and 3). Finally, in Fig. 6

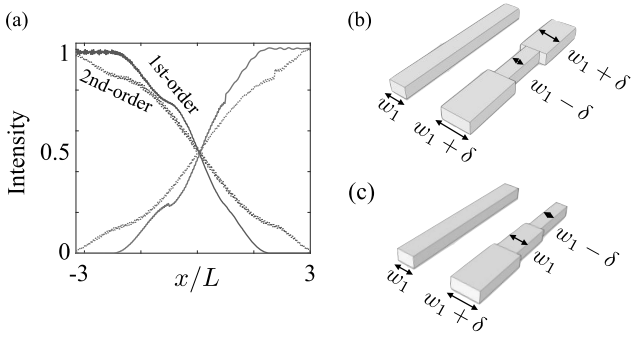

FIG. 6. (a) Light intensity as a function of normalized length of two composite waveguide couplers: one with first-order design as shown in (b) and one with second-order design as shown in (c). The light intensity of the initially populated waveguides [with blue curves in (a) starting from 1] is robustly transferred to the other waveguide [with red curves in (a) starting from zero].

we show light switching for $N = 3$ composite waveguides based on first- and second-order sequences.

V. CONCLUSIONS

We introduced a set of detuning-modulated composite pulse sequences that are robust to inaccuracies in various systematic parameters including duration, coupling strength, and off-resonance errors well within the system's lifetime. The control knobs, which we utilized to achieve broadband population transfer, are the detuning parameters of the constituent pulses, while the coupling constants remain unchanged. We achieved an inversion gate fidelity above the QI threshold vs errors of several percents in the pulse area for a sequence of only two constituent pulses and vs errors of over 10% for three constituent pulses. The presented composite pulses are radically different compared to existing composite sequences, which assume complex coupling parameters and modify their phases. Thus we believe that our analytical solutions will be the cornerstone for quantum information protocols in practical realization of high-fidelity quantum computing in integrated photonic circuits.

ACKNOWLEDGMENTS

E.K. acknowledges financial support from the European Union's Horizon 2020 research and innovation programme under the Marie Skłodowska-Curie Grant agreement No. 705256–COPQE. H.G. is supported by the Gertner Institute. H.S. acknowledges support by the Horizon 2020 European Research Council (ERC) Fund under the project MIRAGE 20-15 (Grant No. 639402). The authors acknowledge support from the Israel Science Foundation (ISF) Grant No. 1433/15 and the PAZY Young Investigator grant.

E.K. and H.G. contributed equally to this work.

APPENDIX: COMPOSITE PULSE FOR A ROBUST EQUAL SUPERPOSITION

An equal superposition between the two qubit states is realized when the rotation angle from Eq. (4) $\theta = \pi/2$. We focus on the shortest sequence with $N = 2$. Then, for the off-diagonal composite propagator element from Eq. (5) we have the condition

$$U_{12}^{(2)} = \frac{\frac{\Delta_1}{\Omega_1} - \frac{\Delta_2}{\Omega_2}}{\sqrt{\Delta_1^2 + \Omega_1^2}\sqrt{\Delta_2^2 + \Omega_2^2}} = -1/\sqrt{2}. \tag{A1}$$

We solve this equation for one of the independent parameters, $\frac{\Delta_1}{\Omega_1}$, and find that it is satisfied for $\frac{\Delta_1}{\Omega_1} = \frac{-1-\frac{\Delta_2}{\Omega_2}}{-1+\frac{\Delta_2}{\Omega_2}}$ and $\frac{\Delta_1}{\Omega_1} = \frac{-1+\frac{\Delta_2}{\Omega_2}}{1+\frac{\Delta_2}{\Omega_2}}$. We substitute this solution into the second derivative of $|U_{12}^{(2)}|^2$ with respect to A at $A = \pi$ and finds its roots. The exact expression is too cumbersome to be explicitly included here. Finally, we find the roots to be

$$\left(\frac{\Delta_1}{\Omega_1}, \frac{\Delta_2}{\Omega_2}\right) = \pm(-5.52, 0.69), \tag{A2}$$

which gives the interaction parameters of a two-pulse sequence that produces a robust equal superposition.

[1] M. Nielsen and I. Chuang, *Quantum Computation and Quantum Information* (Cambridge University Press, Cambridge, UK, 2000).
[2] E. L. Hahn, Phys. Rev. **80**, 580 (1950).
[3] H. Y. Carr and E. M. Purcell, Phys. Rev. **94**, 630 (1954).
[4] H. M. Cho, R. Tycko, A. Pines, and J. Guckenheimer, Phys. Rev. Lett. **56**, 1905 (1986).
[5] H. K. Cummins, G. Llewellyn, and J. A. Jones, Phys. Rev. A **67**, 042308 (2003).
[6] M. H. Levitt and R. Freeman, J. Magn. Reson. (1969) **33**, 473 (1979).
[7] R. Freeman, S. P. Kempsell, and M. H. Levitt, J. Magn. Reson. (1969) **38**, 453 (1980).
[8] M. H. Levitt, Prog. Nucl. Magn. Reson. Spectrosc. **18**, 61 (1986).
[9] R. Tycko, Phys. Rev. Lett. **51**, 775 (1983).
[10] B. T. Torosov and N. V. Vitanov, Phys. Rev. A **83**, 053420 (2011).
[11] B. T. Torosov, S. Guérin, and N. V. Vitanov, Phys. Rev. Lett. **106**, 233001 (2011).
[12] G. T. Genov, D. Schraft, T. Halfmann, and N. V. Vitanov, Phys. Rev. Lett. **113**, 043001 (2014).
[13] J. Keeler, *Understanding NMR Spectroscopy* (John Wiley and Sons, New York, 2005).
[14] A. A. Rangelov, N. V. Vitanov, and G. Montemezzani, Opt. Lett. **39**, 2959 (2014).
[15] A. A. Rangelov and E. Kyoseva, Opt. Commun. **338**, 574 (2015).
[16] E. Dimova, W. Huang, G. Popkirov, A. Rangelov, and E. Kyoseva, Opt. Commun. **366**, 382 (2016).
[17] I. Cohen, A. Rotem, and A. Retzker, Phys. Rev. A **93**, 032340 (2016).
[18] E. Kyoseva and N. V. Vitanov, Phys. Rev. A **88**, 063410 (2013).
[19] B. T. Torosov, E. S. Kyoseva, and N. V. Vitanov, Phys. Rev. A **92**, 033406 (2015).
[20] A. Politi, J. C. F. Matthews, and J. L. O'Brien, Science **325**, 1221 (2009).
[21] J. C. F. Matthews, A. Politi, A. Stefanov, and J. L. O'Brien, Nat. Photon. **3**, 346 (2009).
[22] R. J. Chapman, M. Santandrea, Z. Huang, G. Corrielli, A. Crespi, M.-H. Yung, R. Osellame, and A. Peruzzo, Nat. Commun. **7**, 11339 (2016).
[23] M. Frimmer and L. Novotny, Am. J. Phys. **82**, 947 (2014).
[24] G. Falci, A. D'Arrigo, A. Mastellone, and E. Paladino, Phys. Rev. Lett. **94**, 167002 (2005).
[25] E. Collin, G. Ithier, A. Aassime, P. Joyez, D. Vion, and D. Esteve, Phys. Rev. Lett. **93**, 157005 (2004).
[26] S. Takahashi, L. C. Brunel, D. T. Edwards, J. van Tol, G. Ramian, S. Han, and M. S. Sherwin, Nature (London) **489**, 409 (2012).
[27] T. Faust, J. Rieger, M. J. Seitner, J. P. Kotthaus, and E. M. Weig, Nat. Phys. **9**, 485 (2013).
[28] R. Hanson, O. Gywat, and D. D. Awschalom, Phys. Rev. B **74**, 161203(R) (2006).
[29] A. Yariv, IEEE, J. Quantum Electron. **9**, 9 (1973).

Additional Work

4

4.1 Persistent Photoconductivity (PPC) in $LaAlO_3/SrTiO_3$

Recent experimental observations [74, 75, 76] on optically enhanced coherent transport in superconductors open the possibility of ultrafast light-induced superconductivity even at temperatures above the critical temperature for a superconducting phase transition Tc. This has piqued my interest to combine our lab's expertise in ultrafast optical phenomena and near field optical nano-scaled measurements with superconductors and other highly correlated electron materials. The research directions are related to the recently reported transient phase transition in $YBa_2Cu_3O_{6.5}$ superconductors [74], occurring at T<Tc , with a timescale of the order of 7ps, due to a transient enhancement of the superfluid density of the superconductor. Moreover, the same qualitative behavior was observed above Tc, meaning that the photoinduced enhancement of the superfluid density persists, for temperatures of up to room temperature 300K. This was supported by fitting experimental data by the optical properties of a Drude metal. Similar results were reported for another superconducting material $La_{1.675}Eu_{0.2}Sr_{0.125}CuO_4$, for temperatures <20K [75].

These photoinduced dynamics were interpreted as a signature of an inhomogeneous light-induced phase, in which only a fraction of the equilibrium superconducting state is transformed. This is similar to the inhomogeneity found in the ultrafast insulator-metal transition (IMT) of VO_2 [77]. The timescales of this transition were found to vary from 40-200fs, due to the sensitivity of the photoinduced IMT to structural differences between different crystal areas, or a thermal transition, imaged by a near-field scanning optical microscope (SNOM).

In this research, I aimed to bridge the gap between highly correlated electron materials with ultrafast optics, and to introduce these materials into the field of nanophotonics. Near field studies of photoinduced phase transitions and other effects in these materials will allow to gain insight on the nature of these changes, their locality, their timescales and their physical origins.

A wide range of physical phenomena, such as superconductivity, ferroelectricity and electro-optic effects have been shown [78, 79, 80, 81, 82] in complex oxides, such as Strontium Titanate ($SrTiO_3$). $SrTiO_3$ is a wide-bandgap semiconductor (3.25eV at room temperature), whose electronic properties can be tuned by electron doping [83, 84]. Studies [85, 86, 87] report a strong temperature and electric field dependence of its dielectric constant, thus it is considered a strong candidate for oxide-based electronic devices [88, 89].

Moreover, at room temperature, when exposed to sub-bandgap light (2.9eV or higher), $SrTiO_3$ exhibits a persistent photoinduced change of its conductivity, with a twofold enhancement of free electron concentration, which maintains without decay for several days [90]. At room temperature, this persistent photoconductivity (PPC) can be attributed to oxygen vacancies created by annealing $SrTiO_3$ samples at $1200°C$ for one hour [90]. The annealed samples were exposed to photon energies ranging from 2-3eV, while the free-carrier absorption was measured in the far field. A threshold for PPC was observed at 2.9eV (430nm). Macroscopic measurements of the resistivity performed on these samples at $\lambda = 410nm$, above the threshold for PPC, conveyed a significant drop from $290\Omega cm$ before illumination to $0.6\Omega cm$ after it. The effect of exposing the annealed sample to sub-bandgap illumination can be explained via two processes in a band diagram that takes into account the electron conduction band and another band for the oxygen vacancies in the sample, i.e. a defect band, seen in Figure 4.1(a). In the first process, by illuminating the sample, a photon promotes an electron from the defect band to the conduction band. The defect relaxes into a metastable configuration, and in process two, electron recapture to the ground state can only occur if the electron has enough energy to overcome a thermal barrier.

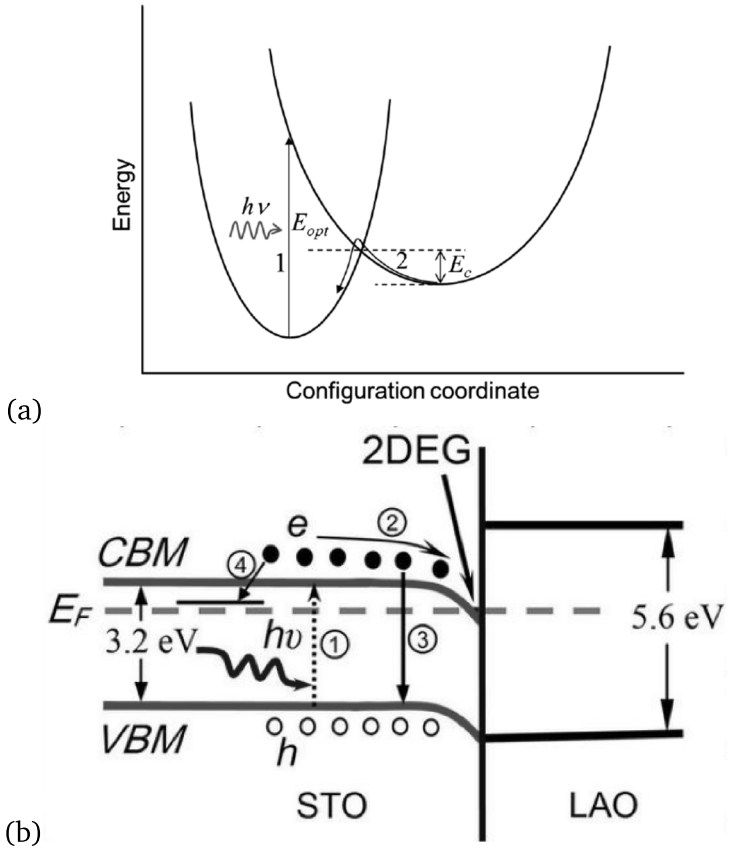

Fig. 4.1: Band diagrams of processes occurring in $LaAlO_3/SrTiO_3$ exposed to sub-bandgap illumination. (a) Figure taken from [90]. Defect configuration-coordinate diagram describing (1) excitation of electron into conduction band and (2) electron recapture. (b) Figure taken from [76]. Schematic diagram of band structure at the $LaAlO_3/SrTiO_3$ interface where the band bending is displayed.

4.1.1 Near Field Studies of PPC in $LaAlO_3/SrTiO_3$

The macroscopic phenomenon of persistent photoconductivity was more recently reported [76] in $LaAlO_3/SrTiO_3$ epitaxially grown oxide heterostructures. This material has been at the focus of scientific attention since it was discovered that a high-mobility two-dimensional electron gas (2DEG) appears at the interface of the two bulk insulating materials as the LAO thickness crosses a threshold of four unit cells [91]. This is popularly explained by a model, in which the polar sublayers of LAO cause an electric potential build-up as its thickness increases. To prevent a "polar catastrophe", a charge transfer of $0.5e^-$ per unit cell is transferred from the LAO layer to the $LaAlO_3/SrTiO_3$ interface, therefore creating a 2DEG.

Many intriguing physical properties have since been exhibited by these heterostructures, such as superconductivity, negative magnetoresistance, Kondo effect, and a coexistence of ferromagnetism and superconductivity. Persistent and transient photoinduced conductivity were measured at room temperature [76] in $LaAlO_3/SrTiO_3$ by illuminating 10u.c. samples with 365nm ($\approx 3.3eV$), which is between the bandgap of LAO (5.6eV) and STO. In this scenario, shown in Figure 4.1(b) the light irradiates the 2DEG interface at the STO side, and generates electron-hole pairs by passing through the LAO layer. This results in an increase of the electron density in the 2DEG, where the excited electrons falling into the potential well at the interface on the STO side are added into the 2DEG, and the holes are localized by small defects, such perhaps as oxygen vacancies. When the illuminating light is turned off, the trapped electrons in the 2DEG potential well do not recombine with holes due to the energy barrier, thus the conduction will maintain its increased value.

High-energy optical reflectivity, coupled with spectroscopic ellipsometry measurements have been performed on $LaAlO_3/SrTiO_3$ heterostructures under the conduction threshold [92] in order to gain a better understanding about the nature of the phase transition. A surprising charge distribution of $0.5e^-$ was observed within the LAO layers even in the insulating case, with no charge transfer to the interface. This may mean that even though macroscopically, the sample is still insulating, there may be a localized free electron density, which reaches the threshold to cross the barrier when the LAO layer is over 4u.c. thick.

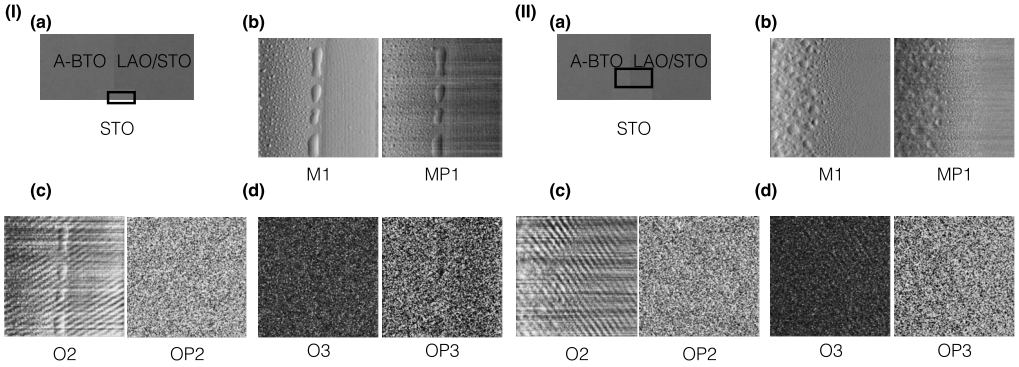

Fig. 4.2: Near field measurements of $LaAlO_3/SrTiO_3$ heterostructures (I) (a) Scheme of measured sample: amorphous BTO (in blue), $LaAlO_3/SrTiO_3$ heterostructure (in red) and atomically flat STO (in green). Black frame around area of interest - boundary between $LaAlO_3/SrTiO_3$ and STO. (b) Mechanical signal (left) and phase (right) of area of interest (c) Second harmonic of optical signal (left) and phase (right) of area of interest. (d) Third harmonic of optical signal (left) and phase (right) of area of interest. (II) (a) Black frame around second area of interest - boundary between amorphous BTO and $LaAlO_3/SrTiO_3$. (b) Mechanical signal (left) and phase (right) of area of interest (c) Second harmonic of optical signal (left) and phase (right) of area of interest. (d) Third harmonic of optical signal (left) and phase (right) of area of interest.

4.1.2 Experimental Setup of PPC Measurements

As the initial research question of interest was whether the phenomenon of PPC in $LaAlO_3/SrTiO_3$ heterostructures is local or of a carrier transporting nature, it was important to create a clear boundary between illuminated and non-illuminated areas of the samples. This was a challenging task, as any visible mechanical creation of a boundary, such as a scratch or a nanofabricated marker, causes significant debris on the surface of the sample, which is a scattering source that affects the measurements. Figure 4.2(I) shows both the mechanical and near-field optical signals obtained simultaneously, by measuring the boundary between two insulating materials: amorphous-BTO and atomically flat STO (Figure 4.2(Ia)). These scans are $10 \times 10\mu m$ in size, with a 150×150 pixel area and show the mechanical signal and phase (b), and the second and third harmonics of the optical signal (c) and (d). The optical signal at the higher harmonics is the pure near-field signal, yet we are not certain of its physical origin. To compare, we measured the boundary between amorphous-BTO and and $LaAlO_3/SrTiO_3$ heterolayer, shown in Figure 4.2(II). Here, the mechanical signal shows that the boundary is not smooth, and debris appears on the conducting side of the sample. This perhaps creates scattering sources which result in a stronger interference pattern shown in the third harmonic of the optical signal. We note that these measurements were performed with a $\lambda = 633nm$ near-field probe.

I performed SNOM measurements on 4-10u.c. samples of $LaAlO_3/SrTiO_3$ before illumination, and after exposing them to a 450nm UV lamp for $\approx 10min$. This time, the probe wavelength was $\lambda = 1530nm$. Both before and after illumination, we observed patches of high SNOM signal in both the illuminated and non-illuminated

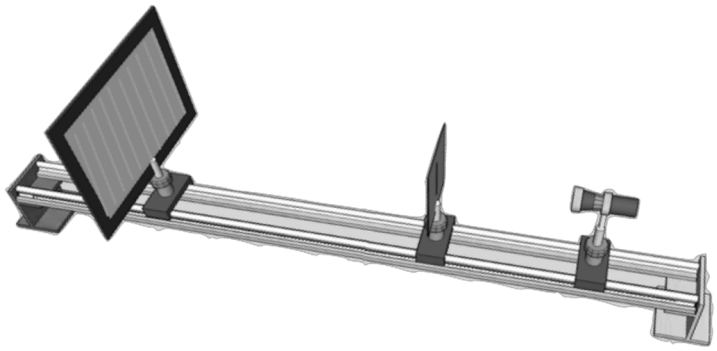

Fig. 4.3: Cartoon of single slit diffraction setup of PPC experiment.

areas of LAO. This might be a result of photoconductive effects diffusing across the sample, or background scattered light. All SNOM measurements displayed an optical interference pattern, that could not be associated with the miscut steps of $LaAlO_3/SrTiO_3$ or its electronic structure, as it appears in the amorphous BTO regions seen in Fig. 4.2 as well.

In order to control the areas of illumination, we set up a far-field diffraction experiment. We illuminated the samples with a SpectraPhysics MaiTai HP 70-100fs tunable ultrafast Ti:Sapp laser (690-1040nm), tuned to 730nm. The beam was focused to a nonlinear BBO crystal to produce via second harmonic generation the desired UV exposure wavelength of 365nm, which was impinged on a tunable single slit to create a diffraction pattern on the sample of interest, as depicted schematically in Fig. 4.3.

I scanned a 10u.c. $LaAlO_3/SrTiO_3$ heterostructure in the SNOM with a $\lambda = 685nm$ wavelength before and after exposing it to a UV diffraction pattern via a slit of 10-20μm in width. It is important to note that for these measurements, we used a tunable slit with a rotation resolution of 5μm, and essentially, we had no control over its absolute width. I will address this issue later in this section. The top row of Fig. 4.4 shows the third harmonic optical and optical phase SNOM $50x50\mu m$ channels scan of the 10 u.c. $LaAlO_3/SrTiO_3$ sample directly after exposure to the 365nm laser. As each scan had an area of 350x350 pixels with a 6.1ms integration time per pixel, it took a total of 25 minutes. The bottom row of Fig. 4.4 is the same two channels of the scan of the same sample in the same location, 15 hours post-illumination. The optical phase scan in Fig. 4.4(b) clearly shows a $7\mu m$ diffraction pattern, corresponding to a slit with a width of a few millimeters. To

better emphasize the details of the diffraction pattern created on the heterostructure, Fig. 4.5 shows cross correlations of the optical scans of the $LaAlO_3/SrTiO_3$ sample directly after illumination, one hour and 15 hours post illumination with respect to bulk STO unilluminated samples. The cutlines of each scan show obvious periodic patterns that decay over time. This suggests the existence of a *localized* persistent photoconductivity in $LaAlO_3/SrTiO_3$ heterostructures. However, the single slit diffraction pattern was too intense and difficult to control in order to analyze in a deterministic way. Therefore, I designed an experiment to expose $LaAlO_3/SrTiO_3$ and bulk $SrTiO_3$ samples to 365nm illumination through a series of double slits with a varying distance. The slits were fabricated at the Tel Aviv University Center for Nanotechnology and Nanoscience by evaporating a 10μm layer of Aluminum on a SiO_2 and opening two 10μm wide slits situated at distances of 3,5,7,9,11 millimeters. These will ensure a diffraction pattern with at least three intensity peaks on a sample exposed at a distance of 10 centimeters from the slits. Due to technical constraints, this experiment is currently pending results.

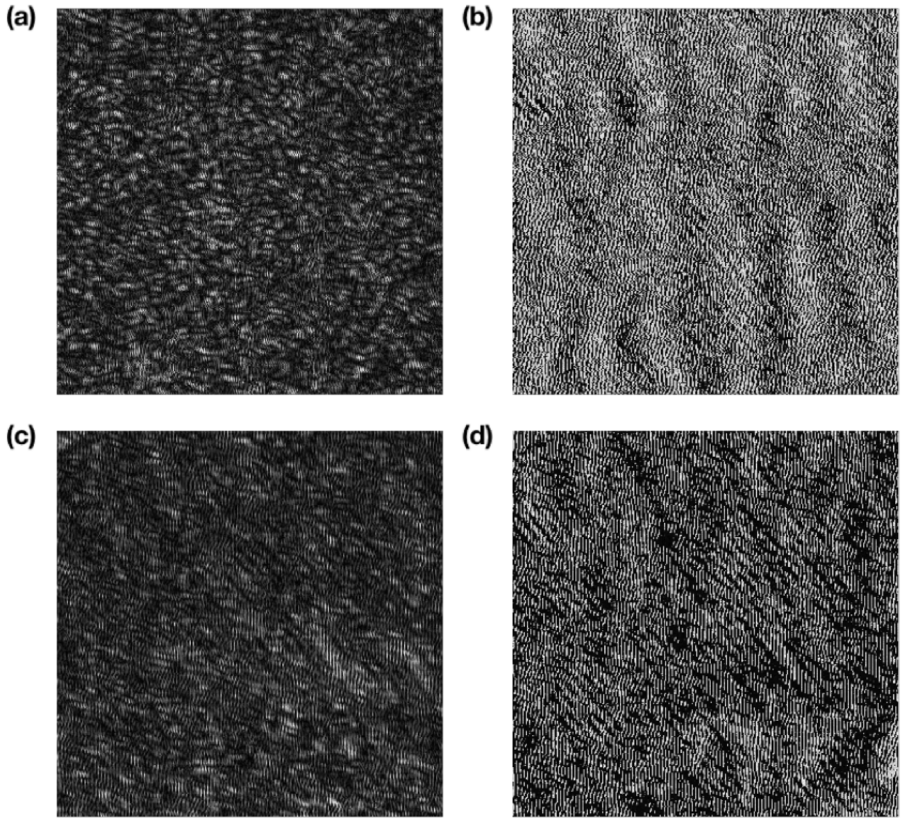

Fig. 4.4: Near field scanning optical microscope (SNOM) scans of $LaAlO_3/SrTiO_3$ heterostructure exposed to sub-bandgap illumination. (a) Third harmonic optical and (b) optical phase SNOM $50x50\mu m$ scan of $LaAlO_3/SrTiO_3$ heterostructure directly after exposure to 365nm laser. (c) Third harmonic optical and (d) optical phase signal of the above, 15 hours post-illumination.

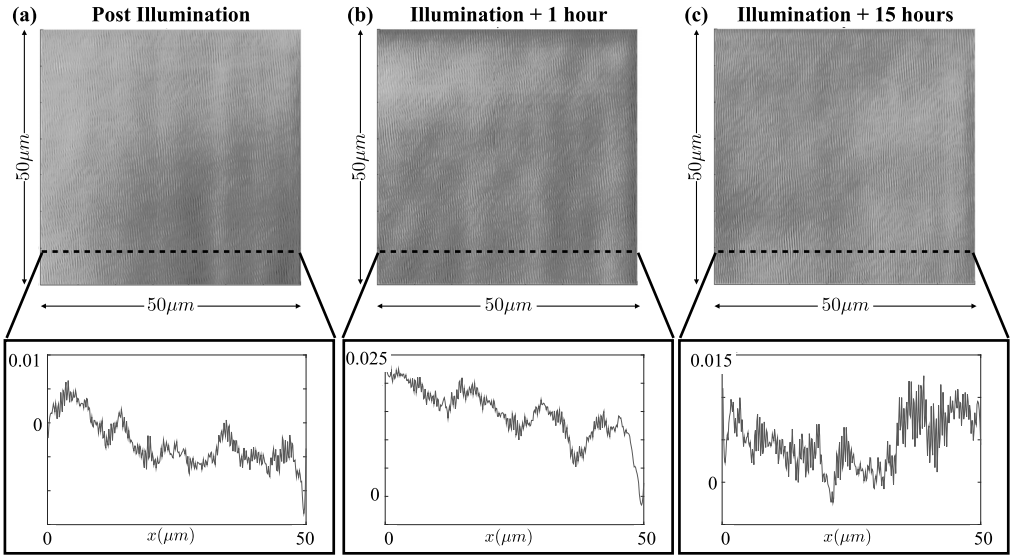

Fig. 4.5: Top: Cross correlation of 50x50um near-field scans of 10 unit cell $LaAlO_3/SrTiO_3$ samples with respect to bulk STO samples (a) immediately after exposure to a pulsed wavelength of 365nm illuminated through single slit for 10 minutes, (b) one hour post-illumination, and (c) 15 hours post-illumination. Bottom: Respective cut-lines of each scan shows a clear periodic pattern, decaying over time, suggesting localised persistent photoconductivity in $LaAlO_3/SrTiO_3$ heterostructures.

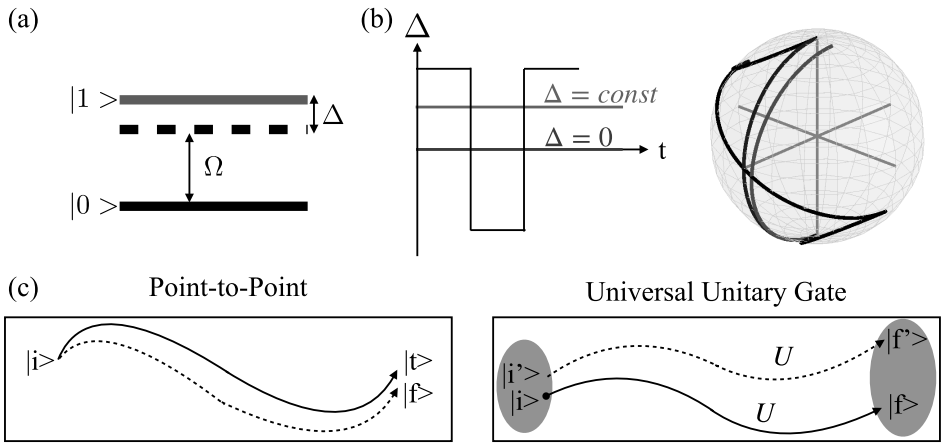

Fig. 4.6: Universal detuning-modulated composite pulses. (a) Schematic depiction of a qubit, a two-level quantum system with coupling Ω and detuning Δ. (b) Detuning as a function of time for a resonant (blue), constant detuned (red) and detuning-modulated (black) system with their respective trajectories on the Bloch sphere. (c) Point-to-Point rotation (left) from initial state $|i>$ to desired target state $|t>$ (continuous line) vs. erroneous experimental rotation to final state $|f>$. Universal unitary gate (right) U from initial state $|i>$ to target state $|f>$ preserves the unitary transformation from *any* other initial state $|i'>$ to the final rotated state $|f'>$.

4.2 Universal Detuning Modulated Composite Pulses

The work introduced in Chapter 2.2.2 produced composite pulses that address state transfer only from the initial state of the system. This is generally not suitable for quantum computers, that need general unitary rotations that perform well for any initial state. Thus, we began to expand this technique to address qubits in any initial state and developed the first detuning-modulated composite pulse sequence for the implementation of robust universal DMCPs within the finite lifetime of the system. These pulses are independent of the qubit's initial state and are robust to errors of up to tens of percent in the target values of the pulse area. Furthermore, our pulses are stable against the system's lifetime, maintaining fidelity above the QIP threshold of 10^{-4} for high values of the system's decay parameter, which is crucial for future implementation of scalable QIP circuits. Universal DMCPs will provide a basis for derivations of unitary gates applicable to a variety of qubit platforms. It is important to note that the robustness of universal DMCPs to errors in target coupling or detuning values separately reaches a lower fidelity of 10^{-2}. Additionally, while these pulses were designed to achieve stability to amplitude errors of the off diagonal element of the unitary propagator, its phase is not. Further derivations of unitary gates that are stable against amplitude and phase errors are beyond the scope of this work.

We begin to lay out the basis for universal detuning-modulated composite pulses by differentiating between two different types of pulses: point-to-point (PP) and

universal rotations (UR). The first are constructed to transform a given state to a desired final state, while the latter is designed to create a given rotation around a specific axis and angle for any arbitrary initial state. The PP solutions based on DMCPs developed in the previous section 2.2.2 for the most general qubit system [93].

In order to create state-independent single-qubit gates that are robust to various system inaccuracies and conclude in high-fidelity states, we apply a procedure adapted from a previous work [94] for constructing a UR pulse for a rotation angle θ from a PP pulse with half the angle $\theta/2$. We construct universal rotations from a series of sign-reversed palindromic DMCPs. In order to create a rotation by the angle θ around axis k, the unitary transformation $U_k(\theta) = e^{-i\theta I_k}$ can be decomposed to two consecutive rotations of angle $\theta/2$ around the k axis. Moreover, a θ rotation around the the $\hat{x}$ axis can be decomposed to two PP pulse sequences:

$$U_x(\theta) = V(v)\overline{V}^{tr}(v), \tag{4.1}$$

where $V(v)$ is the propagator describing a $\theta/2$ rotation PP sequence around a given range of axis offsets v and $\overline{V}^{tr}(v)$ is its time and phase-reversed counterpart. Namely, a UR pulse is constructed by concatenating the original pulse sequence $V(v)$ to the time and phase-reversed pulse sequence $\overline{V}^{tr}(v)$. The phase reversal can be done around any axis; for e.g. $\hat{z}$, this results in $-\hat{z}$, which is a sign reversal of the detuning parameter. Note that for $\hat{x}$, since $\phi = 0$, phase reversal of the pulse results in $\hat{x}$.

To achieve universal DMCPs with the aforementioned formalism, we reversed the sign of the detunings calculated for half the target rotation angle values of a DMCP [93].

The construction of an $N-$ piece universal detuning-modulated θ pulse is as follows:

1. For $V(v)$, calculate a $N/2$-piece detuning-modulated $\theta/2$ pulse sequence with $N/2$ values of $\Delta = \Delta_1, ..., \Delta_{N/2}$, where the rotation axis offsets v are calculated according to the resulting Bloch vector frequency $-\Omega_i/\Omega_{g,i}\hat{x} + \Delta_i/\Omega_{g,i}\hat{z}$ (see Fig. 4.7).

2. The detuning-reversed $\overline{V}^{tr}(v)$ is the above sequence with $\overline{\Delta} = -\Delta_{N/2}, ..., -\Delta_1$.

3. The complete $N-$ piece universal detuning-modulated sequence is the concatenation of the two seqeuences.

In the following, we devise the minimal *first-order* universal detuning-modulated composite sequences. These are the family of solutions that nullify up to the third derivatives of the off diagonal element of the total propagator with respect to the pulse area around $A = \pi$ [93].

To achieve the shortest universal detuning-modulated π pulse with $N = 4$ pieces, we calculated a $\pi/2$ detuning-modulated pulse sequence composed of $N/2 = 2$-pieces

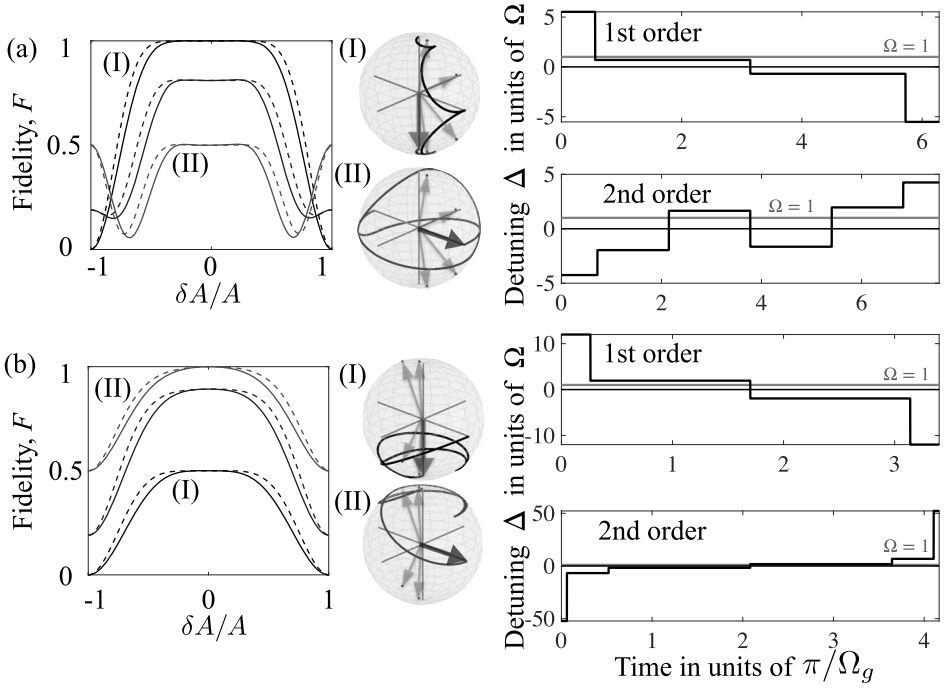

Fig. 4.7: Fidelity of detuning-modulated universal single-qubit DMCPs. (left) First- (continuous lines) and second-order (dashed lines) (a) π and (b) $\pi/2$ pulse vs. errors in the pulse area for different initial states $|0\rangle$ (I - black), $1/\sqrt{2}(|0\rangle + |1\rangle)$ (II - red) and 0.9 (blue) with matching (center) first-order trajectories on the Bloch sphere. These trajectories are plotted around the vector frequencies $-\Omega_i/\Omega_{g,i}\hat{x} + \Delta_i/\Omega_{g,i}\hat{z}$ (red arrows), which directly correspond to the axes offsets of the propagator $V(v)$ (see text for details). The construction of the universal pulses by detuning modulation (right) for first- (N=4) and second-order (N=6) pulse sequences as a function of time in units of the generalized Rabi frequency. All sequences are demonstrated with constant and normalized coupling $\Omega = 1$.

as $V(v)$ with two values of $\Delta = (\Delta_1, \Delta_2)$. An equal superposition between the two qubit states is realized when a single-qubit rotation T is at an angle $\theta = \pi/2$:

$$T = \begin{bmatrix} \cos\theta & -i\sin\theta \\ -i\sin\theta & \cos\theta \end{bmatrix}. \tag{4.2}$$

For $N/2 = 2$, the condition for the off-diagonal DMCP propagator element reads [93]:

$$|U_{12}|^2 = \frac{\frac{\Delta_1}{\Omega_1} - \frac{\Delta_2}{\Omega_2}}{\sqrt{1+\frac{\Delta_1}{\Omega_1}}\sqrt{1+\frac{\Delta_2}{\Omega_2}}} = -1/\sqrt{2}. \tag{4.3}$$

Solving this equation for one of the independent parameters, $\frac{\Delta_1}{\Omega_1}$, we find that it is satisfied for $\frac{\Delta_1}{\Omega_1} = (-1 - \frac{\Delta_2}{\Omega_2})/(-1 + \frac{\Delta_2}{\Omega_2})$ and $\frac{\Delta_1}{\Omega_1} = (-1 + \frac{\Delta_2}{\Omega_2})(1 + \frac{\Delta_2}{\Omega_2})$. For a first-order sequence, this solution is plugged into the second derivative of $|U_{12}|^2$ with respect to A at $A = \pi$ and we find its roots:

$$\left(\frac{\Delta_1}{\Omega_1}, \frac{\Delta_2}{\Omega_2}\right) = \pm(5.52, 0.69). \tag{4.4}$$

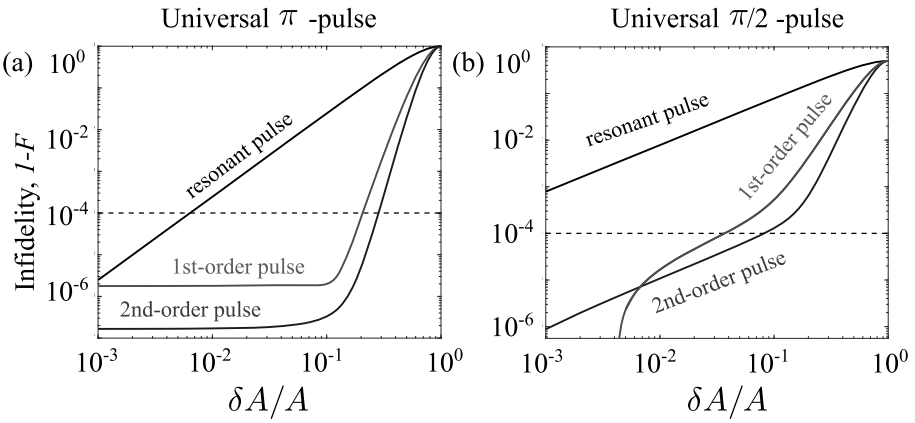

Fig. 4.8: Infidelity *(1-F)* in logarithmic scale of detuning-modulated universal CPs. Infidelity of first-(red) and second-order (blue) (a) π and (b) $\pi/2$ pulses to pulse area errors. These pulses outperform single resonant pulses, plotted for reference in black. They maintain robustness within the 10^4 QIP infidelity threshold, shown as a dashed black line, for errors of up to at least 10% from the target pulse area value.

N	Order	$(\frac{\Delta_1}{\Omega_1}, \frac{\Delta_2}{\Omega_2}, \ldots, -\frac{\Delta_2}{\Omega_2}, -\frac{\Delta_1}{\Omega_1})$
4	1	$\pm(5.52, 0.69, -0.69, -5.52)$
6	1	$(5.89, 1.01, -5.68, 5.68, -1.01, -5.89)$
6	2	$(-4.25, -1.96, 1.65, -1.65, 1.96, 4.25)$

Tab. 4.1: Detuning parameters for universal detuning-modulated composite π pulses.

This gives the interaction parameters of a 2-piece sequence that produces a robust detuning-modulated $\pi/2$ pulse [93]. Given this and the above formalism, the shortest universal DMCP is $\Delta_i = \pm(5.52, 0.69, -0.69, -5.52)\,\Omega$. This sequence enables a π rotation for any initial qubit state, and is very robust to errors in target pulse areas. To increase robustness to the above errors, we solved for the family of *second-order* universal detuning-modulated pulses, nullifying up to the sixth derivative of the modulus squared value of the total propagator with respect to A at $A = \pi$. These result in sequences with a minimal length of $N = 6$. We show the shortest solutions for first- and second-order universal detuning-modulated π pulses in Table 4.1.
In order to create universal and robust single-qubit $\pi/2$ pulse, two steps are required. The above technique is used to first derive a detuning-modulated $N/2 = 2$-piece $\pi/4$ pulse sequence. Then we reverse the sign of the detuning to create a universal sequence with $\Delta_i = (11.99, 1.94, -1.94, -11.99)\,\Omega$. The shortest sequences for first- and second-order detuning-modulated composite $\pi/2$ pulses are shown in Table 4.2.

N	Order	$(\frac{\Delta_1}{\Omega_1}, \frac{\Delta_2}{\Omega_2}, \ldots, -\frac{\Delta_2}{\Omega_2}, -\frac{\Delta_1}{\Omega_1})$
4	1	$(11.99, 1.94, -1.94, -11.99)$
6	1	$(-0.97, 0.97, 0.37, -0.37, -0.97, 0.97)$
6	2	$(-52.23, -6.76, -1.74, 1.74, 6.76, 52.23)$

Tab. 4.2: Detuning parameters for universal detuning-modulated composite $\pi/2$ pulses.

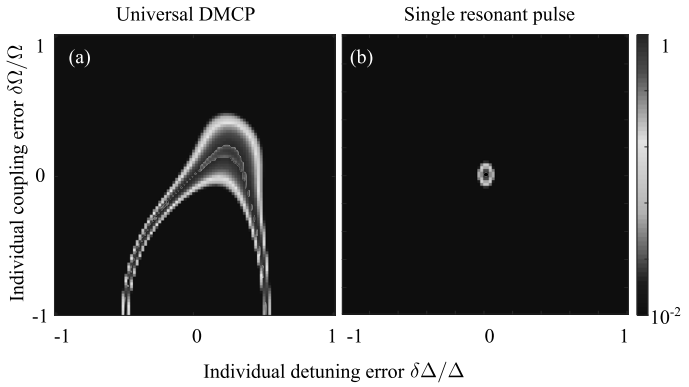

Fig. 4.9: Contour plots of the robustness of universal unitary detuning-modulated pulses. (a) Fidelity of a 1st-order universal unitary π pulse against errors in individual detuning $\delta\Delta/\Delta$ and coupling $\delta\Omega/\Omega$ errors. The color scale ranges from a fidelity of 10^{-2} to a fidelity of 10^{0}; in grey scale we accent the contour for which the fidelity is within the 10^{-4} QIP threshold. (b) Fidelity of a single resonant pulse against errors in the coupling and detuning. A single point on this contour plot achieves fidelity higher than 10^{-4}.

We tested the fidelity of universal DMCPs against various target system parameters. We evaluate the robustness of the pulses as a function of target values of pulse areas for different initial states (see Fig. 4.7). The robustness to errors maintains a high fidelity that is independent of the system's initial state, and increases for the second-order pulses plotted as dashed lines. We plot the infidelity of these pulses in logarithmic scale (see Fig. 4.8) and compare it to that of a single resonant pulse and the QIP infidelity threshold of 10^{-4} for reference. The universal π pulses display robustness to errors of up to 28% in the target pulse area while the universal $\pi/2$ pulses are robust to errors of up to 8%, compared e.g. with the 0.6% robustness of a single resonant π pulse.

In the detuning-modulated case, the pulse amplitude is a function of the coupling and the detuning. Any error in the pulse amplitude can be attributed to an error in the time in which the pulse was impinged on the system (as in the previous analysis) or to an error in either the coupling or the detuning. Thus, we studied the fidelity of the pulses as a function of the target detuning and coupling values, under the assumption that the realized time for each pulse was the target time (errorless). Fig. 4.9(a) is a contour plot of the first-order universal detuning-modulated π pulse fidelity, as a function of errors in the individual target coupling and detuning values. The color scale of this plot is from a fidelity of 10^{-2} to 10^{0}, and we accent in greyscale the contour of the combined values of coupling and detuning that achieve fidelities above 10^{-4}. For a single resonant pulse, this contour is minimized to a single black point of an errorless coupling value, as seen in Fig. 4.9(b). We provide full-ranged contour plots for the fidelity of the universal DMCPs against errors in the target coupling and detuning values in Fig. 4.10.

As composite sequences are comprised of a series of pulses, their overall implementation time is longer than that of a single resonant pulse. Therefore, one must also test

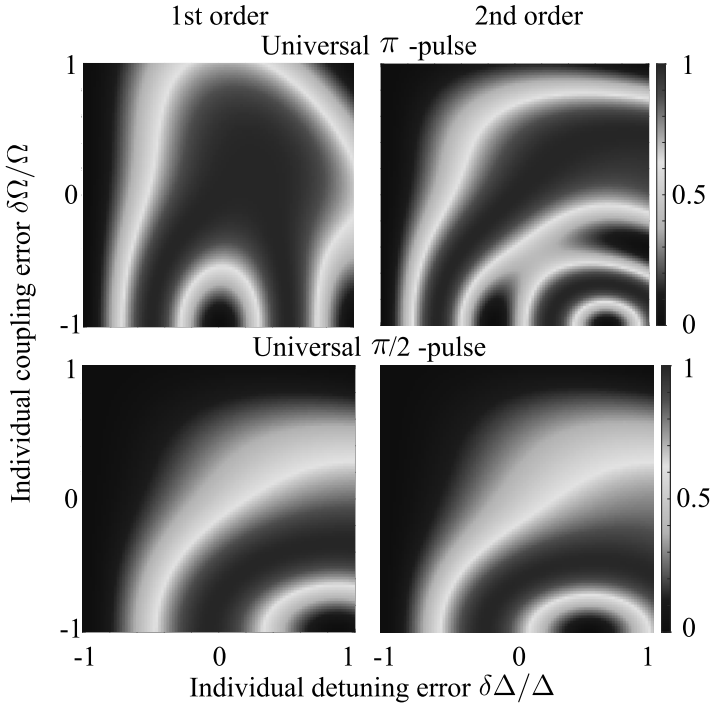

Fig. 4.10: Contour plots of the robustness of universal detuning-modulated pulses. 1st- (left) and 2nd-order (right) universal π (top) and $\pi/2$ (bottom) detuning-modulated pulses as a function of individual detuning $\delta\Delta/\Delta$ and coupling $\delta\Omega/\Omega$ errors. The contour plots show large areas in which the pulses are robust to errors in target values of these parameters.

their fidelity against the system's lifetime. Substituting $\Delta \to \Delta - i\gamma$ in the diagonal elements of the Hamiltonian presented in the main text, we find the probability amplitude of each state according to $|c_i(t)|^2 e^{-\gamma t/2}$, where γ is the characteristic relaxation time of the system is $T_1 = \gamma^{-1}$. For free decay, T_1 is independent of T_2, and there is an upper limit [95, 96] for the decoherence rate $T_2 \leq 2T_1$. Fig. 4.11 presents the robustness of both the π and $\pi/2$ pulses to with respect to γ. We considered experimentally reported values of γ of the order of Ω [97, 98, 99, 100] to show that our pulses are robust to decoherence and that their implementation time is well within the decay rate of the qubit.

The presented formalism for universal detuning modulated composite pulses is suitable for any irreducible n-level system with SU(2) symmetry (note that in this chapter, we define capital N as the number of pulses in a composite sequence and lowercase n as the number of levels in a multi-level system). I consider non-degenerate levels, in which the diagonal elements of the Hamiltonian representing the system's dynamics are the cumulative detunings of the excitation laser frequency from each Bohr frequency Δ_n and the off-diagonal elements link the different dipole transition moments between each two adjacent levels to the exciting electric field amplitude whose carrier frequency matches the Bohr frequency of this exact transition, namely Ω_n (i.e. the Rabi frequency for a transition between two adjacent levels). A variety of n-level solutions has been presented over the years, and in

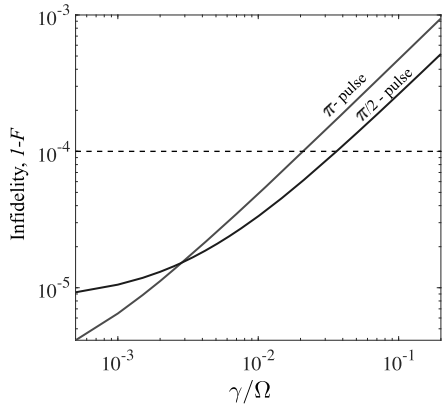

Fig. 4.11: Robustness of universal detuning-modulated CPs vs relaxation. Infidelity, $1-F$, of universal π (red) and $\pi/2$ (blue) pulses in logarithmic scale as a function the system's decay rate in units of Ω. The pulses maintain robustness within the 10^4 QIP infidelity threshold, shown as a dashed black line, for decay rates lower than 10% of the system's coupling value. The infidelity of a single resonant pulse is out of the scale of this graph.

our manuscript, we refer to the Jacobi solution, given by $\Omega_n = \Omega_0\sqrt{n(N-n)}$ and $\Delta_n = n\Delta_0 + D_0$. By using the irreducible matrix representation for SU(2) symmetry it was shown [65] that these off-diagonal elements are not necessarily equidistant. Taking note of the three-level system in Fig. 4.12(a), one of the two level pairs can be illuminated and excited with one of three fields: $\epsilon_{L1}(t) = A_{L1}e^{i\omega_{L1}t}$ with detuning $\Delta_{10} = \omega_{L1} - \omega_{10}$ or $\epsilon_{L2}(t) = A_{L2}e^{i\omega_{L2}t}$ with detuning $\Delta_{21} = \omega_{L2} - \omega_{21}$. In this case, the Rabi frequencies are $\Omega_{10} = 2A_{L1}(t)d_{10}/\hbar$ and $\Omega_{21} = 2A_{L2}(t)d_{21}/\hbar$. Assuming the above-mentioned Jacobi solution, and choosing $D_0 = 0$, we set the excitation laser frequencies, such that the detunings are $\Delta_{10} = \Delta_0$ and $\Delta_{21} = 2\Delta_0$. One can also chose the values of A to comply with the Rabi frequencies in this solution, which will be equal in this case $\Omega_{10} = \Omega_{21} = \sqrt{2}\Omega_0$.

In the following, I present an implementation of the above universal detuning-modulated composite pulses method to control a three-level system described by the SU(2) Hamiltonian:

$$H = Re\Omega_g\hat{\sigma_x} + Im\Omega_g\hat{\sigma_y} + \Delta\hat{\sigma_z} \tag{4.5}$$

where σ_i are the 3×3 Pauli matrices. Assuming a $N = 4$-piece universal detuning-modulated composite π pulse, the system's evolution is described by the composite unitary matrix $U^{(N=4)} = U_4U_3U_2U_1$, where U_i, described by eq. 2.11, is the unitary propagator or the piece-wise Hamiltonian $H_i = Re\Omega_{g,i}\hat{\sigma_x} + Im\Omega_{g,i}\hat{\sigma_y} + \Delta_i\hat{\sigma_z}$.

For the sake of simplicity, we will set a constant coupling $\Omega_i = \Omega$, such that the complete composite sequence is governed by the detuning parameters derived in the above section. We reprise the shortest *first-order* universal detuning modulated composite solution $\Delta = [5.52, 0.69, -0.69, -5.52]\Omega$ and implement it on a three-level SU(2) symmetric system. This results in robust palindromic state transfer shown in Fig. 4.12(b) that is robust to errors in the target pulse area from any initial state

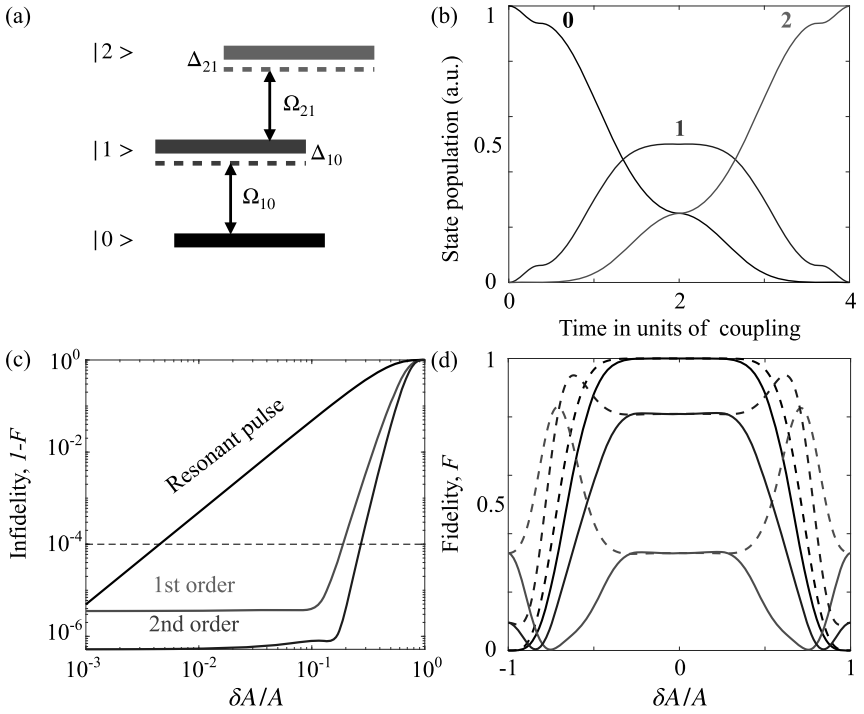

Fig. 4.12: Implementation of universal DMCPs in n-level systems with SU(2) symmetry. (a) A three-level irreducible system with Rabi frequencies $\Omega_{i,i+1}$ and detunings $\Delta_{i,i+1}$. (b) Palindromic state transfer from $|0>$ to $|2>$ in a three-level system due to a first-order universal $N = 4$ detuning-modulated composite π pulse. (c) Infidelity *(1-F)* of the above first-order (red) and second-order (blue) π pulse in logarithmic scale to errors in the target pulse area. Both outperform a single resonant pulse, shown in black for comparison, maintaining fidelity that is higher than the threshold for quantum information processing up to errors of $\delta A/A = 18\%$ for the first-order case and $\delta A/A = 27\%$ for the second-order case. (d) Fidelity (F) of the shortest first-(continuous lines) and second-order (dashed lines) universal detuning-modulated composite π pulses to errors in the target pulse area for different initial states: $|0\rangle$ (black), $1/\sqrt{3}(|0\rangle + |1\rangle + |2\rangle)$ (red) and $0.9|0\rangle + \sqrt{0.19/2}(|1\rangle + |2\rangle)$ (blue).

(Fig. 4.12(c-d)). The contour plot describing the robustness of this pulse sequence to errors in the target coupling and detuning parameters is similar to that of a two-level system. We note that as the unitary matrix elements grow in complexity for higher-level systems ($n \geq 4$), the shortest second-order sequence does not always outperform the first. That being said, all sequences maintain high fidelity against pulse area errors above the QIP threshold of 10^{-4}.

4.2.1 Realization in Quantum Integrated Photonic Circuits

As detuning-modulated CPs enable implementation in systems with real-valued couplings, it is straightforward to realize the above universal sequences in quantum integrated photonic circuits [101, 102], which suffer from inaccuracies originating from fabrication defects and environmental characteristics (i.e. temperature). Universal detuning-modulated CPs not only allow to overcome inevitable fabrication errors in such integrated devices, but relax the need for a precise initial state of light coupled into the system in order to achieve accurate gate operations.

Fig. 4.13(a) schematically shows a photonic circuit comprised of two coupled optical waveguides, situated at a distance of g from their center lines. The amplitudes of the fundamental modes in the waveguides follow the coupled mode equations [39]. Similar to Eq. 2.10, the coupling is $\Omega = ae^{-bg}$, where a, b are material and geometry-dependent. The system is said to be on resonance if the two waveguides are identical in material and geometry, otherwise there exists a real-valued phase mismatch between the propagation constants β_i which we define as the detuning $\Delta = (\beta_1 - \beta_2)/2$. The universal detuning-modulated CPs can be applied to such a system by varying the relative widths of the waveguides to create discrete changes of Δ along the propagation axis. For further details of this realization, see section 6. Fig. 4.13(a) is a top view of the light intensity propagation of a $N = 4$-piece coupled waveguide system that realizes the required changes in Δ to obtain a π pulse (Table 4.1). This was simulated via an eigenmode expansion solver (EME) [103]. The light intensity at the center line of each waveguide is plotted to stress the complete light switching in the coupled system in Fig. 4.13(b).

In the Appendix, I present a scheme to translate the theoretical parameters of detuning-modulated composite pulses to executable geometric designs of integrated photonic systems. Namely, I lay out the steps taken to scale and tweak the detuning parameters for N-piece DMCPs for coupled waveguides.

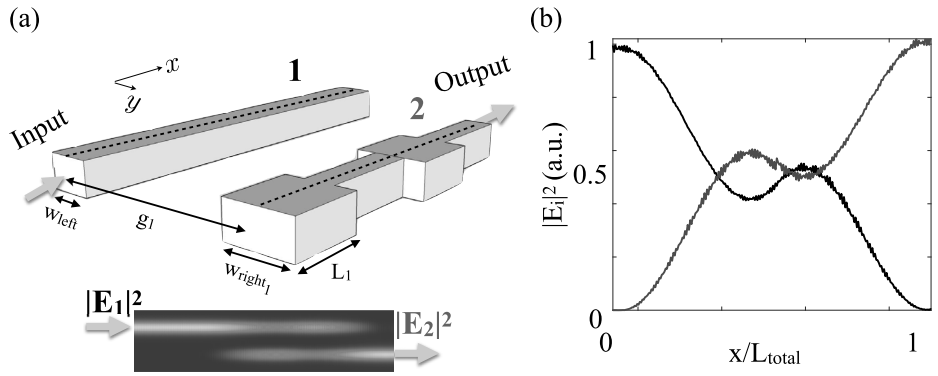

Fig. 4.13: Complete light switching in a universal detuning-modulated composite waveguide coupler. (a) (top) An out-of-scale schematic of the *first-order* $N = 4$-piece waveguide design. Light is initially injected to waveguide 1 and is transferred to waveguide 2. (bottom) Top-view of an eigenmode expansion solver (EME) calculation of the light intensity of the coupled waveguide system. (b) A cutline of the electromagnetic field intensity in the middle of waveguide 1 (black, initially populated) and waveguide 2 (red, initially empty) vs the normalized propagation length.

Discussion and Future Research 5

5.1 Near Field Optics and Dynamics

We developed a multifrequency excitation and detection method to achieve improved optical contrast in near-field optical measurements, while maintaining a high signal to noise ratio. In Fig. 5.1, I present an experimental comparison of mono-modal vs. bi-modal SNOM measurements to highlight this feat. I measured the same plasmonic gold nanobar on ITO, illuminated at 1550nm and excited separately via (a) mono-modal tip excitation at frequency f and demodulation at $4f$ and (b) bi-modal tip excitation at frequencies f and f' and demodulation at $2(f+f')$. The signal intensity was measured at its strongest spatial point at all available demodulation frequencies per excitation. It is immediately apparent that while the optical contrast remains similar (as seen in publication 1, in Chapter 3.1), the difference in the signal intensity compared to that achieved by demodulation of the fundamental frequency is very significant - the high contrast signal drops to 0.1% in the mono-modal case but only 50% in the bi-modal case.

This method utilizes fast signal processing to diminish the trade-off between optical contrast and SNR. Thus far, all of our measurements were performed on materials in the steady-state, with spatially-resolvable features. An interesting avenue to approach with MF-SNOM would be to perform conclusive measurements to show that this improvement leads to higher resolution. Furthermore, as this imaging method is temporally limited by raster-scanning and single-pixel integration times, transient effects of near-field light-matter interactions are very difficult to measure. While past research has been able to combine between the ultra-small spatial resolution the SNOM has to offer with the ultra-fast temporal resolution of pump-probe microscopy [104], the resultant measurements were of a highly complex interference pattern of many excitation points over time. One way to overcome this would be to apply sparse sampling [105, 106], since the sparse signal resides mainly in the vicinity of the location of excitation, in order to allow for faster image processing [107].

Near Field Studies of Persistent Photoconductivity in $LaAlO_3/SrTiO_3$

In the following, I present suggestions for future work to gain a better understanding of the underlying mechanism of persistent photoconductivity in $LaAlO_3/SrTiO_3$ heterostructures.

One possible research avenue would be to couple an optical fiber to the SNOM in order to locally control the excitation of the measured sample. This will enable the simultaneous change of resistivity of the sample with an adequate wavelength, and

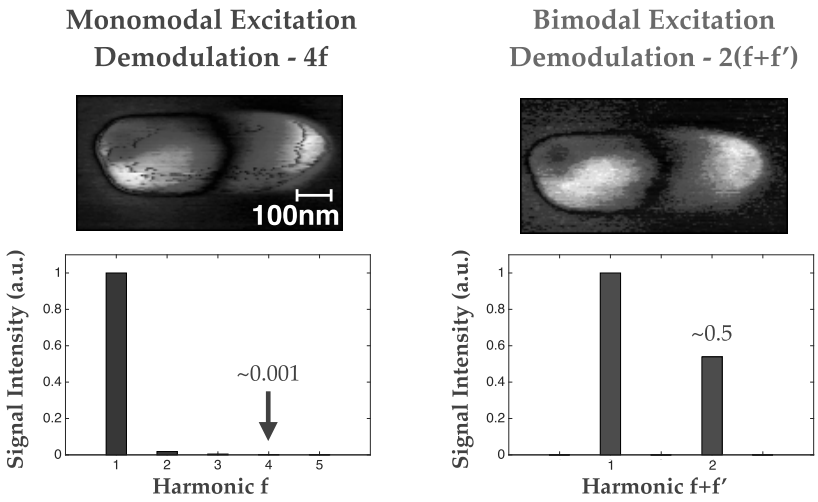

Fig. 5.1: Near-field optical measurements of a gold nanobar, illuminated at 1550nm. On the left, we used mono-modal excitation and detected the optical signal, demodulating at the fourth harmonic. On the right, we applied the novel bi-modal tip excitation technique, demodulating at the second harmonic of the sum of the two frequencies. While the difference in the signal intensity (SNR) between the 1st and 4th harmonic in the mono-modal method is of the order of 1/1000, for the bi-modal method, it's of the order of 1/2.

to locally probe the change in optical signal in the near field. This will also help better understand and conclude whether PPC in $LaAlO_3/SrTiO_3$ is a local effect. It may be particularly interesting to extract from optical traces a coherence length of local changes of conductivity from such measurements.

Combining the notion of local excitation with sparse signal processing mentioned in Section 5.1 will allow for comparison of continuous wave induced photodynamics to ultrafast ones in this material. This may answer the question of whether significant novel features are apparent in the near field, and how are these compared to far field measurements.

Finally, it may be appealing to study to find a theoretical explanation of persistent photoconductivity in $LaAlO_3/SrTiO_3$ formulated via near field measurements and/or by use of a broadband source. Namely, is there a theory to show whether the source of PPC is in the oxygen vacancies in $SrTiO_3$ or the two dimensional electron gas at the interface of the two materials? This may serve as a base for future studies of conduction boundaries in various two-dimensional materials, such as graphene, MoS_2, mixed granular structures with percolation limits and more.

5.2 Composite Pulses for Quantum Information Processing

As discussed in Chapter 2.2.2, we have introduced a new family of detuning-modulated CPs to enable high-fidelity state transfer within the quantum error threshold of 10^{-4}, that is robust to errors of up to several percent in the target

values of coupling, detuning and pulse area. We also show that our method offers a minimal pulse overhead and robustness to the system's lifetime, where the shortest sequence is composed of $N = 2$ pulses. We extended this findings and developed a universal detuning-modulated CP technique, where the shortest sequence is composed of $N = 4$ pulses. This, to the best of our knowledge, is currently the shortest available universal composite sequence.

This technique is suitable for, but not limited to, implementation in integrated photonic circuits, which are considered a strong candidate for quantum computation hardware and QIP. As integrated photonic circuits are prone to fabrication errors, leading to a decrease in the produced signal fidelity, their application in QIP has been considered limited. Furthermore, precise quantum state preparation in integrated photonics requires an additional preliminary process of state preparation, which adds to the complexity of scaling-up device fabrication. To this end, universal detuning-modulated composite pulses may enable the production of high fidelity photonic gates for quantum computation without rigid requirements of the input signal. An ongoing collaboration with the Zadok Laboratory at Bar-Ilan University is pending initial experimental results of this photonic implementation.

In the following subsections, I briefly summarize ongoing projects that stemmed from the results of my research: deep learning for nanophotonics, detuning-modulated composite designs of crystals for nonlinear frequency conversion and an extension of universal detuning-modulated composite pulses to derive two-qubit gates.

Deep Learning for Nanophotonics

This work provided a basis for a fruitful collaboration to combine machine learning with photonics. Our recent work, "Deep learning based reconstruction of directional coupler geometry from electromagnetic near-field distribution," [108] addresses the fact that the process of fabricating integrated photonic circuits is long and tedious, and is generally interrupted for critical dimensions monitoring. Since many of these devices are typically buried beneath an oxide layer, the task of recovering the system's physical geometry post-fabrication is a major challenge. Moreover, while measurements of near-field electromagnetic intensity distributions of devices of a certain geometry are straightforward to perform, the inverse problem of analytically recovering the geometry of a physical system from its EM field is very difficult. We introduced a deep-learning approach to overcome this challenge. The problem of accurately recovering the geometry of buried waveguide structures was formulated as an image-to-image translation. The input to the deep-learning algorithm is a map of the spatial distribution of the EM field intensity measured above the oxide layer of a coupled waveguide structure. The output is a spatial map of the structures' dielectric constant.

This research is the first to suggest a deep learning approach to solve the problem of retrieving the underlying geometry of a buried coupled waveguide structure. Furthermore, the technique allows for a continuous image-to-image translation

of a two-dimensional EM-field map to a matching two-dimensional reconstructed geometry. Most importantly, the method has excellent ability to output geometries from EM-fields well outside the distribution of the training dataset, demonstrating its remarkable learning capabilities. This work constitutes a baseline for future works of recovering more complex systems, such as waveguide arrays, as well as the retrieval of nonlinear optical dynamics and decoherence.

Our work engages the wide community that constitutes the field of photonic fabrication, and is the first to apply Pix2Pix, a strong universal image-to-image translation algorithm used, among other purposes, to optimize road pictures taken by autonomous vehicles. Our paper is a cornerstone for implementing elaborate algorithms from the field of computer vision on photonic circuit design. From a design and fabrication standpoint, it provides opportunities for innovative outlooks in post-fabrication and validation of classical and quantum integrated photonic devices.

Detuning-modulated composite segmented nonlinear crystals

An additional collaboration that emerged from the work on detuning-modulated composite pulses is in the field of non-linear optics. As the sum frequency conversion process portrays SU(2) symmetry under the undepleted pump approximation [109], it is straightforward to adopt the composite pulses formalism to design detuning-modulated composite segmented periodically poled (CSPP) crystals for non-linear frequency conversion.

Detuning-modualted two-qubit gates

A natural continuation of detuning-modulated composite pulses would be to search for detuning-modulated composite two-qubit gates. Previous works [110, 111] have suggested an implementation of coupling-modulated composite pulses for two qubit gates based on the well-known Wimperis BB1 scheme [112]. This achieves robustness to errors of up to the order of six in the two-qubit coupling parameter J. However, the technique is of little novelty and results in a very long composite sequence, that is not always robust to the lifetime of the two-qubit system. Herein, a more general formulation of traditional composite pulses two-qubit gates [113] may result in shorter robust sequences.

The basic notion of the above general formulation is that all NMR operations are implemented by single qubit gates $R(\theta, \phi)$ and two-qubit gates $S(\Theta)$. A minimal composite pulse sequence for a two-qubit gate is suggested to follow the schematic:

The single-qubit operator R is in fact equation 2.11, which can be describe via the Cayley-Klein parameters:

$$U(a,b) = \begin{bmatrix} a & be^{-i\phi} \\ -b^* e^{i\phi} & a^* \end{bmatrix} \tag{5.1}$$

and the two-qubit operator is:

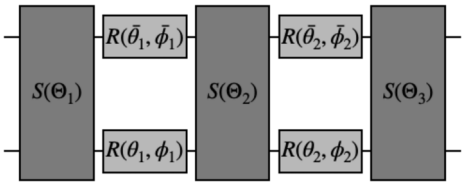

Fig. 5.2: Schematic representation of composite two-qubit gate for N=3, where S and R denote two- and single-qubit operations respectively.

$$S(\Theta_j) = \begin{bmatrix} e^{-i\Theta_j} & 0 & 0 & 0 \\ 0 & e^{i\Theta_j} & 0 & 0 \\ 0 & 0 & e^{i\Theta_j} & 0 \\ 0 & 0 & 0 & e^{-i\Theta_j} \end{bmatrix} \tag{5.2}$$

It was shown [113] that if $\Delta = 0$, the minimal solution for a two-qubit gate is obtained for $N \geq 3$. I propose a search for detuning-modulated solutions within the scope of this formalism, that may uncover shorter composite pulse sequences to obtain robust two-qubit gates.

5.3 Summary

Over the course of the past five years, I conducted a comprehensive study of near-field optical microscopy and quantum coherent control. This work, comprised of peer-reviewed journal publications along with extensive backgrounds and supplemental material to each paper, illustrate a coherent evolution of my research.

In Chapter 2.2.1, I describe the theoretical derivation and experimental application of multifrequency near-field scanning optical microscopy (MF-SNOM). This technique enables for enhanced sensitivity in near-field optical contrast imaging, while maintaining a high signal-to-noise ratio.

Chapter 2.2.2 construes the historic origins, current limitations and proposed solutions of composite pulse sequences. First, I extend the scope of composite pulse sequences from two-level quantum systems to N-level systems with SU(2) symmetry. Next, an immediate motivation for deriving detuning-modulated composite pulses (DMCPs) was declared as a means to overcome limitations of fabrication errors in integrated photonic circuits - where composite pulses had not been applied. A broad study of DMCPs for single qubit gates was introduced, opening avenues for quantum information processing implementation in photonic systems.

In Chapter 4, I presented additional work. First, I outlined the plan and execution of an interdisciplinary study of persistent photoconductivity (PPC) in the complex oxide interface, LAO/STO. By tailoring the excitation method and conducting measurements in the near-field, we were able to characterize PPC in this material as a *local* effect at room temperature. Finally, my thorough derivation of universal detuning-

modulated composite pulses was described, along with a complete translation of the theory to photonic circuit design.

The conclusions and insights of this work provide a strong basis for future research on the interface between near-field optical phenomena and quantum information processing. In particular, the detuning-modulated composite pulses can be immediately realized in passive integrated photonic devices for light propagation that is robust to fabrication errors. Further assimilation with methods of deep learning will allow to develop algorithms for precise state preparation, transfer and active control. The versatile method of universal detuning-modulated composite gates will pave the way to achieve high precision in quantum gates via short and elegant solutions. I hope that it will further push the capabilities of reaching high fidelity in any qubit architecture and for large scale quantum circuits designs.

6 Appendix: Implementation of DMCPs in integrated photonic systems

Without loss of generality, I lay out the specific steps taken to scale and tweak the detuning parameters for N-piece DMCPs calculated for Si on SiO_2 coupled waveguides. Given the available fabrication capabilities, I considered waveguides at a given constant height of $h = 340nm$ and a base width of $w_0 = 220nm$ and vice versa; with grating-coupled light of wavelengths $1550nm$ and $1310nm$.

1. Employ Lumerical Finite Difference Eigenmode (FDE) solver [103] to calculate the "on-resonance" eigenmodes of the coupled waveguide system, where both waveguides are of identical geometry and material. By calculating the symmetric and anti-symmetric eigenmodes for different distances g between the waveguides, the coupling of the system, $\kappa = (\beta_+ - \beta_-)/2$, is plotted as a function of g.

2. Calculate the detuning as a function of the difference between the two waveguide geometries. Use FDE to calculate the single-waveguide propagation constant β_w as a function of width $w = w_0 \pm \delta$. The resulting detuning is the difference between this propagation constant and that of the base width β_{w0}, namely $\Delta = (\beta_{w0} - \beta_w)/2$.

3. As the above process is numerical, it doesn't take into consideration effects, such as back-reflections created by the boundaries between two detuning-modulated waveguide pieces. Thus, we perform an iterative process of simulating the full detuning-modulated coupled waveguide light propagation, by using a Lumerical Eigenmode Expansion (EME) solver, to tweak the target δw geometric detuning values and propagation lengths.

In order to fabricate these, we provide the geometrical parameters required to design robust Si on SiO_2 waveguide couplers for input wavelengths of $\lambda = 1310nm$ and $1550nm$. Specifically, the following examples translate the parameters of Table 6.1

N	Order	$(\frac{\Delta_1}{\Omega_1}, \frac{\Delta_2}{\Omega_2}, \ldots, -\frac{\Delta_2}{\Omega_2}, -\frac{\Delta_1}{\Omega_1})$
2	1	$\pm(1, -1)$
3	1	$(1, -1, 1)\sqrt{3}$
3	2	$(1, 0, -1)2.5425$
4	1	$(1, -1, 1, -1)(\sqrt(2) + 1)$

Tab. 6.1: Detuning parameters for detuning-modulated composite π gates.

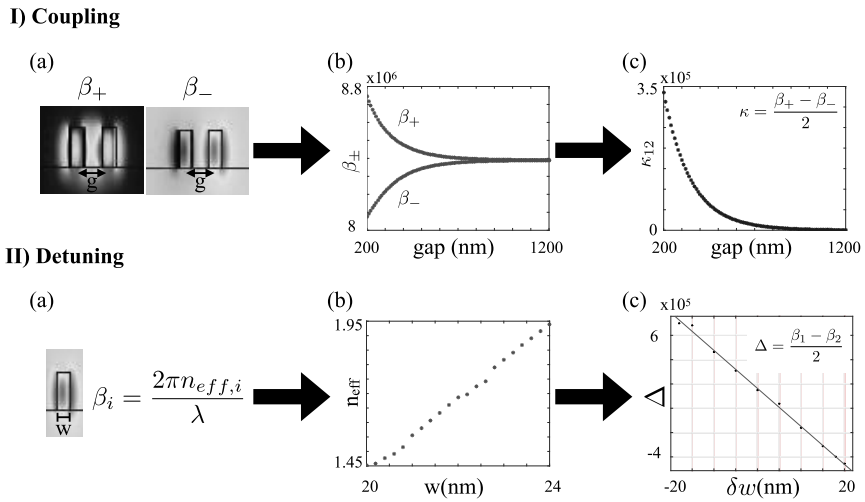

Fig. 6.1: Flow chart for determining the geometrical parameters demanded for specific couplings (I) and detunings (II) of a detuning-modulated coupled waveguide system. All calculations were performed via a FDTD Comsol Multiphysics simulation.

to Si on SiO_2 two, three and four-piece 1st-order, and a three-piece 2nd-order detuning-modulated waveguide systems.

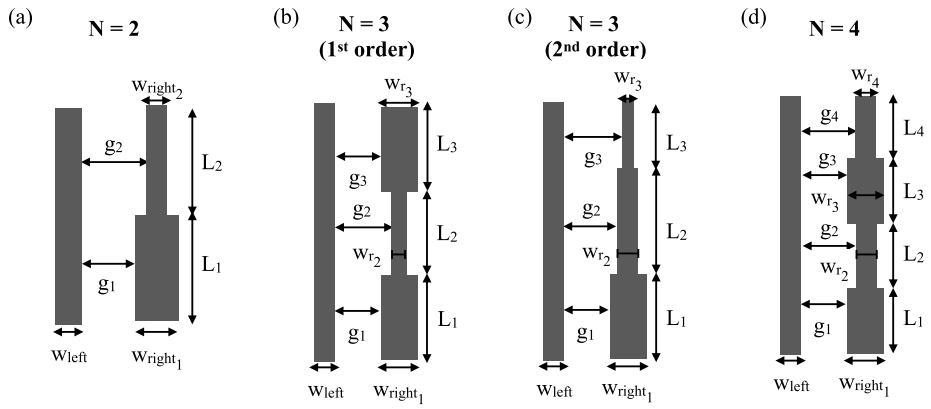

Fig. 6.2: Geometric layout of (a) N=2-piece 1st-order (b) N=3 1st-order (c) N=3 2nd-order and (d) N=4 1st-order coupled waveguide systems. L_i are the lengths of each segment i, w_{left_i} (w_{right_i}) are the widths of the left (right) waveguides of each segment, and g_i are the edge-to-edge distances between each coupled waveguides in each segment.

	N = 2 (1st)	N = 3 (1st)	N = 3 (2nd)	N = 4 (1st)
L1[um]	2.76E-05	0.00002	1.42E-05	1.57E-05
w_left1[um]	3.40E-07	3.40E-07	3.40E-07	3.40E-07
w_right1[um]	3.50E-07	3.58E-07	3.68E-07	3.66E-07
g1[um]	4.45E-07	4.41E-07	4.36E-07	4.37E-07
L2[um]	2.76E-05	0.00002	3.88E-05	1.57E-05
w_left2[um]	3.40E-07	3.40E-07	3.40E-07	3.40E-07
w_right2[um]	3.30E-07	3.22E-07	3.40E-07	3.14E-07
g2[um]	4.55E-07	4.59E-07	4.50E-07	4.63E-07
L3[um]		0.00002	1.42E-05	1.57E-05
w_left3[um]		3.40E-07	3.40E-07	3.40E-07
w_right3[um]		3.58E-07	3.12E-07	3.66E-07
g3[um]		4.41E-07	4.64E-07	4.37E-07
L4[um]				1.57E-05
w_left4[um]				3.40E-07
w_right4[um]				3.14E-07
g4[um]				4.63E-07

Fig. 6.3: Geometric parameters of coupled waveguide system with base height of h=220nm and input wavelength of 1310nm. Grating pitch optimized for TM mode coupling is 0.77um.

	N = 2 (1st)	N = 3 (1st)	N = 3 (2nd)	N = 4 (1st)
L1[um]	1.28E-05	9.52E-06	6.88E-06	7.49E-06
w_left1[um]	2.20E-07	2.20E-07	2.20E-07	2.20E-07
w_right1[um]	2.28E-07	2.33E-07	2.44E-07	2.38E-07
g1[um]	2.96E-07	2.94E-07	2.88E-07	2.91E-07
L2[um]	1.28E-05	9.52E-06	1.88E-05	7.49E-06
w_left2[um]	2.20E-07	2.20E-07	2.20E-07	2.20E-07
w_right2[um]	2.13E-07	2.08E-07	2.20E-07	2.03E-07
g2[um]	3.04E-07	3.06E-07	3.00E-07	3.09E-07
L3[um]		9.52E-06	6.88E-06	7.49E-06
w_left3[um]		2.20E-07	2.20E-07	2.20E-07
w_right3[um]		2.33E-07	1.97E-07	2.38E-07
g3[um]		2.94E-07	3.12E-07	2.91E-07
L4[um]				7.49E-06
w_left4[um]				2.20E-07
w_right4[um]				2.03E-07
g4[um]				3.09E-07

Fig. 6.4: Geometric parameters of coupled waveguide system with base height of h=340nm and input wavelength of 1310nm. Grating pitch optimized for TM mode coupling is 0.731um.

	N = 2 (1st)	N = 3 (1st)	N = 3 (2nd)	N = 4 (1st)
L1[um]	1.28E-05	8.65E-06	6.57E-06	6.73E-06
w_left1[um]	2.20E-07	2.20E-07	2.20E-07	2.20E-07
w_right1[um]	2.31E-07	2.40E-07	2.51E-07	2.49E-07
g1[um]	3.25E-07	3.20E-07	3.15E-07	3.16E-07
L2[um]	1.28E-05	8.65E-06	1.80E-05	6.73E-06
w_left2[um]	2.20E-07	2.20E-07	2.20E-07	2.20E-07
w_right2[um]	2.09E-07	2.00E-07	2.20E-07	1.91E-07
g2[um]	3.36E-07	3.40E-07	3.30E-07	3.45E-07
L3[um]		8.65E-06	6.57E-06	6.73E-06
w_left3[um]		2.20E-07	2.20E-07	2.20E-07
w_right3[um]		2.40E-07	1.89E-07	2.49E-07
g3[um]		3.20E-07	3.46E-07	3.16E-07
L4[um]				6.73E-06
w_left4[um]				2.20E-07
w_right4[um]				1.91E-07
g4[um]				3.45E-07

Fig. 6.5: Geometric parameters of coupled waveguide system with base height of h=340nm and input wavelength of 1550nm. Grating pitch optimized for TM mode coupling is 0.87um.

	N = 2 (1st)	N = 3 (1st)	N = 3 (2nd)	N = 4 (1st)
L1[um]	6.22E-05	4.31E-05	3.19E-05	3.60E-05
w_left1[um]	5.00E-07	5.00E-07	5.00E-07	5.00E-07
w_right1[um]	5.14E-07	5.24E-07	5.37E-07	5.30E-07
g1[um]	7.93E-07	7.88E-07	7.82E-07	7.85E-07
L2[um]	6.22E-05	4.31E-05	8.70E-05	3.60E-05
w_left2[um]	5.00E-07	5.00E-07	5.00E-07	5.00E-07
w_right2[um]	4.86E-07	4.76E-07	5.00E-07	4.70E-07
g2[um]	8.07E-07	8.12E-07	8.00E-07	8.15E-07
L3[um]		4.31E-05	3.19E-05	3.60E-05
w_left3[um]		5.00E-07	5.00E-07	5.00E-07
w_right3[um]		5.24E-07	4.63E-07	5.30E-07
g3[um]		7.88E-07	8.19E-07	7.85E-07
L4[um]				3.60E-05
w_left4[um]				5.00E-07
w_right4[um]				4.70E-07
g4[um]				8.15E-07

Fig. 6.6: Geometric parameters of coupled waveguide system with base height of h=220nm and input wavelength of 1550nm. Grating pitch optimized for TM mode coupling is 0.93um.

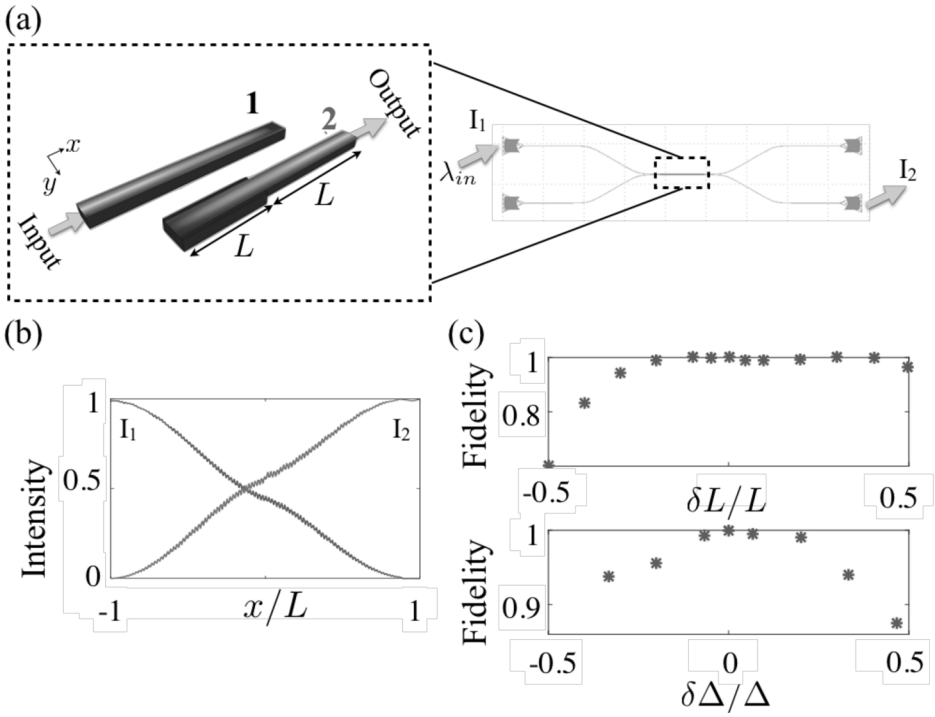

Fig. 6.7: Example experimental set-up and demonstration of robustness. (a) Input CW laser light intensity I_1 of $\lambda = 1310nm$ grating-coupled into a detuning-modulated N=2-piece 1st order coupled waveguide system. The output light intensity I_2 is grating-coupled out of the system into a detector. (b) The intensity of light in each waveguide as a function of propagation distance. (c) The normalized fidelity of the output signal as a function of relative deviation from the target values of the segment lengths L_i and detuning values Δ_i, characterized by the segment widths w_i.

Bibliography

[1] M. Born, E. Wolf, A. B. Bhatia, P. C. Clemmow, D. Gabor, A. R. Stokes, A. M. Taylor, P. A. Wayman, and W. L. Wilcock. *Principles of Optics: Electromagnetic Theory of Propagation, Interference and Diffraction of Light*. Cambridge University Press, 7 edition, 1999.

[2] L. Novotny and B. Hecht. *Principles of Nano-Optics*. Cambridge University Press, 2 edition, 2012.

[3] A. Lewis, M. Isaacson, A. Harootunian, and A. Muray. Development of a 500a spatial resolution light microscope: I. light is efficiently transmitted through lambda/16 diameter apertures. *Ultramicroscopy*, 13(3):227–231, 1984.

[4] D.W. Pohl, W. Denk, and M. Lanz. Optical stethoscopy: Image recording with resolution lambda/20. *Appl. Phys. Lett.*, 44(651), 1984.

[5] E. Betzig, J. K. Trautman, T. D. Harris, J. S. Weiner, and R. L. Kostelak. Breaking the diffraction barrier: Optical microscopy on a nanometric scale. *Science*, 251(5000):1468–1470, 1991.

[6] Y. Inouye and S. Kawata. Near-field scanning optical microscope with a metallic probe tip. *Optics Letters*, 19(159):159–161, 1994.

[7] F. Zenhausern, Y. Martin, and H.K Wickramasinge. Scanning interferometric apertureless microscopy: Optical imaging at 10 angstrom resolution. *Science*, 269:1083–1085, 1995.

[8] B. Knoll and F. Keilmann. Near-field probing of vibrational absorption for chemical microscopy. *Nature*, 399:134–137, 1999.

[9] L. Novotny. The history of near-field optics. In E. Wolf, editor, *Progress in Optics*, volume 50, chapter 5, pages 137 – 184. Elsevier, 2007.

[10] J. T. Robinson, S. F. Preble, and M. Lipson. Imaging highly confined modes in sub-micron scale silicon waveguides using transmission-based near-field scanning optical microscopy. *Opt. Express*, 14(22):10588–10595, 2006.

[11] A. Y. Nikitin, E. Yoxall, M. Schnell, S. Vélez, I. Dolado, P. Alonso-Gonzalez, F. Casanova, L. E. Hueso, and R. Hillenbrand. Nanofocusing of hyperbolic phonon polaritons in a tapered boron nitride slab. *ACS Photonics*, 3(6):924–929, 924-929.

[12] A. David, B. Gjonaj, and G. Bartal. Two-dimensional optical nanovortices at visible light. *Phys. Rev. B*, 93:121302, 2016.

[13] Z. Fei, A. S. Rodin, W. Gannett, S. Dai, W. Regan, M. Wagner, M. K. Liu, A. S. McLeod, G. Dominguez, M. Thiemens, A. H. Castro Neto, F. Keilmann, A. Zettl, R. Hillenbrand, M. M. Fogler, and D. N. Basov. Electronic and plasmonic phenomena at graphene grain boundaries. *Nat. Nano.*, 8(11):821–825, 2013.

[14] O. Khatib, J. D. Wood, A. S. McLeod, M. D. Goldflam, M. Wagner, G. L. Damhorst, J. C. Koepke, G. P. Doidge, A. Rangarajan, R. Bashir, E. Pop, J. W. Lyding, M. H. Thiemens, F. Keilmann, and D. N. Basov. Graphene-based platform for infrared near-field nanospectroscopy of water and biological materials in an aqueous environment. *ACS Nano*, 9(8):7968–7975, 2015.

[15] E. A. Muller, B. Pollard, and M. B. Raschke. Infrared chemical nano-imaging: Accessing structure, coupling, and dynamics on molecular length scales. *The Journal of Physical Chemistry Letters*, 6(7):1275–1284, 2015.

[16] C. Wu, W. J. Wolf, Y. Levartovsky, H. A. Bechtel, M. C. Martin, F. D. Toste, and E. Gross. High-spatial-resolution mapping of catalytic reactions on single particles. *Nature*, 541(7638):511–515, 2017.

[17] D. N. Basov, M. M. Fogler, and F. J. García de Abajo. Polaritons in van der waals materials. *Science*, 354(6309), 2016.

[18] B. Knoll and F. Keilmann. Enhanced dielectric contrast in scattering-type scanning near-field optical microscopy. *Optics Communications*, 182(4):321–328, 2000.

[19] R. Hillenbrand, B. Knoll, and F. Keilmann. Pure optical contrast in scattering-type scanning near-field microscopy. *Journal of Microscopy*, 202(1):77–83, 2000.

[20] F. Keilmann and R. Hillenbrand. Near-field microscopy by elastic light scattering from a tip. *Philos. Trans. R. Soc. Lond. A*, 362(1817):787–805, 2004.

[21] N. Ocelic, A. Huber, and R. Hillenbrand. Pseudoheterodyne detection for background-free near-field spectroscopy. *Appl. Phys. Lett.*, 89(10):101124, 2006.

[22] E.A. Ash and G. Nichols. Super-resolution aperture scanning microscope. *Nature*, 237:510–512, 1972.

[23] H. Greener, M. Mrejen, U. Arieli, and H. Suchowski. Multifrequency excitation and detection scheme in apertureless scattering near-field scanning optical microscopy. *Opt. Lett.*, 42(16):3157–3160, Aug 2017.

[24] J. R. Lozano and R. Garcia. Theory of multifrequency atomic force microscopy. *Phys. Rev. Lett.*, 100:076102, Feb 2008.

[25] R. Garcia. *Amplitude Modulation Atomic Force Microscopy*. Wiley-VCH, 2010.

[26] D. Garcia-Sanchez, A. San Paulo, M. J. Esplandiu, F. Perez-Murano, L. Forró, A. Aguasca, and A. Bachtold. Mechanical detection of carbon nanotube resonator vibrations. *Phys. Rev. Lett.*, 99:085501, Aug 2007.

[27] R. Hillenbrand, M. Stark, and R. Guckenberger. Higher harmonics generation in tapping mode atomic force microscopy: insights into the tip-sample interactions. *Appl. Phys. Lett.*, 76(3478), 2000.

[28] C. Bustamante and D. Keller. Scanning force microscopy in biology. *Physics Today*, 12(32), 1995.

[29] R. W. Stark and W. M. Heckl. Fourier transformed atomic force microscopy: tapping mode atomic force microscopy beyond the hookian approximation. *Surface Science*, 457(219-228), 2000.

[30] M. Labardi, S. Patane, and M. Allegrini. Artifact-free near-field optical imaging by apertureless microscopy. *Appl. Phys. Lett.*, 77(5):621–623, 2000.

[31] P. G. Gucciardi, G. Bachelier, and M. Allegrini. Far-field background suppression in tip-modulated apertureless near-field optical microscopy. *J. Appl. Phys.*, 99:124309, 2006.

[32] M. Abramowitz and I. A. Stegun. *Handbook of Mathematical Functions with Formulas, Graphs, and Mathematical Tables*. Dover, New York, ninth dover printing, tenth gpo printing edition, 1964.

[33] M.A. Nielsen and I.L. Chuang. *Quantum Computation and Quantum Information*. Cambridge University Press, Cambridge, 2000.

[34] A. Sørensen and K. Mølmer. Quantum computation with ions in thermal motion. *Phys. Rev. Lett.*, 82:1971–1974, Mar 1999.

[35] L. Allen and J.H Eberly. *Optical Resonance and Two Level Systems*. Dover, New York, 1975.

[36] J. Gong and S. A. Rice. General method for complete population transfer in degenerate systems. *Phys. Rev. A*, 69:063410, Jun 2004.

[37] J. Gong and S.A. Rice. *J. Chem. Phys.*, 120:9984, 2004.

[38] H. Suchowski, Y. Silberberg, and D. B. Uskov. Pythagorean coupling: Complete population transfer in a four-state system. *Phys. Rev. A*, 84:013414, Jul 2011.

[39] A. Yariv. *IEEE, J. Quantum Electronics*, 9:9, 1973.

[40] J. Keeler. *Understanding NMR*. John Wiley and Sons, New York, 2005.

[41] I. I. Rabi, J. R. Zacharias, S. Millman, and P. Kusch. A new method of measuring nuclear magnetic moment. *Phys. Rev.*, 53:318, 1938.

[42] C. Zener. Non-adiabatic crossing of energy levels. *Proc. R. Soc. London Ser. A*, 137:696, 1932.

[43] N. Rosen and C. Zener. Double stern-gerlach experiment and related collision phenomena. *Phys. Rev.*, 40:502, 1932.

[44] E. L. Hahn. Spin echoes. *Phys. Rev.*, 80:580–594, Nov 1950.

[45] H. Y. Carr and E. M. Purcell. Effects of diffusion on free precession in nuclear magnetic resonance experiments. *Phys. Rev.*, 94:630–638, May 1954.

[46] H. M. Cho, R. Tycko, A. Pines, and J. Guckenheimer. Iterative maps for bistable excitation of two-level systems. *Phys. Rev. Lett.*, 56:1905–1908, May 1986.

[47] H. K. Cummins, G. Llewellyn, and J. A. Jones. Tackling systematic errors in quantum logic gates with composite rotations. *Phys. Rev. A*, 67:042308, Apr 2003.

[48] M. H. Levitt and R. Freeman. *J. Magn. Reson.*, 33:473, 1979.

[49] R. Freeman, Kempsell S.P., and M.H. Levitt. *J. Magn. Reson.*, 38:453, 1980.

[50] M.H. Levitt. *Prog. Nucl. Magn. Reson. Spectrosc.*, 18:61, 1986.

[51] R. Tycko. Broadband population inversion. *Phys. Rev. Lett.*, 51:775–777, Aug 1983.

[52] M. H. Levitt. Composite pulses. *Prog. Nucl. Magn. Reson. Spectrosc*, 18:61–122, 1986.

[53] B. T. Torosov and N. V. Vitanov. Smooth composite pulses for high-fidelity quantum information processing. *Phys. Rev. A*, 83:053420, May 2011.

[54] B. T. Torosov, E. S. Kyoseva, and N. V. Vitanov. Composite pulses for ultrabroad-band and ultranarrow-band excitation. *Phys. Rev. A*, 92:033406, Sep 2015.

[55] M. H. Levitt, D. Suter, and R. R. Ernst. Composite pulse excitation in three-level systems. *The Journal of Chemical Physics*, 80(7):3064–3068, 1984.

[56] J. R. Kuklinski, U. Gaubatz, F. T. Hioe, and K. Bergmann. Adiabatic population transfer in a three-level system driven by delayed laser pulses. *Phys. Rev. A*, 40:6741–6744, Dec 1989.

[57] J. Oreg, F. T. Hioe, and J. H. Eberly. Adiabatic following in multilevel systems. *Phys. Rev. A*, 29:690–697, Feb 1984.

[58] K. Bergmann, H. Theuer, and B. W. Shore. Coherent population transfer among quantum states of atoms and molecules. *Rev. Mod. Phys.*, 70:1003–1025, Jul 1998.

[59] B. W. Shore, K. Bergmann, and J. Oreg. Coherent population transfer: Stimulated raman adiabatic passage and the landau-zener picture. *Zeitschrift für Physik D Atoms, Molecules and Clusters*, 23(1):33–39, 1992.

[60] M. Fleischauer, A. Imamoglu, and J.P. Marangos. Electromagnetically induced transparency: optics in coherent media. *Rev. Mod. Phys.*, 77:633–673, 2005.

[61] N. V. Vitanov, A. A. Rangelov, B. W. Shore, and K. Bergmann. Stimulated raman adiabatic passage in physics, chemistry, and beyond. *Rev. Mod. Phys.*, 89:015006, Mar 2017.

[62] J. R. Morris and B. W. Shore. Reduction of degenerate two-level excitation to independent two-state systems. *Phys. Rev. A*, 27:906–912, Feb 1983.

[63] E. S. Kyoseva and N. V. Vitanov. Coherent pulsed excitation of degenerate multistate systems: Exact analytic solutions. *Phys. Rev. A*, 73:023420, Feb 2006.

[64] R. J. Cook and B. W. Shore. Coherent dynamics of n-level atoms and molecules. iii. an analytically soluble periodic case. *Phys. Rev. A*, 20:539–544, Aug 1979.

[65] F. T. Hioe. N-level quantum systems with su(2) dynamic symmetry. *J. Opt. Soc. Am. B*, 4(8):1327–1332, 1987.

[66] E. Majorana. *Nuovo Cimento*, 9:43–50, 1932.

[67] S. Longhi. Photonic transport via chirped adiabatic passage in optical waveguides. *Journal of Physics B: Atomic, Molecular and Optical Physics*, 40(12):F189–F195, jun 2007.

[68] Y. Lahini, F. Pozzi, M. Sorel, R. Morandotti, D. N. Christodoulides, and Y. Silberberg. Effect of nonlinearity on adiabatic evolution of light. *Phys. Rev. Lett.*, 101:193901, Nov 2008.

[69] C. Ciret, V. Coda, A. A. Rangelov, D. N. Neshev, and G. Montemezzani. Broadband adiabatic light transfer in optically induced waveguide arrays. *Phys. Rev. A*, 87:013806, Jan 2013.

[70] M. Mrejen, H. Suchowski, T. Hatakeyama, Y. Wang, and X. Zhang. Experimental realization of two decoupled directional couplers in a subwavelength packing by adiabatic elimination. *Nano Letters*, 15(11):7383–7387, 2015. PMID: 26421374.

[71] M. Mrejen, H. Suchowski, T. Hatakeyama, C. Wu, L. Feng, K. O'Brien, Y. Wang, and X. Zhang. Adiabatic elimination-based coupling control in densely packed subwavelength waveguides. *Nature Communications*, page 7565, 2015.

[72] I. Cohen, A. Rotem, and A. Retzker. Refocusing two-qubit-gate noise for trapped ions by composite pulses. *Phys. Rev. A*, 93:032340, Mar 2016.

[73] E. Kyoseva and N. V. Vitanov. Arbitrarily accurate passband composite pulses for dynamical suppression of amplitude noise. *Phys. Rev. A*, 88:063410, Dec 2013.

[74] W. Hu, S. Kaiser, D. Nicoletti, C. R. Hunt, I. Gierz, M. C. Hoffmann, M. Le Tacon, T. Loew, B. Keimer, and A. Cavalleri. Optically enhanced coherent transport in yba2cu3o6.5 by ultrafast redistribution of interlayer coupling. *Nat Mater*, (7):705–711, 2014.

[75] E. Casandruc, D. Nicoletti, S. Rajasekaran, Y. Laplace, V. Khanna, G. D. Gu, J. P. Hill, and A. Cavalleri. Wavelength-dependent optical enhancement of superconducting interlayer coupling in $La_{1.885}Ba_{0.115}Cuo_4$. *Phys. Rev. B*, 91:174502, May 2015.

[76] K. X. Jin, W. Lin, B. C. Luo, and T. Wu. Photoinduced modulation and relaxation characteristics in laalo3/srtio3 heterointerface. 5:8778 EP –, 03 2015.

[77] B. T. O'Callahan, A. C. Jones, J. Hyung Park, D. H. Cobden, J. M. Atkin, and M. B. Raschke. Inhomogeneity of the ultrafast insulator-to-metal transition dynamics of vo2. 6:6849 EP –, 04 2015.

[78] P. Moetakef, T. A. Cain, D. G. Ouellette, J. Y. Zhang, D. O. Klenov, A. Janotti, C. G. Van de Walle, S. Rajan, S. J. Allen, and S. Stemmer. Electrostatic carrier doping of gdtio3/srtio3 interfaces. *Applied Physics Letters*, 99(23):232116, 2011.

[79] A. D. Caviglia, S. Gariglio, N. Reyren, D. Jaccard, T. Schneider, M. Gabay, S. Thiel, G. Hammerl, J. Mannhart, and J. M. Triscone. Electric field control of the laalo3/srtio3 interface ground state. *Nature*, 456(7222):624–627, 12 2008.

[80] N. Reyren, S. Thiel, A. D. Caviglia, L. Fitting Kourkoutis, G. Hammerl, C. Richter, C. W. Schneider, T. Kopp, A.S. Rüetschi, D. Jaccard, M. Gabay, D. A. Muller, J.-M. Triscone, and J. Mannhart. Superconducting interfaces between insulating oxides. *Science*, 317(5842):1196–1199, 2007.

[81] J. A. Bert, B. Kalisky, C. Bell, M. Kim, Y. Hikita, H. Y. Hwang, and K. A. Moler. Direct imaging of the coexistence of ferromagnetism and superconductivity at the laalo3/srtio3 interface. *Nat Phys*, 7(10):767–771, 10 2011.

[82] K. Ueno, S. Nakamura, H. Shimotani, A. Ohtomo, N. Kimura, T. Nojima, H. Aoki, Y. Iwasa, and M. Kawasaki. Electric-field-induced superconductivity in an insulator. *Nat Mater*, 7(11):855–858, 11 2008.

[83] J. F. Schooley, W. R. Hosler, and M. L. Cohen. Superconductivity in semiconducting $srtio_3$. *Phys. Rev. Lett.*, 12:474–475, Apr 1964.

[84] H. P. R. Frederikse, W. R. Thurber, and W. R. Hosler. Electronic transport in strontium titanate. *Phys. Rev.*, 134:A442–A445, Apr 1964.

[85] J. H. Barrett. Dielectric constant in perovskite type crystals. *Phys. Rev.*, 86:118–120, Apr 1952.

[86] K. A. Müller and H. Burkard. Srtio$_3$: An intrinsic quantum paraelectric below 4 k. *Phys. Rev. B*, 19:3593–3602, Apr 1979.

[87] J. Hemberger, P. Lunkenheimer, R. Viana, R. Böhmer, and A. Loidl. Electric-field-dependent dielectric constant and nonlinear susceptibility in srtio$_3$. *Phys. Rev. B*, 52:13159–13162, Nov 1995.

[88] K. Zhao, K. Jin, Y. Huang, S. Zhao, H. Lu, M. He, Z. Chen, Y. Zhou, and G. Yang. Ultraviolet fast-response photoelectric effect in tilted orientation srtio3 single crystals. *Applied Physics Letters*, 89(17):173507, 2006.

[89] D. Kan, T. Terashima, R. Kanda, A. Masuno, K. Tanaka, S. Chu, H. Kan, A. Ishizumi, Y. Kanemitsu, Y. Shimakawa, and M. Takano. Blue-light emission at room temperature from ar+-irradiated srtio3. *Nat Mater*, 4(11):816–819, 11 2005.

[90] M. C. Tarun, F. A. Selim, and M. D. McCluskey. Persistent photoconductivity in strontium titanate. *Phys. Rev. Lett.*, 111:187403, Oct 2013.

[91] A. Ohtomo and H. Y. Hwang. A high-mobility electron gas at the laalo3/srtio3 heterointerface. *Nature*, 427(6973):423–426, 01 2004.

[92] T. C. Asmara, A. Annadi, I. Santoso, P. K. Gogoi, A. Kotlov, H. M. Omer, M. Motapothula, M. B. H. Breese, M. Rübhausen, T. Venkatesan, Ariando, and A. Rusydi. Mechanisms of charge transfer and redistribution in laalo3/srtio3 revealed by high-energy optical conductivity. 5:3663 EP –, 04 2014.

[93] E. Kyoseva, H. Greener, and H. Suchowski. Detuning-modulated composite pulses for high-fidelity robust quantum control. *Phys. Rev. A*, 100:032333, Sep 2019.

[94] B. Luy, K. Kobzar, T. E. Skinner, N. Khaneja, and S. J. Glaser. Construction of universal rotations from point-to-point transformations. *Journal of Magnetic Resonance*, 176(2):179 – 186, 2005.

[95] M. Frimmer and L. Novotny. The classical bloch equations. *American Journal of Physics*, 82(10):947–954, 2014.

[96] G. Falci, A. D'Arrigo, A. Mastellone, and E. Paladino. Initial decoherence in solid state qubits. *Phys. Rev. Lett.*, 94:167002, Apr 2005.

[97] E. Collin, G. Ithier, A. Aassime, P. Joyez, D. Vion, and D. Esteve. Nmr-like control of a quantum bit superconducting circuit. *Phys. Rev. Lett.*, 93:157005, Oct 2004.

[98] T. Faust, J. Rieger, M. J. Seitner, J. P. Kotthaus, and E. M. Weig. Coherent control of a classical nanomechanical two-level system. *Nature Physics*, 9:485 EP –, 07 2013.

[99] R. Hanson, O. Gywat, and D. D. Awschalom. Room-temperature manipulation and decoherence of a single spin in diamond. *Phys. Rev. B*, 74:161203, Oct 2006.

[100] S. Takahashi, L. C. Brunel, D. T. Edwards, J. van Tol, G. Ramian, S. Han, and M. S. Sherwin. Pulsed electron paramagnetic resonance spectroscopy powered by a free-electron laser. *Nature*, 489(7416):409–413, 2012.

[101] J. Wang, F. Sciarrino, A. Laing, and M. G. Thompson. Integrated photonic quantum technologies. *Nature Photonics*, 14(5):273–284, 2020.

[102] T. Rudolph. Why i am optimistic about the silicon-photonic route to quantum computing. *APL Photonics*, 2(3):030901, 2017.

[103] Lumerical inc. https://www.lumerical.com/products/.

[104] M. Mrejen, L. Yadgarov, A. Levanon, and H. Suchowski. Transient exciton-polariton dynamics in wse2 by ultrafast near-field imaging. *Science Advances*, 5(2), 2019.

[105] M. Mishali and Y. C. Eldar. From theory to practice: Sub-nyquist sampling of sparse wideband analog signals. *IEEE Journal of selected topics in signal processing*, 4(2):375–391, 2010.

[106] Y. C. Eldar and G. Kutyniok. *Compressed sensing: theory and applications*. Cambridge university press, 2012.

[107] S. Gazit, A. Szameit, Y. C. Eldar, and M. Segev. Super-resolution and reconstruction of sparse sub-wavelength images. *Optics express*, 17(26):23920–23946, 2009.

[108] T. Coen, H. Greener, M. Mrejen, L. Wolf, and H. Suchowski. Deep learning based reconstruction of directional coupler geometry from electromagnetic near-field distribution. *OSA Continuum*, 3(8):2222–2231, 2020.

[109] H. Suchowski, D. Oron, A. Arie, and Y. Silberberg. Geometrical representation of sum frequency generation and adiabatic frequency conversion. *Phys. Rev. A*, 78:063821, Dec 2008.

[110] J. A. Jones. Robust ising gates for practical quantum computation. *Physical Review A*, 67(1):012317, 2003.

[111] C. D. Hill. Robust controlled-not gates from almost any interaction. *Physical review letters*, 98(18):180501, 2007.

[112] S. Wimperis. Broadband, narrowband, and passband composite pulses for use in advanced nmr experiments. *Journal of Magnetic Resonance, Series A*, 109(2):221–231, 1994.

[113] T. Ichikawa, U. Güngördü, M. Bando, Y. Kondo, and M. Nakahara. Minimal and robust composite two-qubit gates with ising-type interaction. *Physical Review A*, 87(2):022323, 2013.

List of Figures

List of Tables

תקציר

בעידן הנוכחי, בו טכניקות חדשות פורצות את מגבלות הפבריבקציה של חומרים בסדרי גודל ננומטריים, האפיון וההבנה של התכונות הפיזיקליות הבסיסיות שלהם הינה חשובה ביותר. בפרט, היכולת לשלוט על האופן שבו ניתן לבצע מניפולציות על חומרים אלו וכיצד הם מבצעים אינטראקציה עם אור, מהווה מפתח לפיתוח הדור הבא של גלאים ומודולטורים לאינפורמציה אלקטרונית ואופטית. בעבודת דוקטורט זו, חקרתי אינטראקציות בין אור וחומר בשתי חזיתות, הראשונה דרך מיקרוסקופ שדה קרוב סורק, והשנייה דרך פיתוח סכימה חדשה של פולסים מורכבים עבור שליטה קוהרנטית קוונטית.

בשנים האחרונות, מיקרוסקופ שדה קרוב סורק (SNOM) ביצע מהפכה במחקר הפיזיקה הבסיסית, בשל היותו אחת הטכניקות הבודדות להדמייה לא פולשנית אשר לא מוגבלת ברזולוציה האופטית של אורך הגל. תכונות אלו הינן בעלות ערך גדול במיוחד להבנת תהליכים במערכות כגון חומרים דו-מימדיים, מבנים פלזמוניים ומוליכי גלים, המאפשרים לעצב את האינטראקציה בין האור והחומר בסקלאה הננו-מטרית. ה-SNOM מבוסס על מיקרוסקופ הכוח האטומי (AFM). הרזולוצייה המרחבית שלו מוגבלת בעיקר על ידי חוד המחט החוקרת הזעירה (כ-15 ננומטרים), ועל ידי יכולת ההבחנה בין סיגנל שדה קרוב אופטי מרקע שדה רחוב אופטי חזק ביותר. כך, השגת רגישות גבוהה לשדה הקרוב ממדידות כאלו הינו אתגר משמעותי. בעבודה זו, פיתחתי תיאוריה, תכננתי וביצעתי טכניקה ניסוית להדמיית שדה אופטי, לו רגישות מוגברת לגילוי סיגנלים חלשים של קונטרסט דיאלקטרי בשדה הקרוב. בעבודתי, השגתי הגברה בפקטור שתיים ברגישות מדידות השדה הקרוב כפונקציה של המרחק בין המחט לדגם, וכך לשיפור מדידות אופטיות מסוג זה.

החזית השנייה למחקרי התמקדה בקידום סכימות של שליטה קוהרנטית קוונטית עבור עיבוד אינפורמציה קוונטית (QIP). בפרט, מטרתי היתה לתכנן פרוטוקולים עבור פלטפורמות של מעגלים קוונטיים משולבים פוטוניים; פרוטוקולים עם דיוק גבוה ועמידים לשגיאות במסגרת הסף המקובל עבור QIP. חקרתי את הדינמיקה במערכות קוונטיות באינטראקציה עם שדות אלקטרומגנטיים חיצוניים, ופיתחתי טכניקות למעבר מצבים בתוך הסף המקובל ל-QIP. הכללתי סכימות מוכרות של פולסים מורכבים למערכות עם N רמות וסימטריית SU2, ופיתחתי משפחה חדשה של פולסים מורכבים בהם השמשתי בראשונה את פרמטר ה-detuning כפרמטר שליטה. פולסים מורכבים המאופננים ב-detuning והשערים האוניברסלביים שניתן ליצור איתם הינם עמידים מאוד בפני שגיאות באורך הפולס, במסגרת זמן חיי המערכת הפיזיקלית. פולסים אלו מתאימים במיוחד ליישום במעגלים משולבים פוטוניים כדי להתגבר על אי-דיוקים בפבריקציה ולהתוות דרך עבור סכימות מדויקות לעיבוד אינפורמציה קוונטית. יתרה מכך, סכימות מורכבים מאופננות detuning מהוות בסיס לטכניקות תיקון שגיאות קצרות המתאימות לשליטה על מגוון ארכיטקטורות פיזיות ליצירת קיוביטים.

Tel Aviv University
School of Physics and Astronomy
Condensed Matter Department
Femto-Nano Group

מיקרוסקופיית שדה-קרוב אופטי רב תדרי ופולסים מורכבים עבור שליטה קוהרנטית קוונטית

חיבור לשם קבלת התואר
דוקטורט לפילוסופיה

מאת:
הדר גרינר

עבודה זו בוצעה תחת הנחייתו של:
פרופ׳ חיים סוכובסקי

מרץ 2021